Università degli Studi di Cagliari

DOTTORATO DI RICERCA

IN INGEGNERIA INDUSTRIALE

Ciclo XXIX

MODELLING AND ANALYSIS OF MEDIUM-SIZE HYBRID CSP-CPV SYSTEMS DESIGNED FOR IMPROVING THE DISPATCHABILITY OF SOLAR POWER PLANTS

Settore scientifico disciplinare di afferenza:

ING-IND09 - Sistemi per l'energia e l'ambiente

Presentata da:	LUCA MIGLIARI
Coordinatore Dottorato:	PROF. FRANCESCO AYMERICH
Tutor:	PROF. DANIELE COCCO

Esame finale anno accademico 2015-2016
Tesi discussa nella sessione d'esame marzo – aprile 2017

UNIONE EUROPEA
Fondo sociale europeo

REGIONE AUTONOMA DELLA SARDEGNA

POR SARDEGNA
obiettivo competitività regionale e occupazione

MODELLING AND ANALYSIS OF MEDIUM-SIZE HYBRID CSP-CPV SYSTEMS DESIGNED FOR IMPROVING THE DISPATCHABILITY OF SOLAR POWER PLANTS

LUCA MIGLIARI

Dottorato di Ricerca in Ingegneria Industriale
Università degli Studi di Cagliari
XXIX Ciclo

MODELLING AND ANALYSIS OF MEDIUM-SIZE HYBRID CSP-CPV SYSTEMS DESIGNED FOR IMPROVING THE DISPATCHABILITY OF SOLAR POWER PLANTS

LUCA MIGLIARI

Supervisor:
Professor Daniele COCCO
University of Cagliari, Italy

Dottorato di Ricerca in Ingegneria Industriale
Università degli Studi di Cagliari
XXIX Ciclo

Acknowledgements

This work was carried out during the years 2014-2016 at the Department of Mechanical, Chemicals and Materials Engineering, University of Cagliari.

I owe my deepest gratitude to Professor Daniele Cocco, who supervised and guided my work with professionalism and perseverance and who never restricted my creativity and ideas.

I am deeply grateful to my research team, led by Prof. Daniele Cocco, Prof. Giorgio Cau and Prof. Pierpaolo Puddu, and composed of my office colleagues Simone, Mario, Efisio, Francesco and Mario.

I want to express my gratitude to the revisors of the manuscript Prof. Giampaolo Manzolini and Prof. Alvaro de Gracia.

I gratefully acknowledge Sardinia Regional Government for the financial support of my PhD scholarship (P.O.R. Sardegna FSE, Operational Programme of the Autonomous Region of Sardinia, European Social Fund 2007-2013- Axis IV, Objective l.3, Line of Activity l.3.1.).

I want to thank precisely here, at the end of the list, Giulia, my family and my friends of a lifetime for their love, which never ends.

Abstract

The research study of the present Ph.D. Thesis has been carried out in order to study the performance of medium-size hybrid CSP-CPV systems designed for improving the dispatchability of Solar Power Plants and to develop and optimize novel management strategies for this kind of plants.

The research topic has been chosen also for seizing the opportunity of testing the research results on a real plant: in fact, following the market trend, together with research purposes, an innovative renewable power plant is being built in Sardinia (Italy), which hybridizes CSP and CPV technologies together with thermal and electrochemical storage concepts: the Ottana Solar Facility.

A preliminary study has permitted the author to examine in depth some of the main still-uncertain aspects with regards to the only CSP section of the Ottana Solar Facility: thermal losses influence on the performance of the overall Concentrating Solar Power Plant has been studied in connection with the main plant sections (Solar Field, Thermal Energy Storage and Power Block) during the different operating phases of the plant and according to weather conditions and load requirements. A special focus on the Solar Field behaviour allowed the author to study in detail the thermo-fluid dynamic evolution of the Heat Transfer Fluid temperature along the Solar Field loops across the time, during the morning warm-ups, the evening shutdowns and the full-operation transients and to determine a regulation curve for the Solar Field control. A deep analysis on the effects of implementing a recirculation strategy in the Solar Field management has been conducted. Different management strategies have been proposed and studied, for the overall hybrid CSP-CPV system.

The results of the present Thesis allow to increase the scientific knowledge of hybrid CSP-CPV systems and show the improvement of the

power dispatchability that can be achieved with a suitable integration of Concentrating Solar Power and Concentrating Photovoltaic.

Contents

List of Figures

List of Tables

Chapter 1

Introduction

1.1. Motivation and objectives

Nowadays, the overall share of electricity from Renewable Energy Sources (RES) in OECD countries accounts for 37% of the overall production. Among RES, wind power accounts for 34% and solar technologies for 18% on total [1]. In Italy, in particular, the ratio between the RES electricity production and the total gross internal consumption was 37.5% in 2014, with a total installed RES power of more than 50 GW. Still referring to the Italian situation, at the end of 2014, the installed solar power capacity was of 18.6 GW, mainly from photovoltaic systems, accounting for 37% on the Italian total installed RES power. These solar power systems allowed a gross energy production at the end of 2014 of over 22 TWh/year, which corresponded almost to 7% of the Italian total gross internal consumption (322 TWh/year) [2].

As it is well known, one of the main drawbacks of solar and wind renewable energy sources is their intermittent and variable nature, which can cause frequency imbalance and serious problems in the grid management. In the near future, a further expansion of wind and Solar Power Plants is going to become more and more challenging from a point of view of the grid stability and of the electric service reliability.

Up to now, the fluctuations in electricity production introduced by unpredictable RES plants have been compensated by predictable (mainly fossil-fuelled) power plants; but in the forthcoming future, different strategies will have to be deployed in order to increase the security and

quality of power supply, such as the use of more flexible thermal power plants, the introduction of suitable energy storage systems [3] and the adoption of integrated demand-side management strategies [4].

The idea of integrating different renewable power plants and energy storage systems is considered as an interesting option to smooth the effects of the variability and intermittency of Renewable Energy Sources. The integrated systems, also known as Hybrid Renewable Energy Systems (HRES), are widely studied in literature [5]. Numerous studies ([6] [7] [8]) have pointed out the improvement in performance induced by the integration of different generation sources, especially in the case of intermittent RES generators. Moreover, HRES is a common solution for stand-alone power generation systems based on renewable energy technologies [9], especially where the grid extensions or the use of fossil fuels are too expensive [10] or technically impossible to build.

Owing to the complementary nature of solar and wind renewable sources, the most studied HRES so far is the solar-wind-based system [11], mainly composed of a photovoltaic array, a wind turbine and a battery bank. The main weakness of this hybrid technology, as pointed out by several authors, is the issue of the life time and cost of the battery bank; since the batteries have to be replaced several times in a typical plant life cycle of 20-25 years and their required maintenance is very frequent [12].

Another new and promising option for a sustainable power generation mix is represented by the hybridization of different Solar Power Plants, such as Concentrating Solar Power (CSP) and photovoltaic plants. To the author knowledge, this configuration has not yet been investigated in depth and only one work has been carried out to evaluate the dispatch features of a combined CSP-PV plant [13]. On the contrary, it is instructive that some CSP companies have begun marketing hybrid projects associating CSP and PV to offer fully dispatchable power at lower costs to some customers [14]. As stated by [15], hybrid CSP-PV plant will probably operate with higher energy production costs than those of CSP and PV plants, but the hybrid combination could enable 24-h electricity generation, reaching greater capacity factors than the sole CSP or PV plants.

The idea at the base of the hybridization of CSP and PV is to obtain better overall performances, with respect to single solutions. In fact, the hybrid solution allows exploiting the advantages of each technology to counteract the disadvantages of the other. Generally, PV is more appropriate to high latitudes, especially in locations characterized by frequent cloudy weather, while CSP develops its highest potential in arid or semi-arid areas like those located in the Earth's "sun-belt" (latitudes 20–40°). The state of the art of the photovoltaic technology is represented by the Concentrating Photovoltaic (CPV), which is currently the solar technology with the highest conversion efficiency (46%) owing to the use of high concentrating optics and multi-junction solar cells [16]. In particular, High Concentration Photovoltaic (HCPV) represents the most advanced CPV concept, which has already demonstrated its reliability and efficiency. CPV systems are characterized by very fast response to solar radiation fluctuations and therefore, to enhance their dispatchability, CPV systems greatly benefit from coupling with electrical storage devices [17] and the preferred option is represented by batteries [18]. On the other hand, CSP systems have conversion efficiencies (ranging from 8.5 [19] to 17% [20] depending on the technology) lower than those of CPV systems and a slower dynamic response to Direct Normal Irradiation (DNI) fluctuations. Moreover, CSP systems are usually provided with a Thermal Energy Storage (TES) section with a storage capacity of several hours at full load [21]. In this manner, CSP plants are able to achieve an important time shifting of the energy produced by the Solar Field (SF), allowing electricity generation even during the evening and night hours. The distinguishing feature of CSP plants is therefore their ability to decouple the power generation phase from the solar energy collection phase [22,23]. Another very important feature of CSP plants is represented by the use of rotating machines (turbines) in their Power Blocks, enabling them to provide ancillary services [24] to the national grid (voltage support, frequency response, regulation and spinning reserves, etc.) and to produce great amounts of energy during peaks of electricity demand [25].

The combination of CSP and CPV could therefore be a very interesting option for reducing the intermittent and variable features of solar energy. In particular, due to the use of a combined thermal/electrical energy storage section, these hybrid CSP-CPV power plants have the ability to achieve both a short-term energy storage and an energy time-shifting, with

a significant advantage in comparison to HRES based only on electrical storage (like PV-wind).

For these reasons, in the framework of the POR FESR 2007-2013 Program, the Regional Government of Sardinia (Italy) is supporting the realization of three pilot facilities based on small scale CSP Plants integrated with other RES technologies and energy storage systems. At the moment of writing, the Ottana Solar Facility, one of these projects, which hybridizes CSP and CPV technologies together with thermal and electrochemical storage concepts, is at the final stage of construction.

The Ottana Solar Facility has a nominal power output of 1 MWe and includes a CSP plant, a TES section, a Concentrating Photo-Voltaic power plant and an electrochemical storage system.

As a consequence of what previously stated, and seizing the opportunity of testing the research results on the real plant of Ottana, the target of the present Ph.D. research was to study the performance of medium-size hybrid CSP-CPV systems designed for improving the dispatchability of Solar Power Plants and to develop and optimize novel management strategies for this kind of plants. The analysis has been carried out by means of a simulation model, specifically developed to predict the hybrid system performance, responses and behaviour under the main operating phases, different weather conditions, power requests and for different time horizons. The main objective was to demonstrate the real improvements in dispatch capability achievable adopting a hybrid CSP-CPV power plant instead of single solutions.

In the specific case, the model parameters have been set with the precise intention of being customized to suit the Ottana Solar Facility configuration, and for this reason the author's choice has been to make use of the manufacturers' curves, technical data and information, when available, and to integrate them or develop new appropriate models to calculate the missing information.

The research team who worked and works on the Ottana Solar Facility is composed of researchers, professors and student from the Department of Mechanical, Chemicals and Materials Engineering and from the Department of Electrical and Electronic Engineering, both afferent to the University of Cagliari. While the design of the Concentrating Solar Power

and Thermal Energy Storage sections were supported by the Department of Mechanical, Chemicals and Materials Engineering, whom the author is affiliated to, the Concentrating photovoltaic and the electro-chemical battery design were supported by the Department of Electrical and Electronic Engineering. The development of the simulation models were made according to this subdivision too, and for this reason the Department of Electrical and Electronic Engineering leaded and leads the scientific research on the CPV and battery modeling. For this reason, the model developed by the author regarding the electrical part and the battery bank is very simplified and it is going to be substituted by the more complex one developed by the Department of Electrical and Electronic Engineering.

The final objective of the project is to join the simulation models developed by the Department of Mechanical, Chemicals and Materials engineering and by the Department of Electrical and Electronic Engineering in an overall model whose purpose is to control, manage and supervise medium-size hybrid CSP-CPV systems. The overall model will successively be tested in the Ottana Solar Facility.

Throughout the course of the research, the simulation model developed by the author has been refined and its complexity extended to a large number of components.

The Solar Field of the Concentrating Solar Power Plant of the hybrid CSP-CPV system has been simulated through three steps, following an increasing level of accuracy: a one-dimensional steady-state model has been developed under Matlab® for the yearly and weekly-based simulations, a one-dimensional unsteady model has been developed under Matlab Simulink® for the minute and hourly-based simulations and a two-dimensional dynamic model has been developed under Comsol® environment to compare and verify the results obtained through the one-dimensional unsteady model. In order to evaluate the thermal exchanges that occur among the piping, the oil flowing inside it and the environment, an appropriate thermal equivalent circuit has been studied, modeled and implemented.

Regarding the TES section of the CSP Plant, a thermal equivalent circuit representative of its internal and external thermal exchanges has been conceived, and existing models have been applied and combined in

order to appropriately model the internal and external thermal exchanges. The Power Block sections as well as the auxiliaries' consumptions have been modeled making use of the manufacturers' curve and data sheets.

As previously stated, the model of the CPV-battery section of the hybrid CSP-CPV system has been developed in a very simplified mode, because a more detailed and complex version of it is being developed by the Department of Electrical and Electronic Engineering of the University of Cagliari.

Initially, with the purpose of demonstrating the real improvements in dispatch capability achievable adopting the hybrid CSP-CPV power plant instead of single solutions, the only CSP dispatch performance has been assessed by means of the developed simulation model. Subsequently, the performance of the hybrid solution have been deeply investigated and they are reported in the following pages.

Thermal losses influence on the performance of the overall Concentrating Solar Power Plant has been studied and reported month by month for a reference year. Moreover, the thermal losses analysis has been reported in connection with the main plant sections (Solar Field, Thermal Energy Storage section and power generation unit) during the different operating phases of the plant and according to weather conditions (solar radiation, wind speed, air temperature, etc.) and load requirements. Later, the model complexity has been increased and the performance of the CSP has been investigated with reference to minute and daily intervals. A special focus on the SF behaviour allowed the author to know in detail the thermo-fluid dynamic evolution of the Heat Transfer Fluid (HTF) temperature along the SF loops across the time, during the morning warm-ups, the evening shutdowns and the full-operation transients. Furthermore, a deep analysis on the effects of implementing a recirculation strategy in the SF management has been conducted. Successively to a deep literature review on the operational strategies of CSP plant, a regulation management strategy has been proposed and studied, still with reference to the CSP section of the Ottana Solar Facility.

The dispatch capabilities of the CSP Plant have been studied, and key performance indicators for this feature have been proposed. Season,

starting time and duration influences on dispatch capability of the plant were analysed for a typical year of operation.

The final phase of the present Ph.D. research was the development of different strategies for the integration of the energy fluxes of the two CSP and CPV sections and related storages, based on an optimization algorithm. Results on the dispatch capability of the overall medium-size hybrid CSP-CPV conclude the present thesis work.

The test phase of the developed models on the Ottana Solar Facility has not being carried out yet because, unfortunately, the construction of the Solar Facility was not completed at the moment of writing the present Ph.D. Thesis.

As a consequence of the delay in the construction, the test phase on the Ottana Solar Facility is the challenging objective for the author future work.

1.2. Overview of the thesis

This Thesis is structured in six main chapters subdivided in paragraphs for each topic.

A brief description of each chapter is given in the following:

- **Chapter 2**: a general overview of the Concentrating Solar Technologies is given, with a particular focus on CSP: types of Concentrators, alternative Thermal Energy Storages and possible Power Blocks are discussed and compared. Information about costs, dispatchability and new applications of CSP conclude this chapter, together with a section on Concentrating Photovoltaic.
- **Chapter 3:** considering that the developed models have been applied assuming the Ottana Solar Facility technical data, this chapter is dedicated to a deep description of the Ottana Solar Facility project;
- **Chapter 4**: the novel simulation models proposed for the evaluation of the hybrid CSP-CPV plant performance are reported and discussed herein, together with the introduced management strategies for the only CSP section and for the entire system integration;

- **Chapter 5**: the results obtained through the simulation models discussed in the previous chapter are reported and analysed in this chapter;
- **Chapter 6**: the main conclusions and the possible future development of the present Ph.D. research are discussed.

1.3. Publications

Some of the topics discussed and obtained results shown in this thesis have already been published in international journals or presented by the author during national and international conferences.

Papers published by international journals

1) D. Cocco, L. Migliari, and M. Petrollese, "A hybrid CSP–CPV system for improving the dispatchability of Solar Power Plants," Energy Convers. Manag., vol. 114, pp. 312–323, 2016.
2) L. Migliari and S. Arena, "Thermal Energy Losses During Night, Warm-up and Full-Operation Periods of a CSP Solar Field Using Thermal Oil," Energy Procedia, vol. 82, pp. 1002–1008, 2015.
3) Migliari L, Arena S, Puddu P, Cocco D. , "Thermo-fluid dynamic analysis of a CSP solar field line during transient operation," Energy Procedia, vol. 101, pp.1167–74, 2016.
4) L. Migliari, D. Cocco, and P. Puddu, "Influence of solar field recirculation on medium-size CSP performance", submitted for the publication on Solar Energy.

Papers published by national journals

1) L. Migliari, D. Cocco, and S. Arena," L'impianto solare termodinamico di Ottana: valutazione delle perdite termiche del campo solare durante le diverse fasi operative", La Termotecnica, pp. 55-58, Settembre 2016.

2) L. Migliari, P. Puddu and D. Cocco, " L'impianto CSP di Ottana: comportamento termo-fluidodinamico del campo solare", La Termotecnica, pp. 48-50, Novembre 2016.

Papers presented during conferences and published by conference proceedings

1) D. Cocco, L. Migliari, and F. Serra, "Influence of thermal energy losses on the yearly performance of medium size CSP plants," in Proceedings Of ECOS 2015 - The 28th International Conference On Efficiency, Cost, Optimization, Simulation And Environmental Impact Of Energy Systems, 2015.
2) L. Migliari, D. Cocco, M. Petrollese, and G. Cau, "Capability of a small size CSP plant to provide dispatch power," in Proceedings Of ECOS 2016 - The 29th International Conference On Efficiency, Cost, Optimization, Simulation And Environmental Impact Of Energy Systems, 2016.
3) M. Petrollese, D. Cocco, L. Migliari, and G. Cau, "Techno-economic analysis of a hybrid CSP-CPV power Plant," in Proceedings Of ECOS 2016 - The 29th International Conference On Efficiency, Cost, Optimization, Simulation And Environmental Impact Of Energy Systems, 2016.

Poster presented by the author during conferences

1) "Capability of a small size CSP plant to provide dispatch power," in ECOS 2016 - The 29th International Conference On Efficiency, Cost, Optimization, Simulation And Environmental Impact Of Energy Systems, 2016.
2) "Thermo-fluid dynamic analysis of a CSP Solar Field line during transient operation" in 71° Congresso Nazionale ATI, Torino 2016.

Chapter 2

Solar Concentrating Technologies

2.1. Concentrating Solar Power

Concentrating Solar Power, or Solar Thermal Electricity, is a technology that allows producing heat or electricity by using mirrors that concentrate the sun's rays to a receiver. Different equipment exist, but electricity is generated in any case by using a heat engine, usually a steam turbine. CSP, hybridized with other systems, or provided with a TES, is able to offer firm capacity and dispatchable power on demand [25]. Since CSP requires direct sunlight, also known as Direct Normal Irradiance (DNI) or "beam" radiation, the best suitable places where to build those plants are located within 40° of latitude North or South (Southern Europe, Middle East and Africa, Southern USA, Australia, part of India, China). In this "sun-belt" area, the average direct radiation exceeds 2,000 kWh by square meter per year, reaching peaks of 2,800 kWh/m^2/year; and, if possible, within this area it is better to find places with low humidity and dust. The potential power production of one square kilometre of land in this area, with a CSP Plant installed, reaches 100-130 GWh/year and avoids the emission of 200-300 kg of CO_2 each year [25]. This vast solar power potential commonly exceeds the local demand, and for this reason, the electricity produced in the sun belt areas could ideally be exported to those regions with less solar irradiance. With reference to the solar-to-electricity conversion efficiency reached, the range is between 15% and 17%, but a performance increase up to 20% is expected for the forthcoming future [25].

Nowadays, 10 GW of CSP Plants are operational, under construction or under development worldwide [26]. The world interest in CSP is growing rapidly, as demonstrated by the fact the more than half of the 10 GW are under construction (1.2 GW) or development (4.2 GW). With reference to its land area, and consequently its electric consumptions, Spain is surely the country that most exploited this technology, with more than 2 GW of CSP Plants already operational. The rest of the European countries' overall projects capacity is 280 MW, but currently only 5 MW are operational and 12 MW under construction. USA detains the second place with reference to the operational capacity, which is around 1.7 GW. MENA states are deeply investing on CSP, as revealed by the fact that only 25% of their power is already operational. Still referring to data published by [26], 92 power plants use the parabolic trough concept, 22 are represented by solar tower, 12 use the linear Fresnel reflectors and only 2 are solar dishes or solar engines.

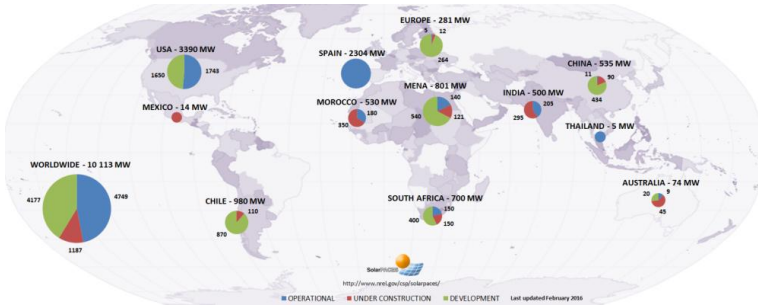

Figure 2.1. Concentrating Solar Power by Country (source: http://www.solarpaces.org/csp-technology/csp-projects-around-the-world)

2.1.1. Dispatchability

As it is known, fossil fuelled, hydroelectric, nuclear and biomass power plants are classified as *dispatchable* power plants, because they are able to provide electricity on demand, thanks to the use of a predictable primary energy source. On the contrary, wind and photovoltaic plants are based on variable and *intermittent* primary energy sources [27] and therefore they are classified as *not dispatchable power plants.*

CSP Plants provided with a TES or hybridized with other systems are potentially able to supply electricity following the demand curve 24/7 and therefore they can be defined as *semi-dispatchable* power generation systems [22]. In fact, they are able to provide a reliable output of electricity taking advantage of their TES section, but using an *intermittent* source of energy. Obviously, in case of a very large storage capacity, they are almost fully dispatchable plants [22].

Nowadays, most of the current national regulations identify CSP plants as *intermittent*, even if it has been demonstrated [23] an operability comparable to that of a conventional not-renewable power plant. If considered as dispatchable by the standards, another key characteristic of CSP plants could be exploited; in fact, they are potentially able to provide ancillary services [24] to the national grid (voltage support, frequency response, regulation and spinning reserves, etc.) and to produce great amounts of energy during peaks of electricity demand [25]. The hybridization with fossil fuels or biomass power plants permits a reduction of the system start-up time, a minimization of the levelized cost of electricity and an enhancement of the overall conversion efficiency, by raising the operating temperature.

The dispatchability features of CSP plants benefit from the availability of a reliable weather forecast. For this reason, several algorithms for Direct Normal Irradiance forecast have been developed [28] in order to obtain a sufficient reliability on solar energy prediction and therefore to use CSP plants as *dispatchable units*.

Currently, to balance the variation in the electricity production of Photo-Voltaic (PV) plants or Wind Power without batteries, other energy sources, that are rarely renewable, have to be used. Therefore, grid operators are constrained to keep in hot standby several fossil fuel power plants, with high operational costs and large CO_2 emissions. Furthermore, the worldwide installed photovoltaic power is continuously growing. In Europe, the PV electricity production is about 3.5% of the electric energy demand, and Italy leads with 7.92% [29].

For these reasons, CSP plants could successfully support a larger diffusion of intermittent Renewable Energy Sources (RES) plants, such as wind and photovoltaic systems, into the existing electrical grid [30] reducing not-renewable power reserve. The penetration of this hybridized-

or-not technology into the existing power network can replace fossil fueled power plants, saving huge amounts of CO_2 production. Moreover, other CO_2 emissions can be avoided, if considering that the energy source is freely available in the place of production, it is local, and therefore it has not to be imported and transported from other countries. A dispersed presence of CSP Plants of all sizes could be, in addition, the opportunity for the start-up of new factories and/or employment. For example, in Italy several companies have started to produce mirrors, receiver tubes (Archimede), Power Blocks (Turboden) and to offer turnkey CSP Plants (Fera, Elianto).

2.1.2. Solar Field

Mainly, Concentrating Solar Power Plants are classified by their focus geometry in *line-focus* (parabolic trough, linear Fresnel) or *point-focus* (central receiver, dish-Stirling) Solar Fields [31].

Parabolic trough technology is the most widely used technology, and consists of a Solar Field of mirrors having a parabolic trough shape, which concentrate 70-100 times the solar radiation on their focus, where a receiver tube is placed. Inside the receiver tube, a HTF is heated up to maximum temperatures around 550 °C, depending on technology. The HTF mostly used is a synthetic thermal oil, but several examples of other fluids are currently being used, i.e. water (steam) and molten salts. New interesting studies are being carried out on the influence of nanoparticle Phase Change Material (PCM) slurry on the performance of receiver tubes [32]. Water and molten salts allow higher temperatures than thermal oil, whose maximum temperature is about 400 °C. Higher temperatures are linked to higher thermodynamic conversion efficiencies of the downstream Power Block section. The so-called Direct Steam Generation avoid environmental, safety and fire prevention issues in case of lack of the HTF, while the molten salts use is advantageous because the HTF can be directly stored, avoiding heat exchangers losses and costs. With reference to this, downstream the SF, the HTF can be used to charge a direct or indirect system of TES or it can be directly used to feed the heat exchangers of a Power Block section, usually composed of a conventional

steam turbine generator. Even if Direct Steam Generation presents complicated control issues of the SF during transients and instability problems of the two-phase flux in the receiver [33], in addition to serious issues for the storage, it seems to be the most promising evolution for parabolic trough technology, together with molten salts.

The very first documented plant adopting parabolic troughs has been built is Egypt more than a century ago (1912) by an American inventor and entrepreneur. The parabolic troughs were used to produce the steam required to feed an engine, which in turn drove a pump for providing water to a small farming community (Figure 2.2) and also an implementation of a steam storage was predicted for the future.

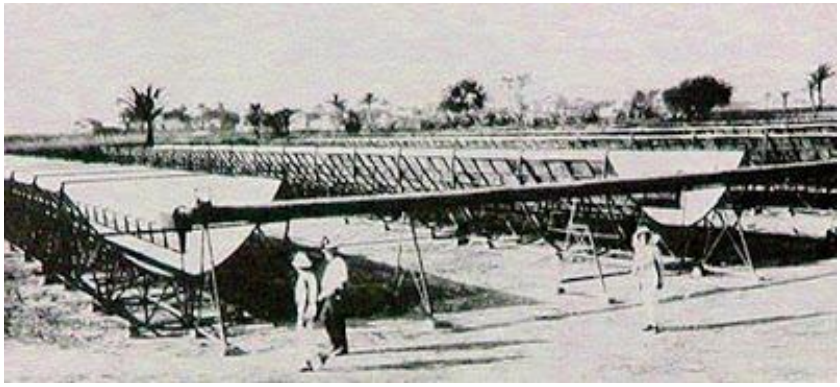

Figure 2.2. The very first CSP Plant in Egypt (source: The New York Times, published: 2 July 1916)

Coming back to our days, according to [25], more than 4 GW of CSP based on parabolic troughs are installed and operational worldwide, with an expected electricity production of 10,000 GWh/year. The parabolic trough-based CSP plant range size is vast, working from 5 to 280 MW; and the technology is considered mature, as well as the operation and management of these systems. In fact, with reference to the Solar Energy Generating System (SEGS) built in California between 1984 and 1991 and still operative, the power plant operating life already exceeded 25 years with a minimum drop of performance. The approximate capacity under construction worldwide is about 700 MW. One of the most trending

applications of parabolic trough is the Integrated Solar Combined Cycle, where the Solar Power Plant is integrated with a fossil fueled power plant in order to guarantee a 24/7 production without the TES need (see Paragraph 2.1.5).

Linear Fresnel Reflector is another example of line-focus concentrator. The base working principle is very similar to the parabolic trough: a mirror reflects the direct sun radiation on a receiver tube, placed above the reflectors plane. Unlike the parabolic trough, the mirrors parabola is achieved by approximating the shape with several almost flat linear mirrors, which are placed on a fixed horizontal structure. The mirrors follow the sun path along its East-West path via one-tracking systems and they are aligned on the North-South axis. The mirrors underlying land is free and partially overshadowed by the mirrors themselves. The shaded area can be grown in desert climates and allow the fauna transit (Figure 2.3) in any case. For this reason, the land usage required by Linear Fresnel Reflector is better tolerated by the public opinion, with respect to other technologies.

Figure 2.3. Linear Fresnel Reflectors at San Nicolò d'Arcidano (Italy) (source: http://www.linkoristano.it)

The receiver is placed several meters above the mirror plane, it faces downwards and it can be provided with a secondary reflector, in order to increase its conversion efficiency. An important advantage with respect to Parabolic Trough is that the receiver tube is fixed, and this simplifies the support structure and permits the use of fixed joints. The system simplicity is rewarded by low investment costs, and consequent lower Levelized Cost Of Electricity (LCOE).

Linear Fresnel Reflectors are potentially able to use the same Heat Transfer Fluids of the parabolic trough, but the direct steam generation seems to be the best choice for this technology. The direct generation of superheated steam up to 500 °C allow very high conversion efficiencies and no need of extra heat exchangers, with a further reduction of the investment cost. Nevertheless, these systems present serious control issues and require complicated storage of saturated liquid.

The largest Solar Power Plant based on Linear Fresnel Reflectors is the 125 MW Indian Reliance Power project [34], connected to the grid in November 2014. All around the world, 179 MW of Linear Fresnel Reflectors are operational, with an expected annual electricity production of 350 GWh, while the capacity of power plants under construction reaches 180 MW [25].

The Linear Fresnel Reflector technology is increasingly being used also for direct thermal applications, in the temperature range between 100 and 250 °C [31] for industrial process, domestic water production, air cooling, desalination and other uses.

Central receiver system is the best example of the point-focus concentrators. They are composed of a Solar Field of heliostats, which are rectangular mirrors that individually track the sun on two axes and concentrate the radiation on a *solar tower* (another name that distinguishes this technology). The solar tower height depends on the Solar Field area: the bigger the SF area is, the higher the tower (common height is over 100 m). As for the parabolic trough, the collected energy heats a HTF, which can be steam, air or molten salt. Steam and air can be directly used to feed a steam or a gas turbine, while molten salts require a heat exchanger upstream the Power Block section. This technology allows

reaching concentration ratios of 600-1,000 and therefore HTF temperatures are the highest among solar systems (over 1,000 °C). Thanks to this, the overall conversion efficiencies of solar tower plants are the highest and the storage sizes can be reduced, because the media is stored at higher temperatures with respect to other cases. Installed power of Central receiver plants is around one tenth of parabolic troughs (500 MW), and their annual expected electricity production is about 1,300 GWh [25]. 392 MW out of the total 500 MW installed represents the commercial Ivanpah Solar Electric Generating System, operative from 2013 (Figure 2.4).

Figure 2.4. Ivanpah Solar Electric Generating System (source: http://www.businesswire.com)

The capacity under construction is about the same of the installed capacity, confirming the increasing trend of this technology. With the first plants built is 1980s, 35 years of experience confirm the solar tower as a mature technology.

Dish Stirling systems use reflective parabolic dishes to focus the sunlight onto the central focal point of the parabola. In the same point, a

receiver produces thermal energy, which is therefore used in a Stirling engine.

Among solar technologies, the Dish-Stirling is the less used. In fact, only two power plants are currently listed on the NREL international catalogue [35], and only one is operational: the Maricopa Solar Project of 1.5 MW was decommissioned in 2011, while the Tooele Army Depot of 1.5 MW is operational in Utah.

2.1.4. Thermal Energy Storage

Thermal energy storage systems allow the storage of heat (or cold) for a later use. TES are very useful in all those applications where a mismatch between energy production and use exists.

Generally, it is possible to divide TES systems in *active* and *passive* systems. In the *active* systems the storage medium flows in the heat exchangers and the main heat transfer occur via forced convection, while in the *passive* systems the storage media does not circulate and the heat transfer occurs via natural convection or buoyancy forces (due to density gradients) [36]. Two-tank systems, thermoclines and steam accumulators are examples of active storage, while systems with embedded or enhanced heat transfer structures or packed bed are examples of passive applications. Active storage systems can be further classified in *direct* and *indirect* systems. In the direct systems, the HTF is used also as storage medium, while in the indirect systems, a second medium is used for the heat storage [37].

Another classical type of classification for TESs is according to the nature of the stored heat: sensible, latent or thermo-chemical.

In *sensible heat storage systems*, thermal energy is stored by raising the temperature of a solid or a liquid media (not gases due to their very low volumetric heat capacity). A large number of materials are available in any required temperature range, and therefore the selection of the storage material is usually made according principally to its heat capacity and considering the available space for the storage section. Among liquid media, a very promising option is represented by the molten salts (even for an HTF usage, as aforementioned): in fact, these mixtures mostly composed of $Na(NO)_3$ and KNO_3 are liquid at atmospheric pressure, they present operating temperatures compatible with the current turbines, they are not inflammable nor toxic, they have an excellent thermal stability at high temperatures, low chemical reactivity, low viscosity and low vapour pressure (allowing them to be used in vertical storages). The main drawback of molten salts is that they freeze in a temperature range between 120 °C and 220 °C. The worst effect of their high freezing point is the damage of receiver tubes, heat exchangers and generally all the containers where they flow or are stored. For this reason, their

implementation requires the adoption of electric resistances or supplementary heaters to avoid this solidification, reducing the conversion efficiency, complicating the plant and making the costs rise.

Table 2.1 reports the properties of molten salts in comparison with other sensible storage materials (the last three even recycled), suitable for CSP applications [38][39].

Table 2.1. Sensible storage materials for CSP applications.

Material	**Density kg/m^3**	**Specific heat, J/kg·K**	**Cost, €/kWh (ΔT=100 °C)**
Molten salt	900-2,600	1,500	14
Saturated water (250 °C, 40 bar)	798	4,865	-
Mineral oil (< 320 °C)	800	2,400	15
Synthetic oil (< 400 °C)	755	2,400	60
Colafite (recycled)	3,120	800-1,034	0.4
Castable ceramics (recycled)	3,500	866	188
High temp. concrete (recycled)	2,750	916	3

Latent heat storage systems are based on the heat absorption and release that occur during a phase change. Phase Change Materials can store up to fourteen times [40] more heat per unit volume than sensible heat storage materials such as water, masonry, or rock. The phase change can occur in different forms, but solid–liquid transition is the most economically attractive option because it causes the smallest changes in volume.

With respect to other techniques, latent heat TES is particularly attractive due to its high-energy storage density and its possibility to store the heat at the constant temperature corresponding to the phase transition. A large number of PCM are known to melt with a heat of fusion in a wide range of temperatures.

Thermo-chemical storage systems exploit the heat produced during an endothermic chemical reaction, where the energy associated with a reversible reaction is required for the dissociation of the chemical species. Materials used for this storage systems have higher energy densities with respect to PCM and sensible storage media [37] and for this reason they can provide the most compact energy storages, even if at the highest costs.

A comparison of the technologies based on the above-mentioned classification (sensible, latent and thermochemical) is reported in Table 2.2 [40].

Table 2.2. Comparison of different TES systems.

	Sensible	**Latent**	**Thermochemical**
Temperature range	up to: 50 °C (Aquifers and ground storage) 110 °C (Water tanks) 300 °C (Sand-rock-mineral oil) 400 °C (Siliconic oil, Concrete) 500 °C (NaCl, solid) 700 °C (Cast steel) 1200 °C (Magnesia fire bricks)	-100 ÷0 °C (Water-salt solutions) -50÷0 °C (Clathrates) -20÷100 °C (Paraffins) -20÷80 °C (Salt hydrates) 20÷450 °C (Sugar alcohols) 120÷300 °C (Nitrates) 150÷400 °C (Hydroxides) 350÷750 °C (Chlorides) 400÷800 °C (Carbonates) 700÷900 °C (Fluorides)	180 °C (Iron carbonate) 200÷300 °C (Metal hydrides) 250÷400 °C (Magnesium oxide) 400÷500 °C (Ammonia) 800÷900 °C (Calcium carbonate) 500÷1000 °C (Methane/water) 2000÷2500 °C (Metal oxides Zn and Fe)
Energy density	Small ~ 50 kWh/m^3 of material	Medium ~ 100 kWh/ $m^3$of material	High ~ 500 kWh/ $m^3$of material

Storage period	Limited (thermal losses)	Limited (thermal losses)	Theoretically unlimited
Lifetime	Long	Often limited due to storage material cycling	Depends on reactant degradation and side reactions
Technology status	Industrial scale	Pilot scale	Laboratory scale
Advantages	Low cost Reliability Simple application with available materials	Medium storage density Small volumes Short distance transport possibility	High storage density Low heat losses (storage at ambient temperature) Long distance transport possibility High compact energy storage
Disadvantages	Significant heat loss over time (depending on insulation) Large volume needed	Low heat conductivity Corrosiveness of materials Significant heat loss (depending on level of insulation)	High capital cost Technically complex

Thermal Energy Storage in Concentrating Solar Power Systems

In the field of power generation, the most interesting Thermal Energy Storage application are the *time-shifting* of energy production and their coupling with Renewable Energy Systems, often coupled in the same application.

As it is well known, electrical energy demand strongly varies during the day, being characterized by periods of peak and base-loads.

During the last decades, not only strong variations of demand have been influencing the grid stability, but also variations and uncertainties are more and more present even in the energy supply, due to the not-dispatchable RES plants. Accordingly, nowadays *dispatchable* power stations, which are rarely renewable, are designed for capacities sufficient to fulfil both the peak of load and the lack of supply. Consequently, power station working points are ever more frequently placed in off-design or hot-standby areas, with high operational costs and large CO_2 emissions.

A more efficient power generation management could be achieved if storing the energy production until a demand peak, and this can be achieved via TES systems [41]. TES systems are charged during the off-peak periods and discharged during the peaks, reducing the load request to the grid. Doing so, power stations could be not-oversized and operational costs could be reduced.

CSP Plants join the energy production from renewable sources with the possibility to achieve a time-shifting at a relatively low-cost, through the exploitation of their TES. TES are aimed to compensate the variability of the solar resource throughout the day and to provide power even during the night. In fact, the heat collected during sunshine hours and not immediately used for power generation can be stored for a night (or generally, later) use.

The selection of the optimal storage system for a CSP Plant is generally made considering the specific characteristics of the plant, and in particular the working fluid, the storage capacity, the temperature range, the power level and the reaction time [39]. As an example, Figure 2.5 shows the characteristic temperature range for various sensible heat storage concepts.

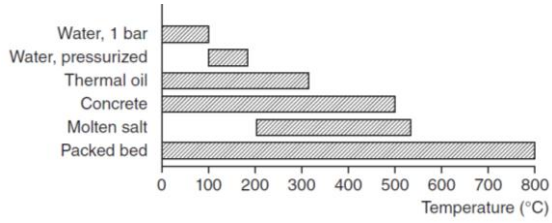

Figure 2.5. Characteristic temperature range for various sensible heat storage concepts (source: [39])

With the intention of giving the reader an idea of the operational TES systems in CSP applications, Table 2.3 reports some of the TES implemented worldwide from the 1980s to our days [39][35].

Table 2.3. Operational TES systems in CSP applications.

Project	Concept	Concentrator type	Max temp.	Thermal capacity	Year
Eurelios (Italy)	Two-tank molten salt	Tower/heliostat	430°C	0.5 MWh_{th}	1981
SSPS (Spain)	Two-tank liquid sodium	Tower/heliostat	530°C	1.0 MWh_{th}	1981
Solar One (USA)	Thermocline with thermal oil	Tower/heliostat	300°C	28 MWh_{th}	1982
Solar Two (USA)	Two-tank molten salt	Tower/heliostat	565°C	110 MWh_{th}	1996
PS10 (Spain)	Steam accumulator	Tower/heliostat	245°C	20 MWh_{th}	2006
Andasol-1 (Spain)	Two-tank molten salt	Trough	385°C	1 GWh_{th}	2009
Gemasolar (Spain)	Two-tank molten salt	Tower/heliostat	565°C	2.3 GWh_{th}	2011
Arenales (Spain)	Two-tank molten salt	Trough	393°C	7 hours	2013
Ait-Baha (Morocco)	Packed-bed of rocks	Trough	570°C	5 hours	2014

2.1.6. Power generation system

Once listed the different concentrators used to convert the solar power in useful thermal energy and described the main methods to store the thermal energy, the present paragraph discusses on the technologies adopted in CSP applications to convert the thermal energy in useful work: the power generation systems.

Steam Rankine Cycle systems

Steam turbines used in Rankine cycles are the most common power generators worldwide. Consequently, their knowledge is deep and their maturity has been proven by thousands of industrial applications. For these reasons, and for the facility of coupling them with CSP systems, the vast majority of the existing CSP plants use Rankine cycles.

In a Rankine cycle, the feedwater is compressed to high pressure, boiled and superheated; the superheated steam is expanded to low pressure in a multi-stage turbine that drives a generator. After the expansion, the low-pressure steam is condensed and the water is pressurized again.

Since the turbines' efficiency is strongly influenced by the temperature and the pressure at their inlet, these systems are fully exploited when coupled with solar systems that allow very high steam temperatures. Solar towers allow to reach a maximum admissible inlet temperature of about 700 °C, while linear concentrators maximum temperatures are about 500-550 °C. For these reasons solar tower systems adopt uniquely steam turbines (in the range of 100-150 MW [35]); while linear concentrators usually use steam turbines only if the power plant capacity is greater than 5 MWe (the typical range is 15-150 MW) or if the HTF is water (Direct Steam Generation, DSG).

With respect to steam thermal power stations driven by fossil fuel, steam plants driven by solar resource are subject to more variable and rapid loads and to more frequent off-design situations. For these reasons, the manufacturers developed steam turbines, which are able to reach the full power in half an hour, specifically for CSP applications, that can therefore be characterized by conversion efficiencies around 40% [39].

From an economic point of view, larger systems cost less per unit of power. Nevertheless, larger systems must be coupled with larger Solar Fields, and an optimization carried out by [39] between savings and costs associated to bigger thermal losses in the Solar Field has led to define the size of 250 MWe as the best trade-off against turbine sizes.

Organic Rankine Cycle systems (ORC)

Organic Rankine Cycle units are power generation systems using organic fluids characterized by a low temperature boiling point and a high molecular mass. Typically used fluids are Toluene, Heptane, Pentane, R123, R134a and others, chosen case by case depending on their characteristics. The organic fluid evolves in a Rankine cycle, where it is evaporated (isobaric), expanded (isentropic) in a turbine (or, generally, in an expander device) and then condensed (isobaric) again (Figure 2.6).

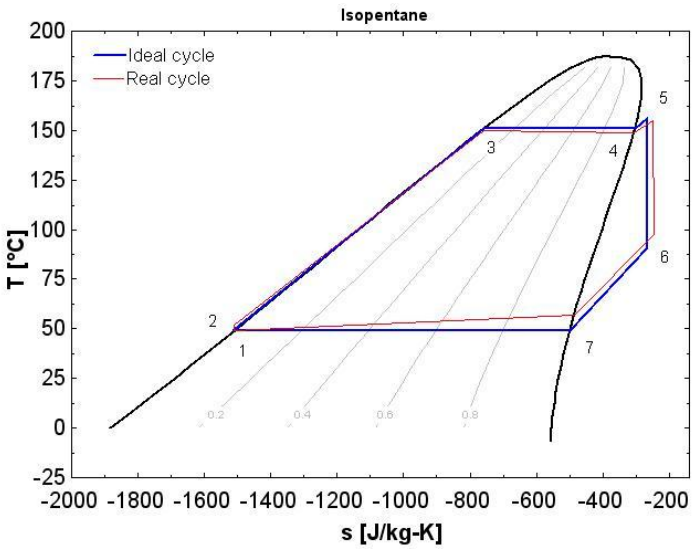

Figure 2.6. Ideal and real ORC (Isopentane) in a Temperature - Entropy diagram.

The most efficient ORC systems follow a regenerated Rankine Cycle: in this case, the fluid enthalpy at the expander outlet is still high and it can be used to pre-heat the organic fluid upstream the evaporator.

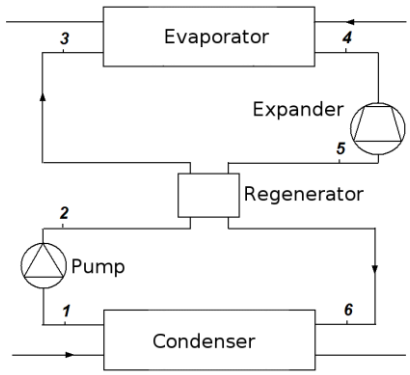

Figure 2.7. Scheme of a Regenerated Rankine Cycle system.

ORC units present the advantage, with respect to steam systems, to be fed with low temperature heat sources (from 100°C up to 350°C) keeping relatively high thermal to electric conversion efficiencies (around 20%). Their versatility allows them to be installed in a wide range of sizes (typically, the range of power goes from 5 kW to 5 MW [42]), and for this reason they seem to be a good choice for distributed generation systems based on renewable energy sources (mainly biomass, geothermal and solar energy).

The world interest toward ORC units in smart grids or distributed power generation is increasing also because the production of electricity by using a rotating machine allows the supply of important ancillary services as grid voltage support, frequency response, regulation and spinning reserves.

Nowadays, the total ORC installed capacity for commercial applications is 2.7 GWe, in 563 power plants [43]. Of this, the geothermal source of heat is the biggest (76.5%), followed by biomass (10.7%) and heat recovery. ORC systems coupled with solar technologies are only 0.1% of the total installed capacity. The world leader manufacturer is ORMAT (65.7%), followed by Turboden (12.6%) and Exergy (9.8%) [43]. The planned capacity for future units is around 525 MWe in 75 plants.

United States of America present the largest installed capacity per country, followed by Turkey and New Zealand. These countries benefit from their geothermal resources. Italy occupies the 8th place in the

installed capacity per country, but its ORC energy sources are mainly biomass and heat recovery.

Usually, ORC units are the most adopted power generators for CSP plants with capacities under 5 MWe.

Other applications

Apart from the conventional technologies of steam turbines and ORC units applied to the CSP field, new applications are being studied nowadays: Brayton cycle turbines fed with air or supercritical CO_2 heated up to 1,000 °C seem to be very challenging alternatives to boost the solar tower overall system efficiency, while Integrated Solar Combined-Cycle Plants can be a good solution to reduce the CO_2 emissions and increase the performance of existing Combined Cycle Gas Turbine (CCGT) plants. Integrated Solar Combined-Cycle Plants add a solar steam generator upstream the waste heat recovery system of a CCGT in order to operate the turbine with an increased amount of steam [44].

2.1.7. Costs

Concentrating Solar Power Plants costs have presented a substantial reduction in the recent years. A cost reduction of industrial power plants can be generally provoked by both technology improvements and scale-up effects. Considering that the scale-up effect did not occur for this kind of plants yet, the cost decrease can be mainly attributed to technology improvements. For these reasons, a scale-up effect activation can really lead to a deep further cost reduction. According to [25], it's very difficult to state the exact costs for CSP Plants components, because of the differences in technologies and plant sizes. In any case, some cost ranges, reported in [25], are introduced, together with some drivers for cost reductions.

The Solar Field cost is approximately between 160 and 250 Euro for square meter, including the HTF. This value is foreseen to be reduced in the next ten years, adopting collectors with larger apertures (trough) and improving the optics and the field layout. Moreover, the automatization of the industrial processes and the standardized design, as well as higher reflectivity and cleanliness can lead to a deeper cost reduction.

The Thermal Storage cost is about 26-30 €/kWh_t and the main driver for the cost reduction is the usage of a direct storage concept, as well as higher temperature differences.

The Power Block section cost is around 720-765 €/kWe and the interesting thing is that a price raise is foreseen for the future, instead of a reduction. This is mainly because of the technological improvements, corresponding to higher process temperatures, lower parasitic consumption and CSP-adapted turbine design.

Considering the overall CSP Plant, the today investment cost is averagely around 4,287 €/kWe [25]. This average cost strongly varies depending on the technology: typical investment costs for LFR in OECD countries are in the range of 3,200-6,200 €/kWe and PTC costs are between 3,700 and 7,500 €/kWe [45].

The investment cost of a coal supercritical power station is between 1,200 and 1,700 €/kWe [46], while the investment cost for a Combined Cycle Gas Turbine is around 500 €/kWe. The investment cost of a CSP plant is higher even with respect to nuclear, whose cost is about 4,000 €/kWe. Among renewable energy sources, photovoltaic cost (ground mounted) is about 900-1,600 €/kWe and wind power (onshore) is about 1,000-1,800 €/kWe.

In conclusion, CSP is currently a very expensive technology for producing power, and this is the main reason why more and more countries are promoting feed-in tariffs to support the technology diffusion and the so-called scale-up effect.

With reference to the Italian case, electricity generation by CSP Plants is supported through feed-in tariffs whose values are around 0.30 €/kWh over a period of 25 years [47]. In the case of hybrid plants, feed-in tariffs only apply to electricity generated from the only solar source.

The Solar Power Plants eligible for support have to meet some requirements of not toxicity of the materials used, size of the TES section (at least 1.5 kWh/m^2), and minimum Solar Field dimension of 2,500 m^2.

However, the investment cost trend of CSP is foreseen to decrease in the future, reaching a value of 3,485 €/kWe in 2020 and 2,814 €/kWe in 2030 [25].

2.1.8. New applications

CSP technologies can be extended to a large number of other applications, different from electricity production.

The heat produced through the solar energy conversion can be used for both medium and high temperature industrial thermal processes. According to [48], about 27% of the heat required by several industrial sectors is at medium temperature (100-400 °C), and 43% is necessary above 400 °C. Solar thermal process heat can be easily produced in these temperature ranges, depending on the type of the solar concentrator. The suitable sectors for concentrating solar thermal plant applications are many, and they comprehend paper, plastics, chemical, distilleries, food and beverages, pharmaceutical, buildings heating and cooling, refineries and so on. Nowadays, 95.5 MWh_t of solar thermal plants for industrial applications are operative worldwide (in the number of 132 plants) [49].

Another not-negligible aspect of solar thermal plants for industrial applications, apart from their renewable nature, is that at the end of their life, their components can be safely recycled and reused, because they do not include hazardous materials.

Desert areas are the best for solar applications but, as it is well known, they usually lack of freshwater. For this reason, the use of concentrating solar in desalination processes seems to be a very interesting application.

A new way of producing energy for transport applications from renewable sources is the so called “solar fuels” field. The solar fuels can be generated either via a solar reforming of natural gas or a solar driven gasification of carbonaceous. The process occurs thanks to the heat from the solar resource, which drives the necessary endothermic chemical reactions that transform the fossil fuel into a refined fuel.

Hydrogen is considered as the cleanest energy carrier, but nowadays over 90% of it is produced from fossil fuels. To make hydrogen life cycle totally clean, hydrogen could be produced only from water and solar energy, and this represents the European vision for 2050 [50].

2.3. Concentrating Photovoltaic

Concentrating Photovoltaic technology combines the photovoltaic effect with the optical capacity of mirrors to concentrate light. The sun rays are concentrated onto little photovoltaic cells and depending on the concentration-ratio, or *number of suns*, CPV systems can be distinguished in Low Concentration Photovoltaic (LCPV) Medium Concentration (MCPV) and High Concentration Photovoltaic (HCPV). LCPV systems have a number of suns between 1.25 and 40; while HCPV between 250 and 1700 suns [39]. As it happens very often, the reasons of the *joint-venture* between high concentrating optics and photovoltaic is economic. The CPV technology had been developed for space applications, and during the first 1990s it has been thought to extend this technology to a terrestrial environment. Since the cell costs were very high, their only feasible use was HCPV. Nevertheless, the CPV only entered the market in 2000s [51].

Nowadays, about 360 MWp of CPV systems are grid-connected worldwide, and several plants exceeded the capacity of 30 MWp [51].

More than 90% of the documented installed capacity of CPV is in the form of High Concentrating Photovoltaic with two-axis tracking, due to their solar cell very high efficiencies (46%) [51]. For this reason, other technologies are not going to be examined in deep by the author. An High Concentrating Photovoltaic device is mainly composed of a support for either a mirror or a CPV array with its framework. CPV systems can track the sun by means of vertical and horizontal axis actuators (Figure 2.8). The possibility to track the sun in two axis allows large electricity productions even during the late part of the day, when the energy demand is considerably high.

The photovoltaic effect occurs only if the photon energy equals or exceeds the bandgap of the material. As well known, the solar spectrum is composed of photons having different wavelengths (and related energies). In order to maximize the sun energy conversion, special multi-junction (or diode) cells have been developed: every junction is made of a different material and therefore a different bandgap, which can convert sunlight of a certain wavelength. The *triple-junction* is the most widely photovoltaic

cell adopted in HCPV, and it is composed of a lattice-matched GaInP (indium, gallium and phosphorus), GaInAs (gallium indium arsenide) Ge (Germanium) triple junction solar cell.

The research and development of this technology is mainly focused toward the increase of solar cell efficiency. A promising datum is the solar cell efficiency growth during the last 14 years, which is about 0.9% absolute growth per year. Researchers are studying new combinations of materials in order to further increase the efficiency.

Figure 2.8. High Concentrating Photovoltaic (Ottana Solar Facility)

Chapter 3

The Ottana Solar Facility

Every data reported in the present chapter is part of the definitive project for the Ottana Solar Facility and it can be found on http://www.enas.sardegna.it.

3.1. Introduction and objectives

A synergy between the Sardinian water supply system (ENAS[1]) and the main regional research center (Sardegna Ricerche), in collaboration with the industrial development consortium of Central Sardinia decided to build the innovative renewable power plant named Ottana Solar Facility, motivated by three objectives: ENAS wanted to reduce its energy purchase costs by producing a part of its requested energy itself, the industrial development consortium of Central Sardinia desired to support new businesses and Sardegna Ricerche wanted to test the new technologies of the project on a pilot scale. The Department of Mechanical, Chemicals and Materials, which the author is affiliated to, and the Department of Electrical and Electronic of the faculty of Engineering of the University of Cagliari, have been involved as scientific support partners.

[1] Ente Acque della Sardegna

In the Ottana Solar Facility, whose budget was around €13,000,000, a concentrating solar photovoltaic system, provided with an electro-chemical battery, is integrated with a CSP Plant, provided with a TES. The two different energy storage concepts were thought for different purposes: the Thermal Energy Storage is characterized by a slow dynamic response, and therefore was conceived for a long-term storage (and a corresponding energy production during long absences of solar radiation); while the electro-chemical battery has a very fast dynamic behaviour, and therefore was designed to be used to compensate the frequent variations of the solar source while producing electricity as constantly as possible.

The Ottana Solar Facility is placed in the industrial district of Ottana (40°14'18.9"N 8°59'37.7"E) and the entire project was aimed to demonstrate the advantages of integrating different solar technologies and different energy storage concepts. The main idea was to enhance the dispatchability of Solar Power Plants, and to obtain pre-determined power profile curves, depending on the market request and on the weather forecast. The current national regulation does not consider Solar Power Plants as dispatchable, and this is the reason why the target of the present research was to assess the dispatchability of hybrid CSP-CPV plants in order to get them closer to the possibility of being considered as dispatchable and therefore able to supply ancillary services.

Figure 3.1. Ottana Solar Facility: plant layout and position. (source: Google Maps)

3.3. Power Plant layout

With reference to the alternative technologies for the CSP sub-systems, described in the previous chapter, the design choices for the Ottana Solar Facility CSP section are summarized in the following.

Considering the land area available for the plant, the budget of the project and the design capacity of the plant, an ORC unit has been considered as the best choice for the power generation section. The relatively low temperatures requested by the ORC unit allowed a Linear Fresnel Concentrator-based Solar Field to be chosen, coupled with a thermal oil as Heat Transfer Fluid. The choice of the thermal oil, instead of newer and more innovative solutions (i.e. pure water) was reinforced by the intention to facilitate the management and to avoid the electrical consumptions (and plant complications) of the electrical resistances needed to keep melted the PCM. The Solar Field layout has been selected, as well as the line number and length, in order to produce the necessary flow of hot oil at a temperature compatible with its specifications. Aiming to minimize the energy losses through heat exchangers, a direct two-tank system has been set for the Thermal Energy Storage section, allowing using the HTF also as storage medium.

Including the CPV section, the Ottana Solar Facility has a nominal power output of 1 MWe and consists of a 600 kWe CSP Plant based on Linear Fresnel Reflectors using thermal oil as Heat Transfer Fluid, a two-tank Thermal Energy Storage system (capacity of 15 MWh), an Organic Rankine Cycle Power Block, a 400 kWe CPV power plant and an electrochemical storage system with a capacity of 430 kWh.

Figure 3.2 shows the simple conceptual scheme of the Ottana Solar Facility abovementioned.

The Concentrating Solar Power section of the Ottana Solar Facility includes three main sub-sections (Figure 3.3): the Solar Field, the Thermal Energy Storage system and the Power Block.

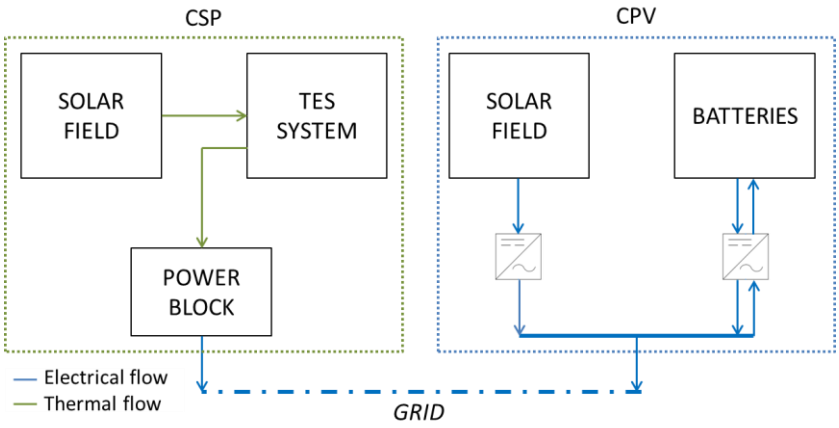

Figure 3.2. Conceptual scheme of the Ottana Solar Facility

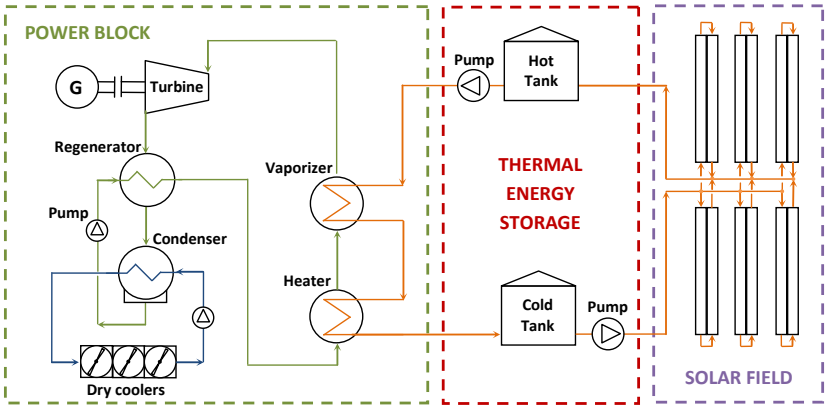

Figure 3.3. Simplified scheme of the CSP Section.

3.3.1. Solar Field

The Solar Field is composed of 6 lines of Linear Fresnel Reflectors (LFR), each 200-meter-long (Figure 3.4), connected in a configuration known as central feed. The receiver includes a secondary reflector that redirects the incoming solar rays towards the evacuated receiver tube.

Figure 3.4. Ottana SF of the CSP Section.

The Solar Field Heat Transfer Fluid is a commercial Dowtherm®-T thermal oil. The inlet and outlet temperatures, determined in the design phase of the Ottana Solar Facility, were 150°C and 260°C and the total mass flow was 17.3 kg/s (under the design conditions of a DNI of 900 W/m^2, an air temperature of 17 °C, an elevation of 73°, and an azimuth equals to 0°).

All the results and simulations obtained and reported in the present thesis are referred to the design data, reported in Table 3.1. However, it should be noticed that the winner project of the competitive public tender for the construction of the Ottana Solar facility has a SF outlet temperature of 275°C and an inlet temperature of 165°C.

Table 3.1. Main operating parameters and assumptions of the SF.

Technical data	
Collecting area	8,400 m^2
Land area	10,800 m^2
Line length	200 m
Lines distance	5.00 m
Focal length	4.9 m
Cleanliness efficiency	98%
HTF inlet / outlet temperature	150/260 °C
HTF mass flow	17.3 kg/s
Tracking system consumption	1 W/m^2 mirror
Circ. pump consumption	9.5 kW
Diameter main pipeline	DN 125
Pipeline insulation thickness	0.08 m
Receiver Tube (AISI 304 – austenitic stainless steel)	
Reference optical efficiency	62%
Density	8030 kg/m^3
Thermal conductivity	20 W/(m·K)
Specific heat	0.50 kJ/(kg·K)
U_1 thermal losses coefficient	0.056 $W/m^2 \cdot K$
U_2 thermal losses coefficient	2.13·10-4 W/m^2K^2
HTF (Dowtherm® T)	
Density	763 kg/m^3
Thermal conductivity	0.110 W/(m·K)
Specific heat at constant pressure	2439.4 J/(kg·K)
Dynamic viscosity	0. 5 mPa·s

The installed receiver tube is an Archimede HCEOI12 (Figure 3.5) whose specifications can be found in [52]. It is composed of an internal tube of austenitic stainless steel with lapped external surface. An external borosilicate glass covers the tube and its anti-reflective spectrally selective coating allows a very high transmittance of solar radiation (96.6%) and a thermal emissivity of about 8.5% at 400°C. Between the steel and the glass tubes, a vacuum annulus is created. Special bellow couplings connect in series the requested number of receiver tube sections (each section has a length of 3,900 mm) to form a receiver line. Each line is supported by a rail, which permits the longitudinal thermal expansion due to temperature increase. The collector lines are aligned along the North-South direction and they are equipped with a single-axis tracking system to follow the sun's path.

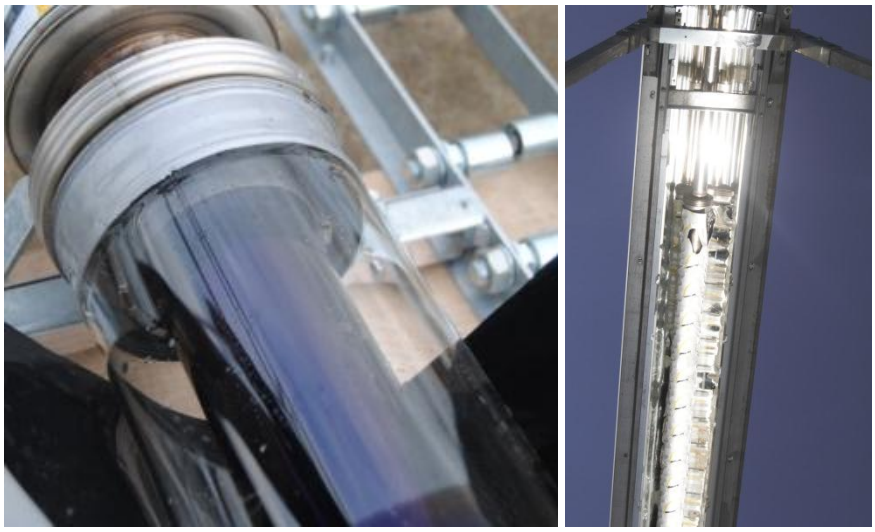

Figure 3.5. Archimede HCEOI12 receiver tube

3.3.3. Thermal Energy Storage

The Thermal Energy Storage of the Ottana Solar Facility is based on a two-tank active direct sensible system using thermal oil as storage medium (Figure 3.6).

The upper part of the tank, above the oil, is filled with Nitrogen. The Hot Tank collects the oil leaving the Solar Field and supplies it to the Power Block; the Cold Tank receives the oil coming from the Power Block, collects it and supplies it to the Solar Field. The two-tank thermal insulation materials are mineral wool (walls), foam glass (bottom) and calcium silicate (roof). Both the wall and roof insulation layers are covered by a thin aluminium sheet. Technical data of the TES can be found in Table 3.2

Figure 3.6. TES of the Ottana Solar Facility (under construction)

Table 3.2. Main operating parameters and assumptions of the TES.

Tank useful volume	330 m^3
Thermal oil mass	195 t
Storage capacity	4.9 h (14.6 MWh_t)
Insulation layer thickness – walls	0.5 m
Insulation layer thickness – roof	0.5 m
Insulation layer thickness. – bottom	0.25 m
Inner diameter	11 m
Inner height	3.5 m
Outer tank surface emissivity	0.35
Outer tank surface emissivity	0.3
Oil emissivity	0.95
Outer tank solar absorptivity	0.66
Pump consumption	5.2 kW

3.3.5. Power Block

The Power Block section of the Ottana Solar Facility is represented by an ORC unit that follows a regenerated Rankine cycle, provided by the Italian Turboden® and characterized by the technical data reported in Table 3.3.

Figure 3.7. ORC power unit of the Ottana Solar Facility.

Table 3.3. Main operating parameters and assumptions of the ORC Unit.

Thermal power input	3,000 kW
Condenser power output	2,350 kW
Oil inlet/outlet temperature	263/153 °C
Minimum up time	3 h
Oil mass flow	11.1 kg/s
Captive power consumption	26 kW
Gross electric power	559 kW
Net power output	533 kW

3.3.6. Cooling section and auxiliary equipment

The cooling section of the Ottana Solar Facility is represented by an air-cooled condenser, which dissipates a nominal thermal power of 2,350 kW through the cooling of a water flow of 200 m^3/h from 35 °C to 25°C (design conditions).

Table 3.4. Main operating parameters of the air-cooled condenser.

Thermal power	2,350 kW
Water nominal flow	200 m^3/h
Water inlet/outlet temperature	35/25 °C
Design air temperature	17 °C
Min/max air temperature	2/34 °C
Number of refrigerators	4
Power of a single refrigerator	600 kW
Power consumption	14.4 kW

Among the auxiliary equipment, the main operating pumps of the Ottana Solar Facility are variable-speed centrifugal pumps with inverter. They feed the oil in the cold and hot circuits of the thermal oil and the water in the air-cooled condenser circuit. The redundancy is ensured by two equal pumps connected in parallel for each circuit.

Since the circuits are represented by different piping sections and lengths, as well as fluid conditions, the pumps are different. Their main characteristics are reported in Table 3.5.

Table 3.5. Centrifugal pumps characteristics.

Hot oil circuit (DN 125)	
Flow rate	80 m^3/h
Pressure	300 kPa
Power consumption	11 kW
Cold oil circuit (DN 100)	
Flow rate	54 m^3/h
Pressure	260 kPa
Power consumption	7.5 kW
Cooling water circuit (DN 200)	
Flow rate	230 m^3/h
Pressure	150 kPa
Power consumption	15 kW

All the circuits are sectioned by a large number of shut-off valves. Regarding the oil circuits, these valves are installed at both the inlet and outlet sections of each solar field loop, at the inlet and outlet sections of the solar field main pipelines, at the inlet and outlet sections of each tank and at the inlet and outlet sections of the power block. Obviously, shut-off valves are placed even upstream and downstream of each pump.

Balancing valves are installed at each loop inlet and at the main pipeline of the oil flowing toward the solar field.

Temperature, pressure and flow rate measurers and transmitters are installed at the inlet/outlet of all the sections of the plant.

An expansion vessel of 100 l (at 6 bar) is installed in the cooling water circuit and a tank of 6,000 l allows the storage of the Nitrogen that fills the top of each tank of thermal oil.

3.3.7. Concentrating Photovoltaic

The Concentrating Photovoltaic power plant section is composed of 37 two-axis solar trackers (Figure 3.8, Figure 3.9), with an overall peak power output of about 400 kW_p. The grid connection is established in medium voltage (three-phase).

Figure 3.8. CPV field of the Ottana Solar Facility (under construction)

Figure 3.9. CPV field of the Ottana Solar Facility (under construction)

The optics is based on the Fresnel technology, which has reached technological and commercial maturity. Each solar tracker includes 48 modules, sectioned in two strings that are connected to a dedicated three-phase DC/AC converter provided with two independent MPPT (Maximum Power Point Tracking) systems. The tracking system is equipped with a four-quadrant solar sensor and an on-board meteorological station, which measures Direct Normal Irradiance and wind speed. Such data are used by the tracker controller to continuously follow the sun's position, together with information about the astronomical ephemerides.

Owing to the high variability of the power production from CPV modules, a battery bank (Figure 3.10) based on Sodium-Nickel is introduced for short-term energy storage. In particular, the capacity of the battery bank is designed to allow programmable generation of the CPV system in 30 s time intervals and to compensate for forecasting errors.

Table 3.6 contains the main design parameters of the CPV plant.

Figure 3.10. Sodium-Nickel battery bank of the Ottana Solar Facility (under construction)

Table 3.6. Main design parameters of the CPV power plant.

CPV module	
Optics technology	Refractive
Solar cells technology	Triple-junction
Geometric concentration factor	500 suns
DC efficiency	25%
Maximum DC power	225 W_p
Battery bank	
Battery/Chemistry Type:	$NaNiCl_2$
Number of batteries	24
Battery bank capacity	430 kWh
DC/DC efficiency	94%
Min/Max State-of-charge	10% / 90%
DC/AC converter	
Nominal Efficiency	97%
N° independent MPPT	2
Overall CPV Plant	
Overall efficiency	22%
Net peak power output	400 kW_p at 850W/m^2

Chapter 4

Hybrid system simulation models

The target of the present Ph.D. research was to study the performance of medium-size hybrid CSP-CPV systems designed for improving the dispatchability of Solar Power Plants and to develop and optimize novel management strategies for this kind of plants.

The simulation tool developed for this purpose and described in the present chapter allows predicting the hybrid CSP-CPV system performance, responses and behaviours starting from the weather conditions and from the plant technical specifications.

In addition, different management strategies are herein proposed for both the only CSP section and for the overall hybrid CSP-CPV system.

4.1. Concentrating Solar Power

To the author's knowledge, most of the scientific literature on Concentrating Solar Power is focused on interesting potential evaluations, performance assessments, feasibility and techno-economic analysis carried out under steady state conditions. As illustrated in the previous chapters, CSP is not a new technology, and its history and evolution presented highs and lows during the past decades, basically following the oil and gas prices. Probably, this is the main reason why only few studies have been carried out on the automatic control [53] and dynamic

simulation [54] of entire CSP systems. To the author's viewpoint, the lack of dynamic studies can be also justified because the simulation models have been mainly used for feasibility and economic assessment so far, and not for control purposes. In addition, the latest control systems are programmed with advanced learning ability functions: during the very first moments of operation, power plants are run in a learning mode and they basically *learn* and acquire transfer functions for the main performance parameters, making this way complexes dynamic models useless for the practical everyday operation. Moreover, these *auto-learnt* transfer functions are tailored on the precise power plant, and therefore their precision is surely better than the one obtainable through numerical models, based on approximations and assumptions. Nevertheless, the auto-learning mechanism presents three main disadvantages: it can be started only if the power plant exists and it is operational, it cannot be used for a different power plant, and it does not provide complete information to understand dynamic phenomena or to optimize the system.

In the specific study of the hybrid CSP-CPV system, the innovative concept of the Solar Facility together with its purposes, made stronger the system-level research interest.

The CSP Plant can be mainly subdivided in three main subsystems: the Solar Field, the Thermal Storage section and the Power Block.

The LFR-based Solar Field of the CSP Solar Field has been modelled for different research purposes. Yearly, daily and hourly-based analysis have been carried out, and for this reason the degrees of accuracy of the developed models are different and suited for the analysis that was ongoing on that moment.

- A one-dimensional steady-state model has been developed under Matlab® for the yearly and weekly-based simulations.
- A non-stationary one-dimensional model has been developed under Matlab Simulink® for minute, hourly and daily-based simulations.
- A non-stationary two-dimensional model has been developed under Comsol® environment to compare and verify the results obtained through the one-dimensional unsteady model.

The model for the Thermal Energy Storage, based on the two-tank concept, allows to assess the thermal losses and performance of the TES section taking into consideration the technical characteristics and the design parameters of the apparatus and the heat and mass exchanges which occur internally and externally to its control volume.

The Power Block section simulated is based on an Organic Rankine Cycle unit produced by Turboden®. These devices are tailor-made on the specific requests of the customer, and they can be defined using the system theory concept of black boxes, because of company secrets. Furthermore, the target of the research was not to develop a dynamic model of the Power Block. For these reasons, the Power Block behaviour has been simulated through the complete efficiency curves provided by the manufacturer.

4.1.1. Solar Field

4.1.1.1. One-dimensional steady-state model

The one-dimensional steady state simulation model of the LFR-based Solar Field developed by the author [55], is used to evaluate the net thermal power output on an hourly basis as a function of solar radiation and solar position, for given values of the main geometrical and technical characteristics of the solar collectors, as well as for assigned thermodynamic properties of the HTF. In particular, the thermal power output $\dot{q}_{SF}$ is evaluated by taking into account the optical losses of the collector $\dot{q}_{Opt}$, the thermal losses of the receiver tube $\dot{q}_{L,tube}$ and those of the main pipes $\dot{q}_{L,pipe}$:

$$\dot{q}_{SF} = S_c DNI - \dot{q}_{Opt} - \dot{q}_{\mathrm{L},tube} - \dot{q}_{L,pipe} = \dot{q}_{RCV} - \dot{q}_{L,tube} - \dot{q}_{L,pipe} \quad (1)$$

In particular, the thermal power concentrated onto the receiver tube $\dot{q}_{RCV}$ has been evaluated by means of the following equation:

$$\dot{q}_{\mathrm{RCV}} = S_c \; \mathrm{DNI} \; \eta_{\mathrm{opt,REF}} \; \mathrm{IAM_L} \cdot \mathrm{IAM_T} \; \eta_{\mathrm{end}} \; \eta_{\mathrm{CLN}} \quad (2)$$

where S_C is the collecting area, $\eta_{opt,REF}$ is the reference optical efficiency (which takes into account of both reflectors) IAM_L and IAM_T are the longitudinal and transversal components of the Incidence Angle Modifier (IAM), η_{end} is the end-loss optical efficiency and η_{CLN} is the surfaces cleanliness factor. The two IAM components were assumed starting from manufacturer information [56,57] and their trends are reported in Figure 4.1 as a function of the incident angle.

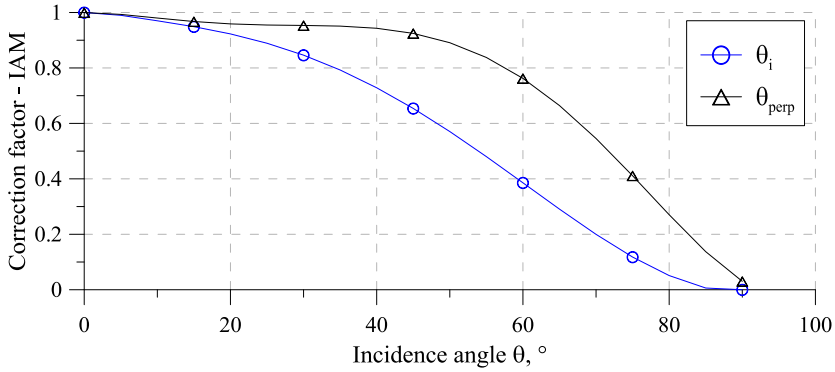

Figure 4.1.Incidence angle correction factors (IAM)

The incidence angle θ components can be defined as:

$$\theta_{\perp} = \text{arctg}\,(\sin(\xi)/\text{tg}(\varphi)) \tag{3}$$

$$\theta_{i} = \arcsin(\cos(\varphi)\cos(\xi)) \tag{4}$$

where ξ represents the azimuth and φ the solar elevation.

End losses η_{end} are calculated according to [58] as:

$$\eta_{end} = 1 - \tan(\vartheta_i) \cdot \frac{l_{focus}}{l_{receiver}} \tag{5}$$

where l_{focus} is the focal length and $l_{receiver}$ is the length of the receiver.

The thermal losses $\dot{q}_{L,RCV}$ are evaluated in function of the temperature difference ΔT_{RCV} between the average oil temperature in the receiver tube and ambient temperature:

$$\dot{q}_{L,RCV} = \left(U_1 \cdot \Delta T_{RCV} + U_2 \cdot \Delta T_{RCV}^2\right) \cdot S_C \quad (6)$$

where U_1 and U_2 are specific coefficient given by the manufacturer (Table 3.1) and S_C is the surface of the collectors. The thermal losses $\dot{q}_{L,pipe}$ are also evaluated in function of the temperature difference ΔT_{PIPE} between oil and air:

$$\dot{q}_{L,pipe} = U_{pipe} \cdot S_{pipe} \cdot \Delta T_{PIPE} \quad (7)$$

where U_{pipe} is the overall heat transfer coefficient and S_{pipe} is the outer surface of the pipe. The heat transfer coefficient U_{pipe} was evaluated by considering the heat convection between oil and internal pipe wall, heat conduction through the pipe wall and the insulation layer and the heat convection from the outer surface to the ambient air.

The Solar Field is connected to the Thermal Energy Storage section as well to the Power Block section through a piping system made of (insulated) stainless steel. In order to evaluate the thermal exchanges that occur among the piping, the oil flowing inside it and the environment, a simplified simulation model has been developed. The model takes into account the incoming solar radiation, the external convection between the piping and the environment, the conduction between the outer and inner walls of the piping and the internal convection between the piping and the oil.

The incoming solar radiation has been calculated as

$$\dot{q}_{sun,PIPE} = DNI \sin(\zeta)\, \alpha\, S_{PIPE,sun} \quad (8)$$

where ζ is the zenith angle, α is the absorptivity of the surface and $S_{PIPE,sun}$ is the piping area facing toward the sun. The latter has been considered as the external diameter of the piping section multiplied for the piping length.

4.1.1.2. Non-stationary one dimensional model

The one-dimensional mathematical model for the Solar Field is based on the mass, momentum and energy conservation equations applied to the control volume shown in Figure 4.2.

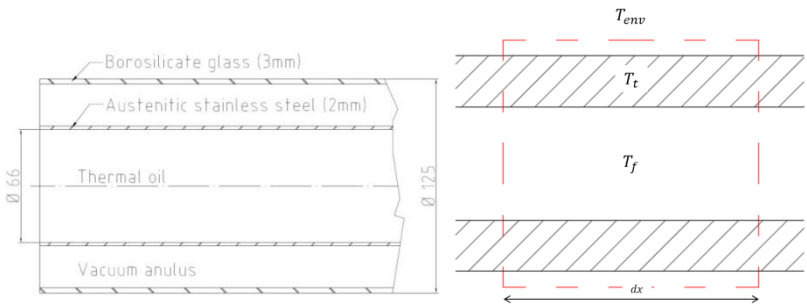

Figure 4.2 Control volume considered in 1D model.

The resulting energy and mass balance equations are:

$$\frac{\partial}{\partial t}\left[\rho S\left(e+\frac{u^2}{2}+gz\right)\right]dx+\frac{\partial}{\partial x}\left[\rho uS\left(e+\frac{u^2}{2}+\frac{P}{\rho}+gz\right)\right]dx=\dot{w}_s+\dot{q}_{sun,RCV} \quad (9)$$

$$\frac{\partial}{\partial t}(\rho S)+\frac{\partial}{\partial x}(\rho uS)=0 \quad (10)$$

The kinetic and potential energy terms have been neglected, shaft work exchanged by the control volume is zero, no mass accumulation occurs inside each control volume ($\rho = const$), and a constant cross section area was considered. The model has been discretized considering three sub-systems characterized by the following thermal state: environment T_{ENV},

receiver tube T_{RCV} and fluid T_{HTF}. The energy balance equations applied to fluid and receiver tube are:

$$C_{HTF}\ \frac{dT_{HTF}}{dt} = R_{RCV,HTF}\ (T_{RCV} - T_{HTF}) - \dot{m}\ c_{p,HTF} \frac{\partial T_{HTF}}{\partial x}\ dx \quad (11)$$

$$C_{RCV}\ \frac{dT_{RCV}}{dt} = \dot{q}_{sun,RCV} - \dot{q}_{L,RCV} - R_{RCV,HTF}\ (T_{RCV} - T_{HTF}) - \kappa_{c,RCV}\ S \frac{\partial T_{RCV}}{\partial x} \quad (12)$$

where $R_{RCV,HTF}$ is the equivalent thermal conductance between tube and fluid, which is calculated as:

$$R_{RCV,HTF} = h_{RCV,HTF}\ \pi\ D_{RCV,int}\ dx \quad (13)$$

The $h_{RCV,HTF}$ convective heat transfer coefficient is obtained from the Dittus-Boelter equation, under the hypothesis of a turbulent flow ($Re \gtrsim 10000$), Prandtl number range ($0.6 \leq Pr \leq 160$), $L/D \gtrsim 10$ and a smooth inner tube surface:

$$Nu = 0.023\ Re^{0.8} Pr^{n} \quad (14)$$

where $n = 0.4$ if $T_{RCV} > T_{HTF}$ and $n = 0.3$ elsewhere.

4.1.1.3. Non-stationary two-dimensional model

A two dimensional axisymmetric numerical model has been developed in the COMSOL® Multiphysics platform to simulate the SF line [59]. The system has been modelled considering the thermo-fluid dynamics behaviour of the entire domain. The domain was reported in Figure 4.3(a) and discretized using a structured (mapped) mesh (Figure 4.3(b)) composed of 10^5 elements with maximum size of 10 mm.

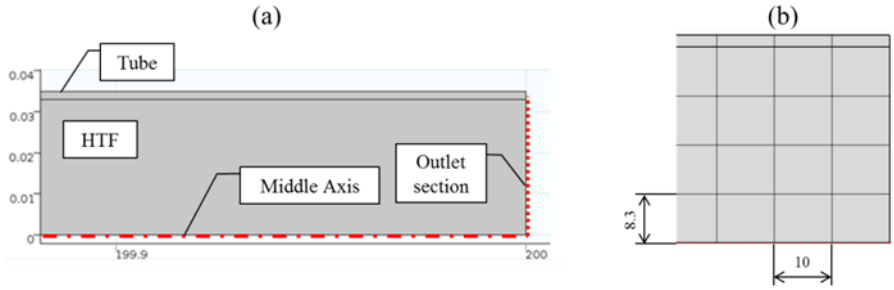

Figure 4.3 Domains of the 2D model (a) and particular of the mesh adopted (b).

A mesh independent study has been carried out considering the different mesh types reported in Table 4.1 and no appreciable differences in the results (in the range of 1 °C) were observed using finer o different type of meshes.

The COMSOL Multiphysics platform was run on a ASUS workstation with I7 Quad-Core CPU and 12 GB memory was 3600s.

Table 4.1. Comparison of the different mesh types adopted.

Case	Type	Duration of the simulation (Real time)	Physical time	Number of elements
1	mapped	3,600 s	19,572 s	$1.0 \cdot 10^5$
2	mapped	3,600 s	29,921 s	$1.5 \cdot 10^5$
3	mapped	3,600 s	34,014 s	$2.3 \cdot 10^5$
4	triangular	3,600 s	4,108 s	$1.7 \cdot 10^6$

The axial temperature evolution of the HTF over the time was evaluated along the dash-dot red line shown in Figure 4.3, which represents the axisymmetric line of the domain. The temperature evolution at SF outlet was evaluated at the intersection point between the red dash-dot and the red dotted line of Figure 4.3(a), representing the central point of the outlet section.

Reynolds-Averaged Navier-Stokes (RANS) equations based on k-ε turbulence model were used to solve the flows through the solar receiver. Continuity and momentum equations are coupled with two additional transport equations involving the turbulent kinetic energy k, and the turbulent dissipation rate ε_T. In the following equation set, the subscript f is for HTF.

$$\frac{\partial \rho_f}{\partial t} + \nabla \cdot (\rho_f u_f) = 0 \tag{15}$$

$$\rho_f \frac{\partial u_f}{\partial t} + \rho_f (u_f \cdot \nabla) u_f = \nabla \cdot \left[-P_f l + (\mu_f - \mu_{T,f}) \left(\nabla u_f + (\nabla u_f)^T \right) - \frac{2}{3} \left(\mu_f - \mu_{T_f} \right) (\nabla \cdot u_f) l - \frac{2}{3} \rho_f k l \right] \tag{16}$$

$$\rho_f \frac{\partial k}{\partial t} + \rho_f (u_f \cdot \nabla) k = \nabla \cdot \left(\left(\mu_f + \frac{\mu_{T,f}}{\sigma_k} \right) \nabla k \right) + P_k - \rho_f \varepsilon_T \tag{17}$$

$$\rho_f \frac{\partial \varepsilon}{\partial t} + \rho_f (u_f \cdot \nabla) \varepsilon_T = \nabla \cdot \left(\left(\mu_f + \frac{\mu_{T,f}}{\sigma_\varepsilon} \right) \nabla \varepsilon_T \right) + C_{\varepsilon 1} \frac{\varepsilon_T}{k} P_k - C_{\varepsilon 2} \rho_f \frac{\varepsilon^2 T}{k} \tag{18}$$

The turbulent viscosity is defined by:

$$\mu_{T f} = \rho_f C_\mu \frac{k^2}{\varepsilon_T} \tag{19}$$

where l is the mixing length, C_μ, $C_{\varepsilon 1}$, $C_{\varepsilon 2}, \sigma_k, \sigma_\varepsilon$ are dimensionless model constants [60] [61], and k is the turbulence kinetic energy.

The production term P_k, which represents the rate at which kinetic energy is transferred from the mean flow to the turbulence, is given by:

$$P_k = \mu_{T,f} \left(\nabla u_f : \left(\nabla u_f + (\nabla u_f)^T \right) - \frac{2}{3} (\nabla \cdot u_f)^2 \right) - \frac{2}{3} \rho_f k \nabla \cdot u_f \tag{20}$$

In order to simulate the heat transfer that occurs in the entire domain, the following energy equation was used:

$$\rho C_p \frac{\partial T}{\partial t} + \rho C_p u \cdot \nabla T = \nabla \cdot (k_c \nabla T) + q_{conv} \quad (21)$$

To simulate the incoming solar power, the boundary condition in the outer wall of the solar receiver was assumed as a net heat flux $(\dot{q}_{sun} - \dot{q}_L)/\mathrm{S_{RCV}} = -\mathrm{n} \cdot (-\mathrm{k_c} \nabla \mathrm{T})$ where $\mathrm{S_{RCV}}$ is the total area of this boundary. The heat transfer inside the receiver tube is characterized by conduction while the heat transfer between the receiver tube and the HTF occurs via both conduction and convection. The energy equation (eq.(21)) applied to the HTF is solved using the velocities calculated from eqs. (15) and (16), in order to evaluate the interactions between fluid dynamics and heat transfer phenomena. The specific thermal power q_{conv} takes into account the convective heat transfer between fluid and internal wall of the receiver.

4.1.1.4. Solar Field control strategy

The main target of every Solar Field management strategy is to deliver to the downstream sections the maximum HTF mass flow at the constant design outlet temperature, for any weather condition and HTF inlet temperature.

The present paragraph reports the Solar Field control strategy for the specific case of the Ottana Solar Facility.

As reported in eqs. (1-2), the thermal power collected by the Solar Field is a function of several parameters, some of which vary during the day and across the year (DNI, $\mathrm{IAM_L}$, $\mathrm{IAM_T}$), while others are constant ($\mathrm{A_c}$, $\eta_{opt,REF}$, η_{CLN}). According to these parameters, the thermal power collected by the SF varies over time. For the specific case of the Ottana Solar Facility, the design value for the thermal power collected $\dot{\mathrm{q}}_{\mathrm{RCV,ref}}$, as defined by eq.(2), is around 4,300 kW and it is obtained for a DNI of

900 W/m^2, an air temperature of 17°C, an elevation of 73° and an azimuth of 0°).

Moved by the intention to find the required mass flow $\dot{m}_{SF}$ to be imposed to the pumps in order to maintain the outlet temperature as close as possible to the design value, for each possible combination of $\dot{q}_{sun}$ and $T_{SF,in}$, the non-stationary one dimensional model discussed in the previous paragraphs has been used.

A total of 2,601 simulations have been carried out (until equilibrium) under Simulink® environment imposing to the system values of $\dot{q}_{RCV}$ ranging from 500 kW (≈ 10 % of $\dot{q}_{RCV,ref}$) up to 4,500 kW (≈ 105 % of $\dot{q}_{RCV,ref}$) with a step of 500 kW, values of $T_{SF,in}$ from 20°C to 180°C, with a step of 10°C and values of mass flow in the range between 0.5 (technical minimum) and 4.5 kg/s (maximum for safety), with a step of 0.25 kg/s. Results have been collected, data have been interpolated for $T_{SF,out}$ equals to the design value of 260 °C and the following curves have been obtained: Figure 4.4 and Figure 4.5 report the SF line mass flow required to obtain an outlet temperature $T_{SF,out}$ of 260 °C for different values of $T_{SF,in}$ and $\dot{q}_{RCV}$.

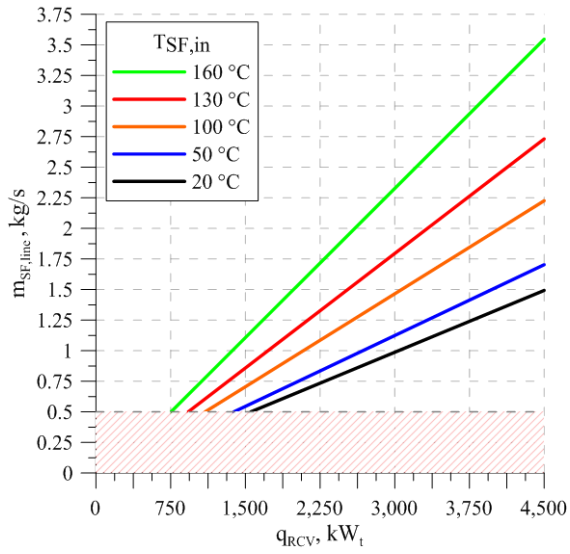

Figure 4.4 Solar Field line calculated mass flow as a function of q_{RCV} for fixed values of $T_{SF,in}$.

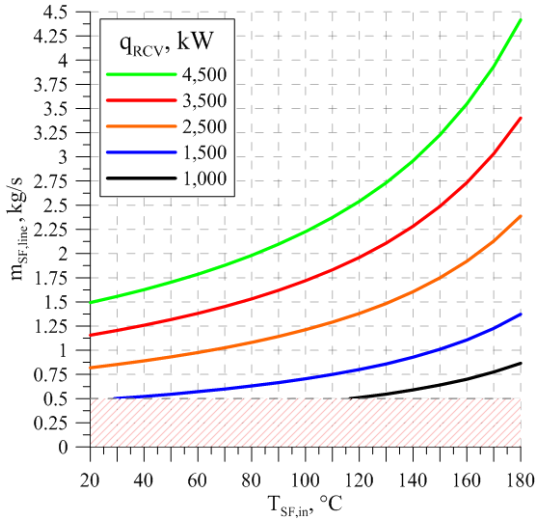

Figure 4.5 Solar Field line calculated mass flow as a function of $T_{SF,in}$ for fixed values of q_{sun}.

The curves shown in Figure 4.4 can be described through the following equation, that calculates the required mass flow for having a $T_{SF,out}$ of 260 °C as a direct function of $\dot{q}_{sun}$ and $T_{SF,in}$

$$\dot{m}_{SF|T_{SF,out}=260°C} = \omega_1(f(T_{SF,in})) \cdot \dot{q}_{sun} + \omega_2\left(f\left(T_{SF,in}\right)\right) \quad (22)$$

Values of ω_1 and ω_2 are reported in Figure 4.6 as a function of the inlet temperature of the Solar Field.

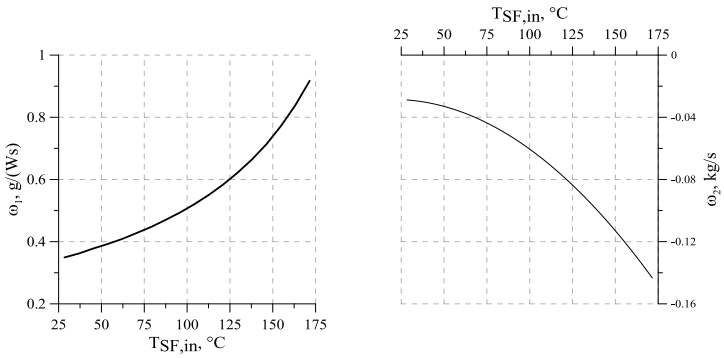

Figure 4.6 Solar field regulation curve coefficients.

4.1.1.5. Recirculation

During the design phase of a line-focus Solar Field, a design choice can be to implement or not a recirculation of the HTF through the SF. The advantage of implementing a recirculation system is that the HTF contained in the SF is pre-heated up to a certain temperature before being delivered to the downstream devices (i.e., a TES), instead of being sent with the temperature of the moment of pumps starting. Doing so, the energy quality of the TES downstream of a recirculated SF can be maintained higher than the case with a not-recirculated SF.

The proposed management strategy for the Solar Field takes into account the possibility to recirculate the mass flow through the Solar Field both partially or totally and including, or not, the Cold Tank in the recirculation. The considered layout is reported in Figure 4.7.

The recirculated mass flow $\dot{m}_{rec}$ is defined by the recirculation factor γ:

$$\gamma = \frac{\dot{m}_{rec}}{\dot{m}_{SF}} \; ; \; 0 \leq \gamma \leq 1 \tag{23}$$

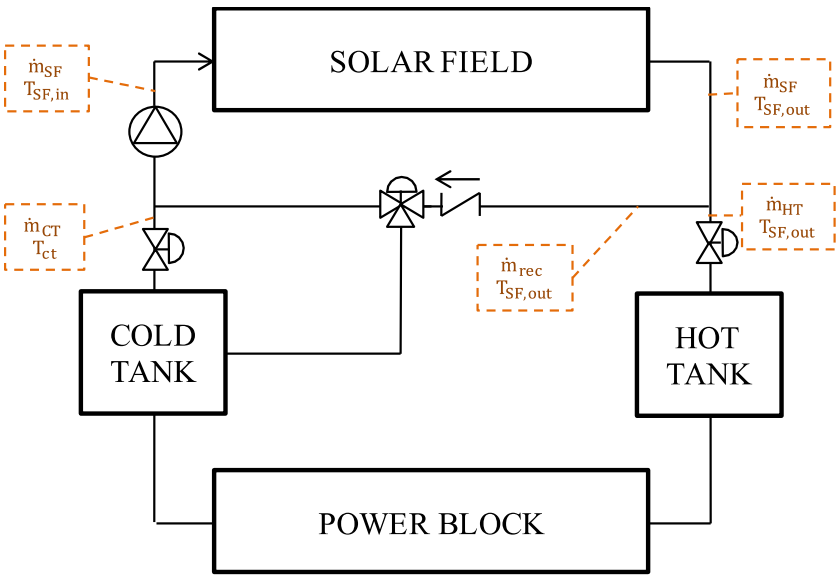

Figure 4.7 Different recirculation strategies layout.

No recirculation occurs when $\gamma = 0$ and complete recirculation occurs when $\gamma = 1$. Intermediate values of γ are obtained by different functions of the Solar Field inlet temperature as reported in Figure 4.8.

In particular, three different recirculation strategy have been tested and compared with the reference case (no recirculation): The different conditions have been indicated as follows:

- A indicates the reference case: no recirculation ($\gamma = 0$).

- B indicates no recirculation $(\gamma = 0)$ for $T_{SF,out} \geq T_{SF,in\ REF}$ and total recirculation passing the Cold Tank $(\gamma = 1)$ elsewhere.

- C indicates no recirculation $(\gamma = 0)$ for $T_{SF,out} \geq T_{SF,in\ REF}$ and total recirculation bypassing the Cold Tank $(\gamma = 1)$ elsewhere.

- D indicates total recirculation bypassing the Cold Tank $(\gamma = 1)$ for $T_{SF,out} < T_{SF,in\ REF}$; partial recirculation bypassing the Cold Tank $(0 < \gamma < 1)$ for $T_{SF,in\ REF} \leq T_{SF,out} < T_{SF,out\ REF}$ and no recirculation $(\gamma = 0)$ elsewhere;

For outlet temperatures of the Solar Field greater or equal than the design outlet temperature, the recirculation factor is zero, in any case.

In the D case, the HTF mass flow coming from the Cold Tank $(\dot{m}_{tank}, T_{ct})$ is mixed with the recirculated mass flow coming from the Solar Field outlet $(\dot{m}_{rec}, T_{SF,out})$. The overall mass flow $\dot{m}_{SF}$ is characterized by the following mass weighted mean temperature:

$$T_{SF,in} = T_{ct}\ (1 - \gamma) + T_{SF,out}\ (\gamma) \tag{24}$$

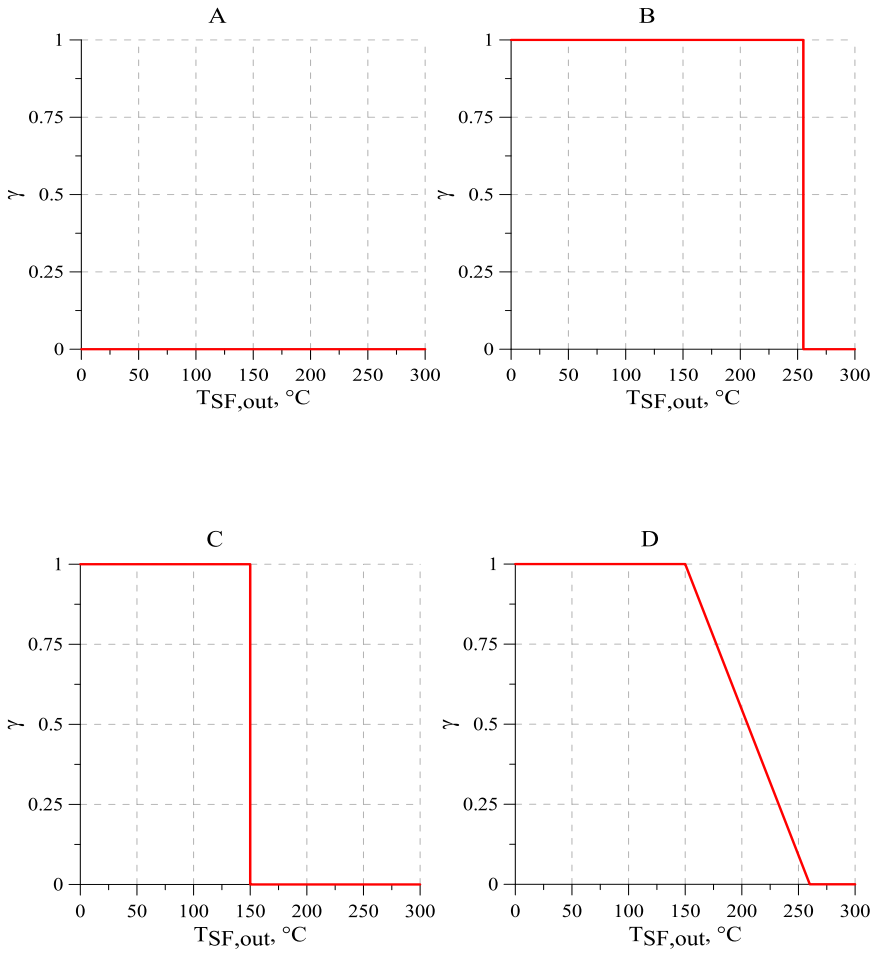

Figure 4.8 Different recirculation strategies proposed.

4.1.3. Power Block

The performance of the ORC unit is evaluated by considering the efficiency curves provided by the manufacturer.

Figure 4.9 shows the ORC oil inlet and outlet temperature, and the oil mass flow as a function of thermal input load. The temperature of the oil at inlet section is constant because the regulation of the ORC is carried out by varying the mass flow.

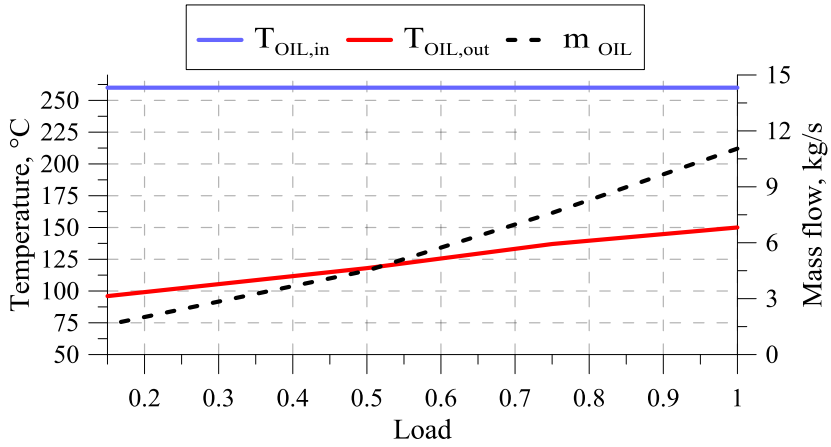

Figure 4.9 ORC oil inlet temperature, outlet temperature and mass flow as a function of the requested load.

Figure 4.10 shows the temperature of the water at the outlet of the condenser in function of the thermal input load and for constant values of both water inlet temperature and mass flow.

Figure 4.11 is probably one of the most representative curves of the ORC section performance: thermal input power and condenser power are shown, as well as the gross and the net electrical efficiencies. These efficiencies differ each other for the auxiliary electric consumptions. The net electric efficiency represents the ratio between the net active electric power output of the ORC and the thermal power input (from thermal oil).

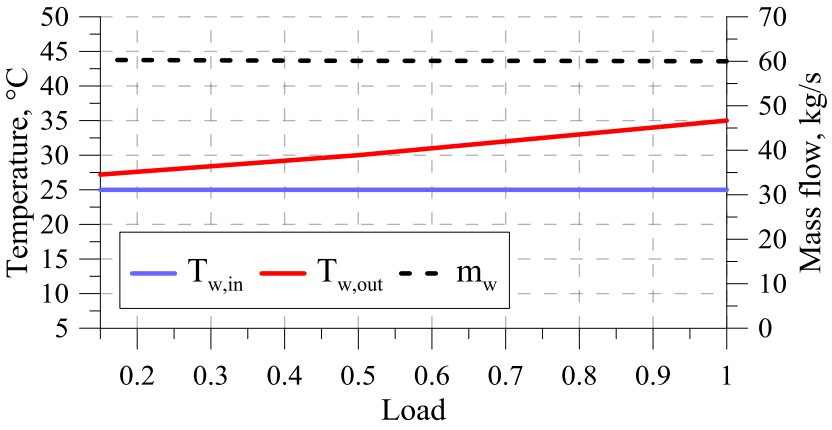

Figure 4.10 ORC cooling water inlet temperature, outlet temperature and mass flow as a function of the requested load.

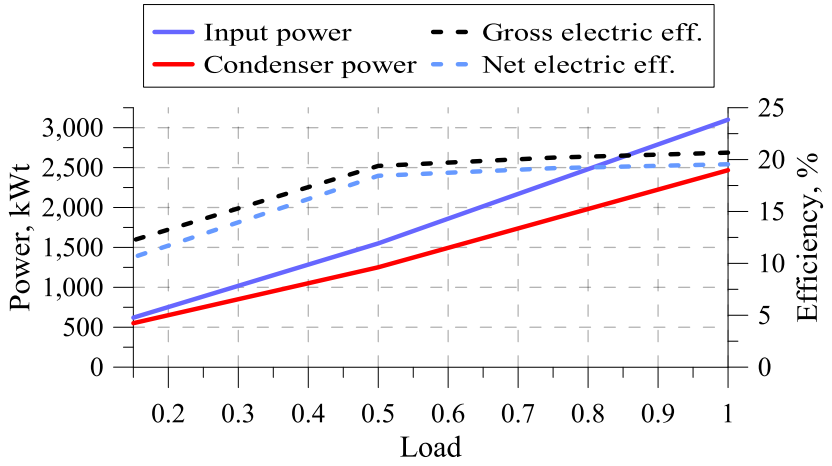

Figure 4.11 ORC input thermal power, condenser power, gross and net electric efficiencies as a function of the requested load.

Figure 4.12 reports the gross electric power produced by the generator and that required to supply the ORC auxiliaries. The net electric power is the difference between the gross electric power and that required by the auxiliaries.

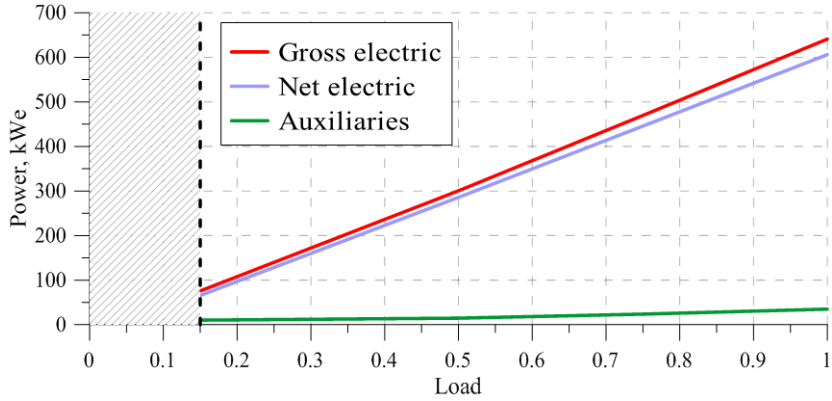

Figure 4.12 ORC gross, net and auxiliaries' electric power as a function of the requested load.

As abovementioned, when coupling ORC units with Solar Power Plants with thermal storages having a capacity of only few hours, their operation is not continuous during the 24 hours, presenting daily shut-downs and start-ups. Depending on both the daily weather and on the state of charge of the TES section, the ORC could be started and turned off several times across a day. Furthermore, during long periods of low DNI, the ORC could be kept off for several days. Moreover, as every rotating machine aimed to produce power, ORC systems require a certain warm-up ramp before being operational. In the evaluation of the ORC behaviours has therefore been considered the start-up phase.

Two different start-up phases have been considered and implemented: cold and warm start-up. The cold start-up occurs when the ORC plant starts after a stop period of more than two days. In this case, all the ORC equipment are cold (especially the heat exchangers) so that they need to be warmed before the starting of the power generation. According to the information provided by the ORC manufacturers, the energy consumption of the cold start-up is evaluated by considering a thermal load request of the ORC system for two-hours at 20-25% of the nominal thermal load. During the start-up periods the ORC does not produce electricity. The warm start-up occurs when the ORC system is still warm because it is re-started after a stop period lower than two days. In this case, the thermal load requested is 25% of the full load for thirty minutes. Moreover, to

avoid a strong reduction of the ORC useful life due to too frequent start up cycles, it has been set that the Power Block can be started-up only if it is able to produce energy at full load for at least three hours.

4.1.4. Thermal Energy Storage

The simulation model of each storage tank provides an accurate evaluation of the heat losses by formulating its energy and mass balance equations. According to the approach proposed by [62], each tank has been modelled by considering two variable control volumes: the oil volume and the overlying nitrogen gas volume. The mass and energy balances allow to evaluate the stored oil mass and the consequent tank wall area in contact with the oil (the wetted wall) and tank wall area in contact with the nitrogen (the non-wetted wall).

As shown by Figure 4.13, thermal losses of the wetted wall are evaluated by considering heat conduction through the insulation layer, heat convection between external wall and air, and wall radiation. Contribution of solar radiation is also considered. Similarly, thermal losses for non-wetted wall and roof are evaluated by considering radiation between the oil surface and the internal walls, heat conduction through the insulation layer, heat convection between external wall and air, wall radiation as well as solar radiation. Finally, bottom thermal losses are evaluated by considering only heat conduction between bottom surface (at bulk oil temperature) and the ground (at an average seasonal temperature). Heat convection between oil and wetted wall is neglected so that the wetted wall temperature equals the bulk oil temperature.

In more detail, the tank thermal losses are given by the sum of the four main components of total heat loss (roof, bottom, wetted and non-wetted walls):

$$\dot{q}_{L,TES} = \dot{q}_{L,TES\ R} + \dot{q}_{L,TES\ bottom} + \dot{q}_{L,TES\ w\ wet} + \dot{q}_{L,TES\ w\ non-wet} \quad (25)$$

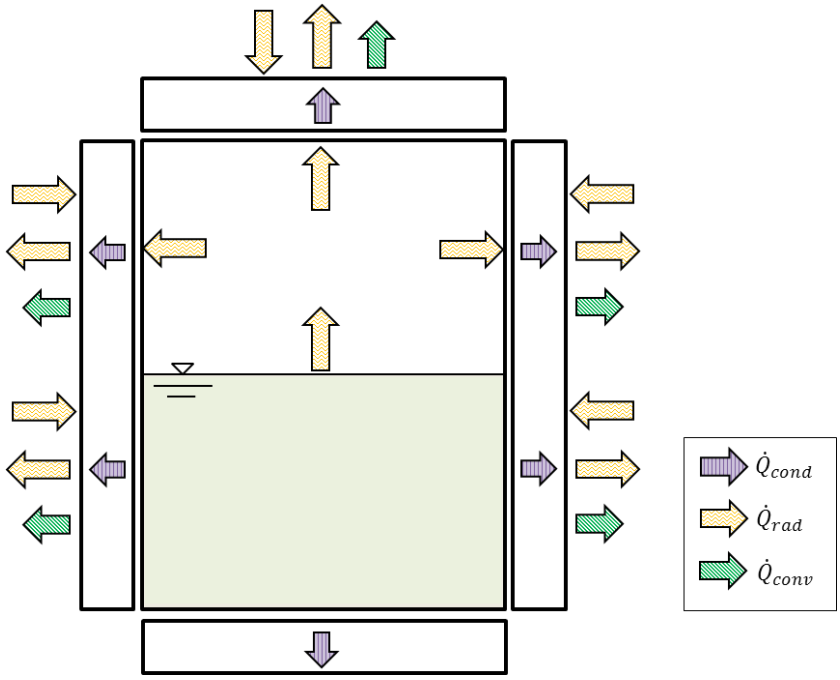

Figure 4.13. Schematics of tanks' thermal losses

Each component is evaluated according to the values of stored oil mass, oil temperature, ambient temperature, wind speed and solar radiation according to the general equation:

$$\dot{q}_{L,TES\,i} = U_i \cdot S_i \cdot \Delta T_i \tag{26}$$

where U_i is the overall heat transfer coefficient, S_i is the heat transfer area and ΔT_i is the difference between internal and external temperatures. The heat transfer coefficients are evaluated by considering the equivalent thermal circuits of Figure 4.14 and Figure 4.15.

Thermal conductivities of the insulation materials are evaluated in function of temperature by means of suitable relationships [62].

Convective heat transfer coefficients are evaluated by calculating the Nusselt number, which is a function of Prandtl and Grashof numbers.

$$Pr = \frac{\mu \cdot c_p}{\kappa} \tag{27}$$

Where κ is the thermal conductivity and μ is the dynamic viscosity.

$$Gr = \frac{g \cdot \beta \, (T_s - T_\infty) \cdot l^3}{\nu^2} \tag{28}$$

Where β is the coefficient of thermal expansion, T_s is the surface temperature, T_∞ is the bulk temperature, l is the characteristic length and ν is the kinematic viscosity.

Considering each component of thermal loss, the thermal equivalent circuit representing the heat transfer throughout the wetted-walls part of the storage tank is shown in Figure 4.14. As previously stated, it has been assumed that the internal wall temperature equals the oil temperature.

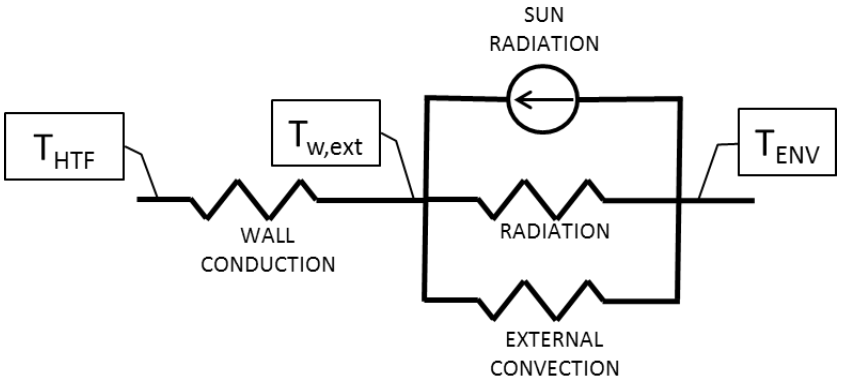

Figure 4.14. Thermal Equivalent Circuit of the wetted wall

Conduction, external convection, external radiation and radiation coming from the sun are taken into account and the adopted equations are discussed in the following.

The wall thermal conductivity is calculated as

$$\kappa_w = 0.037 + 0.0002 \left(\frac{T_{HTF} + T_{w,int}}{2} \right) \tag{29}$$

External convection is calculated considering both forced and natural convection, through a function Ξ = f (Gr) whose value is zero for natural convection, is 1 for forced convection and it assumes intermediate values otherwise. Natural convection occurs when $\frac{\mathrm{Gr}}{(\mathrm{Re})^2} < 0.7$. In this case, when $\mathrm{GrPr} \leq 10^8$:

$$Nu = 0.68 \frac{Pr^{\frac{1}{2}} Gr^{\frac{1}{4}}}{(0.952 + Pr)^{\frac{1}{4}}} \tag{30}$$

Otherwise:

$$Nu = 0.13 \, (Gr \, \mathrm{Pr})^{\frac{1}{3}} \tag{31}$$

Convection is forced when $\frac{\mathrm{Gr}}{(\mathrm{Re})^2} > 10$ and in this case:

$$Nu = 0.3 + \frac{\left(0.62 Re^{\frac{1}{2}} Pr^{\frac{1}{3}} \right)}{\left(1 + \left(\frac{0.4}{Pr} \right)^{\frac{2}{3}} \right)^{\left(\frac{1}{4} \right)}} \cdot \left(1 + \left(\frac{Re}{282000} \right)^{\left(\frac{5}{8} \right)} \right)^{\left(\frac{4}{5} \right)} \tag{32}$$

The global convection heat transfer coefficient is therefore determined as:

$$h = s\, h_{natural} + (1 - \Xi)\, h_{forced} \tag{33}$$

While the radiation heat transfer coefficient ι is defined as:

$$\iota = \sigma\, \varepsilon \left(T_{w,ext} + T_{ENV}\right)\left({T_{w,ext}}^2 + T_{ENV}^2\right) \tag{34}$$

Contribution from solar radiation is calculated differently if considering the tank walls or the tank top:

$$\dot{q}_{sun,TES,w} = DNI \cos(\zeta)\, \alpha\, S_{TES,w} \tag{35}$$

$$\dot{q}_{sun,TES,top} = DNI \sin(\zeta)\, \alpha\, S_{TES,top} \tag{36}$$

The external surface of the tank exposed to the solar radiation $S_{TES,w}$ is calculated as the external diameter of the tank multiplied for the tank height. The not-wetted parts of the tanks (walls and roof) are modelled according to the equivalent thermal circuit represented in Figure 4.15.

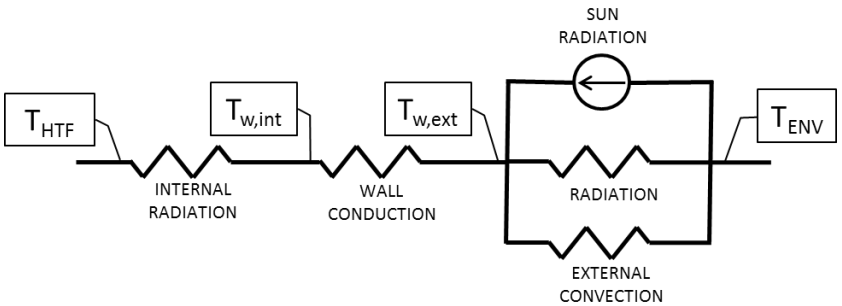

Figure 4.15. Thermal Equivalent Circuit of the non-wetted wall

Referring to the non-wetted volume, the nitrogen above the oil is assumed transparent to heat radiation and with a negligible heat capacity. Therefore, the internal surface temperature of the non-wetted volume (non-wetted wall and roof) is only influenced by heat radiation between oil and surface. The equivalent heat transfer coefficient for this heat radiation was calculated according to specific correlations reported in [63]. The radiation coefficient is calculated as:

$$\iota_{irr} = \frac{\sigma \left(T_{w,int}+T_{HTF}\right)\left(T_{w,int}{}^{2}+T_{HTF}^{2}\right)}{\frac{1-\varepsilon_{HTF}}{\varepsilon_{HTF}}+\frac{1}{F_{HTF,w\,int}}+\frac{(1-\varepsilon_{int})A_{HTF}}{\varepsilon_{int}\,A_{HTF}}} \tag{37}$$

Moreover, the heat conduction through the steel and the aluminium layers is neglected.

The roof convective coefficient is calculated with formulas for an horizontal plate. Thermal conductivity of the calcium silicate composing the roof is:

$$\kappa_R = 0.0674 + (4E^{-5})(\overline{T_{le}}) + (6E^{-8})(\overline{T_{le}})^2 + (9E^{-12})(\overline{T_{le}})^3 \tag{38}$$

Where $\overline{T_{le}}$ is the mean temperature between interior and exterior surface.

The bottom thermal equivalent circuit of the tank is modelled through a conductive resistance between the inner surface temperature (assumed equal to the oil temperature) and the outer surface temperature (assumed to be an average seasonal temperature). Since the storage tank is directly placed on the ground, external convection between the bottom and the environment does not occur.

4.2. Concentrating Photovoltaic

According to the target of the present research, more focused on the Concentrating Solar Power Plant section, and considering that the modelling of the CPV is led by the Department of Electrical and Electronic Engineering of the University of Cagliari, the models developed by the author regarding the CPV and the battery in detail are simplified and they will be substituted by the more complex ones developed by the Department of Electrical and Electronic Engineering.

4.2.1. Generator

The electrical behaviour of CPV systems presents particular features with respect to conventional PV systems due to the use of multi-junction cells and special optics for solar energy concentration.

For this reason, several CPV simulation models have been developed recently, characterized by different levels of complexity and precision [64]. In general, the power produced by CPV modules is influenced by four ambient parameters: Direct Normal Irradiance, air temperature, air mass and wind speed. However, assuming that CPV modules always work at their maximum power point, their power output can be estimated in accordance with the characteristic curves [65] in function of DNI, cell temperature (T_c) and air mass.

The power production of an High Concentrating Photovoltaic system can be predicted, according to the approach proposed by [66], as:

$$P_{CPV} = \frac{P_{REF}}{DNI_{REF}} DNI\ (1 - \omega_{T,c})(1 - \omega_{AM}) \tag{39}$$

Where P_{REF} is the reference power, produced when the DNI equals the reference DNI_{REF} conditions, $\omega_{T,c}$ represents the cell temperature coefficient and ω_{AM} the efficiency losses due to atmosphere depth. This formula can be rewritten considering temperature (χ_T) and air mass (χ_{AM}) coefficients.

$$P_{CPV} = \frac{P_{REF}}{DNI_{REF}} DNI\ (1 - \chi_T(T_{ENV} - T_{ENV,REF}))(1 - \chi_{AM}(AM - AM_{REF})) \quad (40)$$

$T_{ENV,REF}$ and AM_{REF} represent the reference conditions.

The air mass index AM at the sea level can be calculated as a function of solar elevation φ [67]:

$$AM(\varphi) = \sqrt{1229 + (614 \sin \varphi)^2} - 614 \sin \varphi \quad (41)$$

According to [66], the air mass index influence can be neglected when the AM is less or equal than 2. In the other cases, the χ_{AM} value should be evaluated by using a regression analysis on experimental data. Considering that the plant is currently under construction, a value of χ_{AM} = 4.74% has been preliminarily assumed. This is the value obtained by [66] for HCPV modules (Fresnel Lenses) with a concentration ratio of 500 suns installed in Spain.

The values of χ_T are provided by the manufacturer's technical data sheet [68]:

$$\chi_T = \left(-\frac{0.06\%}{°K} \forall\ T_{ENV} < 21°C; -\frac{0.34\%}{°K} \forall\ T_{ENV} \geq 21°C\right) \quad (42)$$

The net power produced by the HCPV system is further reduced by other supplementary losses due to tracking error, soiling, conversion and auxiliaries' consumption. The tracking error causes a reduction of the incident DNI, because the module is not perfectly perpendicular to the radiation. It is a random error, and it can be calculated according to [69] as:

$$\eta_{TRACK} = \cos(random(0.01° - 0.2°)) \quad (43)$$

The soiling (cleaning) losses are strongly influenced by the cleaning frequency, and for this coefficient a value of 0.98 can be assumed [70]. The conversion efficiency curve of the inverter has been introduced and ancillary consumptions are given by the manufacturer [68].

4.2.2. Battery Bank

The available energy content of the electro-chemical battery bank was evaluated by means of its state of charge. The latter is the ratio between the stored energy and its nominal storage capacity and it is determined by monitoring the charging and discharging power flows over time:

$$SOC_{B,t} = SOC_{B,t-1} + \frac{(P_{BC}\eta_B + P_{BD}/\eta_B)\Delta t}{C_B} \quad (44)$$

where η_B is battery efficiency, P_{BC} and P_{BD} are the charging and discharging power flows, C_B is the battery capacity and Δt is the time step. Moreover, as suggested by manufacturers, the batteries were managed by assuming that the battery's state of charge stays within a range between a minimum SOC_B ($SOC_{B,MIN}$) and a maximum SOC ($SOC_{B,MAX}$).

Owing to the capacity limits of the batteries, if the CPV power output exceeds the scheduled value and the batteries are completely charged, a reduction of the CPV power production is required and this power reduction represents a lost power ($P_{CPV,L}$). Therefore, it is possible to introduce an energy balance of the CPV plant that has to be satisfied at each time step:

$$P_{CPV} + P_{BC} = P_{CPV,MPP} + P_{BD} + P_{CPV,L} \quad (45)$$

where P_{CPV} represents the effective power output of the CPV plant, P_{BC} is the power that charges the battery, $P_{CPV,MPP}$ is the power of the CPV at the maximum power point and P_{BD} is the power discharged from the battery.

4.3. Integration strategies of CSP and CPV

As mentioned, the main aim of the research was to assess the capability of Concentrating Solar Power technologies to produce power with programmable and controllable power curves.

While the previous paragraphs reported the models developed for the different sections composing the hybrid CSP-CPV plant and the management strategies related to the only CSP section, in the present paragraph the CSP and CPV integration is discussed for the first time [71]. More in detail, the present paragraph reports some proposed different integration strategies for the optimization of the energy fluxes of the two CSP and CPV sections and related storages.

In order to test and compare the different integration strategies proposed, a requested power output was necessary. In an every-day operation of a hybrid CSP-CPV power plant, a certain power output curve can be either required by the grid operator or proposed by the plant owner.

Since it is difficult to know in advance the power curves that will be required by the grid operator or proposed by the owner to a power plant during the operating phases, the research on the integration strategies was carried out by assuming, for the sake of simplicity, a two-parameter requested power curve.

Each power curve considered is therefore characterized by a *power output* P_{OUT} that is constant for the whole day and a *time duration* τ that depends on the energy availability. Generally, since the solar energy availability for a day is independent from the possible power curves to achieve, the less the power output, the longer the corresponding duration τ.

If the power curve is intended to be proposed by the plant owner, the power curve itself is the output of an optimization process, depending on weather and market conditions. Therefore, the time duration τ of this optimized power curve is the maximum potential duration related to each power output P_{OUT}.

Once determined (imposed or optimized) the power curve to be delivered by the hybrid CSP-CPV during a day, it is necessary to split the

power output between the two sections (CSP or CPV) for each moment of the day. Therefore, two different *control strategies* have been proposed and compared.

In the Full Integration (F-INT) strategy the two CSP and CPV systems operated in a synergetic way to supply the required and fixed power output P_{OUT} ($P_{OUT}(t \in \tau) = const.$). The control system optimizes the share of CSP and CPV power production by maximizing the corresponding potential time duration τ.

In the Partial Integration (P-INT) strategy the two CSP and CPV systems operated independently but always with reference to a single power delivery point. In this case, the control system maximizes the corresponding potential time duration τ for a fixed share of CSP and CPV power productions ($P_{CSP}(t \in \tau) = const.$; $P_{CPV}(t \in \tau) = const.$). Figure 4.16 shows the qualitative power curves for the two aforementioned control strategies for a given power output P_{OUT}.

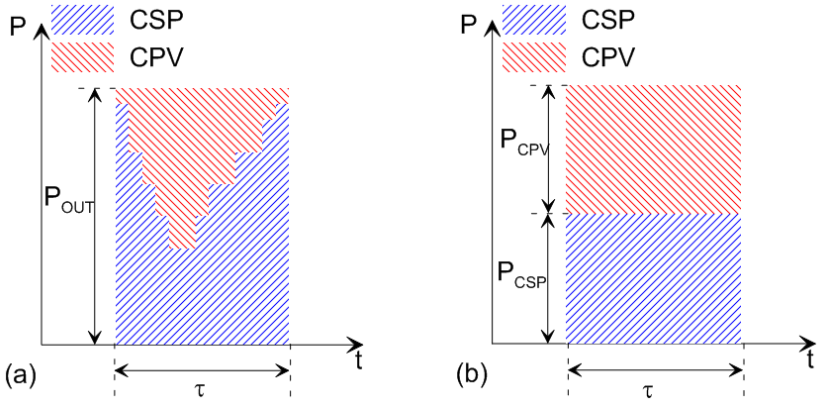

Figure 4.16. Example of output power curve for (a) Full-Integrated and (b) Partially-integrated strategies.

For a given power output, the corresponding time duration τ is determined by optimizing the plant performance with a three-step procedure as shown in

Figure 4.17. During the first step, a simulation model based on the equations described in the previous paragraphs calculates the minute-based daily energy production of the CSP Solar Field ($\dot{q}_{SF}$) and CPV panels ($P_{CPV,MPP}$) assuming weather conditions that are given by the weather service Meteonorm® without considering any weather forecast error. In a second step, the results obtained are used as input data for the optimization of time duration τ referring to a power output P_{OUT} that can be either imposed or optimized. Optimization is carried out day-by-day through a specific algorithm developed under the GAMS environment, using the weather conditions for a certain time horizon and a time step of 1 hour. During this step, the desired power curve is obtained under the constraints given by the operating limits of the different equipment and the energy balance of both CSP and CPV plants. A minimum up-time constraint is also introduced to minimize the number of ORC start-ups during the day together with some simplifications, such as constant TES thermal losses equal to a percentage of the inlet thermal power of the TES, while ORC efficiency curves shown in paragraph 4.1.2 are approximated with a linear piecewise function necessary to solve the mathematical model as a mixed-integer linear problem. Moreover, since the batteries are considered to be used not for a significant power shift, which is made by the TES, but only for a short-term storage and to ensure that the CPV power curve remains constant throughout cloud transients, the role of the batteries is not considered during this step.

In the final step, starting from the output power curve determined in the previous step, a minute-based model refines the GAMS results considering both the actual use of batteries and the real energy losses related to thermal storage and ORC operation.

Therefore, the effective performance of the overall system is assessed.

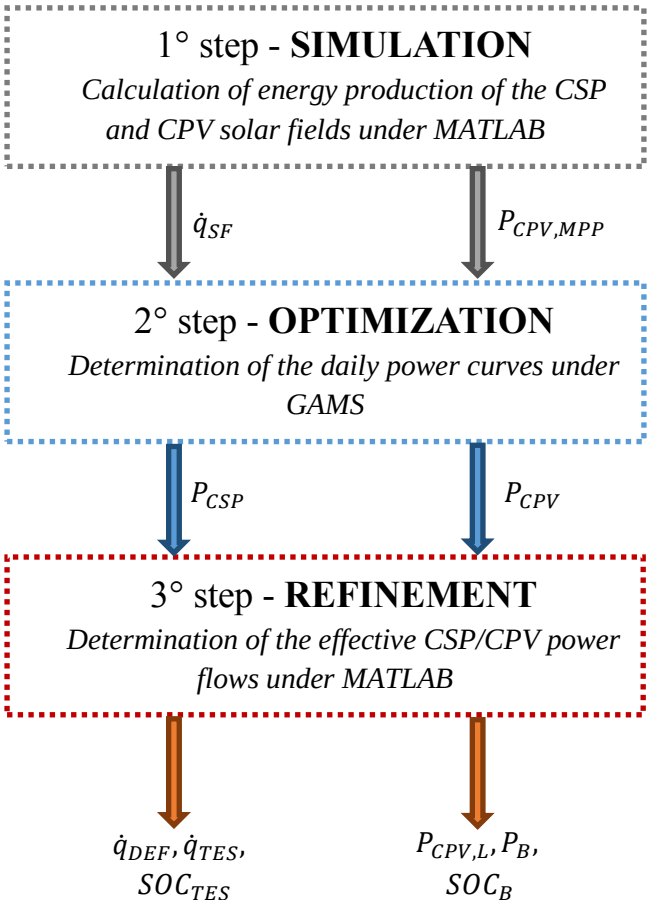

Figure 4.17. Procedure scheme used to simulate the performance of the hybrid CSP-CPV power plant.

Chapter 5

Results

5.1. Concentrating Solar Power Plant

In the following pages are reported the research results related to the performance assessment of a small-size Concentrating Solar Power Plant, obtained through the models described in the previous chapter. The different analysis, comparisons and evaluations have been carried out with reference to the technical specifications and assumptions of the Ottana Solar Facility medium-size hybrid CSP-CPV system.

The first paragraphs consist in the evaluation of the thermal losses occurring in the sections of the CSP, for different time intervals and operating phases. In the following, the results focused on the Solar Field, precisely on its thermo-fluid dynamics phenomena and on its possible operating phases and recirculation strategies. The dispatch capability of the CSP plant closes the report on the Concentrating Solar Power results.

5.1.1. Influence of thermal energy losses on the yearly performance

One of the first studies performed has been an evaluation of the CSP thermal losses related to the main sub-sections of the plant (Solar Field, ORC unit and TES section) [72], whose results are reported in the following.

The thermal losses assessment was carried out during daylight and night periods, as well as during the plant different operating phases (start-up, continuous operation and shut-down). The analysis was performed on hourly basis and for a typical meteorological year. Air temperature and DNI values of the year at the base of the analysis are reported in Figure 5.1 and Figure 5.2.

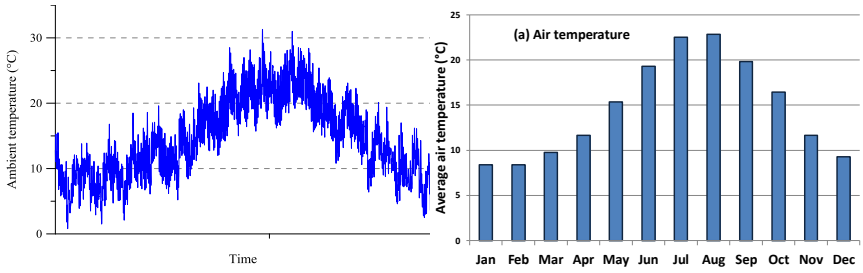

Figure 5.1. Daily and monthly values of air temperature

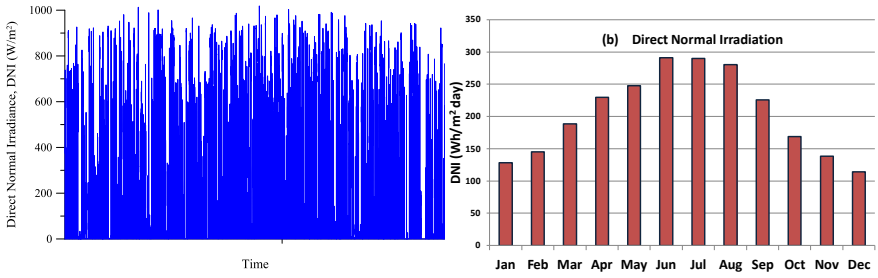

Figure 5.2. Daily and monthly values of DNI

Table 5.1 reports the results of the comparison between the performance of the CSP plant with and without thermal losses (receiver tubes, piping, hot and cold storage tanks, warm up of the Solar Field and the ORC unit).

Table 5.1. Overall energy balance of the CSP plant (Influence of thermal losses on the yearly performance)

	Without thermal losses (MWh/year)	With thermal losses (MWh/year)
Available solar energy	15,038	15,038
Thermal energy to the receiver tube	6,055	6,055
Solar Field thermal losses	0	405
Solar Field net thermal output	6,055	5650
TES thermal losses	0	148
ORC thermal input	6,055	5,502
ORC thermal start-up losses	0	110
ORC useful thermal energy	6,055	5,392
ORC gross energy production	1,174	1,074
Auxiliary electric consumption	133	127
Net electric energy production	1,041	947

Overall, due to the presence of the thermal losses, the average efficiency of the Solar Field, defined as the ratio between the Solar Field net thermal output and the available solar energy decreases from 40.3% to 37.6% and the useful thermal energy of the ORC unit decreases by about 11%. Therefore, the net electrical power production of the CSP plant decreases from 1,041 MWh_e/year to 947 MWh_e/year and the average conversion efficiency, defined as the ratio between the net energy production and the available solar energy decreases from 6.9% to 6.3%.

About 83.5% (78.5 MWh_e/year) of the reduction in the net energy production is due to the thermal losses of the SF and the TES section and about 16.5% (15.5 MWh_e/year) is due to the thermal losses related to the ORC start-up.

Overall, the sum of the thermal losses reported by Table 5.1 gives about 663 MWh_t/year, which is about 4.4% of the available solar energy

or 10.9% of the thermal power concentrated onto the receiver tube. Figure 5.3 shows the distribution of the overall thermal energy losses on monthly basis. As shown by Figure 5.3, during summer months both the receiver and piping thermal losses strongly increase, while the others retain about the same. On a yearly basis, most of the thermal losses (about 61%) are due to the SF receiver tubes (230.6 MWh_t, that is 34.6%) and SF piping (174.7 MWh_t , that is 26.4%). The SF thermal losses can be split between thermal losses that occur during night (or absence of solar radiation) and thermal losses that occur during full operation of the plant.

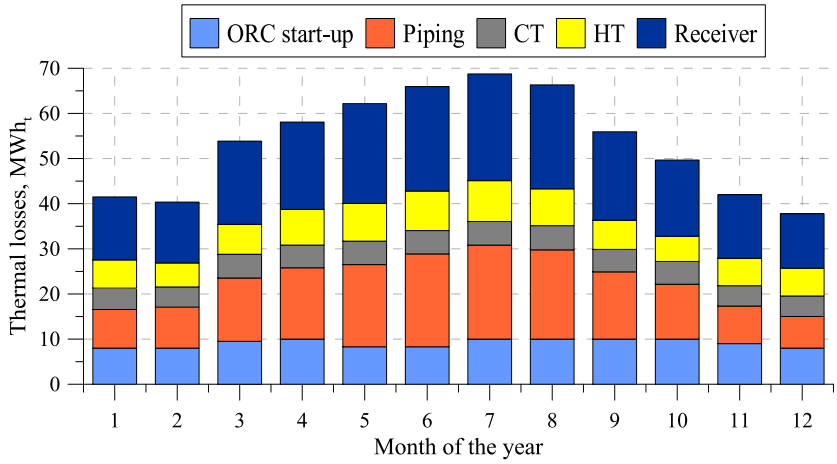

Figure 5.3. Monthly values of thermal losses distribution.

Figure 5.4 reports the monthly distribution of the full operation (day) and night thermal losses of the Solar Field. On a yearly basis, night thermal losses are mainly constant and account for about 20.5% of the overall thermal losses, whilst full operation thermal losses vary strongly along the year. As shown by Figure 5.4, during the summer the full operation thermal losses are remarkably higher than the night thermal losses.

The Hot Tank is responsible for about 13% (86.8 MWh_t) of the overall thermal losses and the Cold Tank for about 9.4% (60.83 MWh_t). Finally, the remaining 16.6% of the yearly CSP thermal losses is due to the ORC start-up procedures.

Figure 5.5 shows the monthly distribution of the start-up losses. The maximum value of the ORC start-up losses can be found during summer months, when solar radiation is high and the ORC is able to be started every day. On the contrary, during winter months, the ORC start-up procedure is less frequent and therefore the start-up losses are reduced.

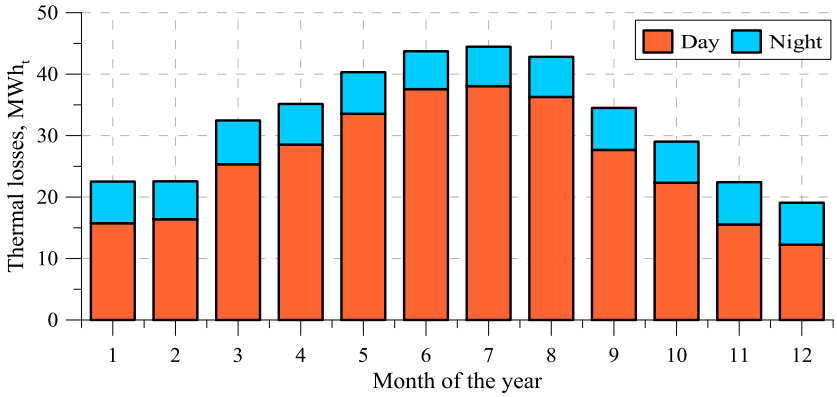

Figure 5.4. Monthly values of Solar Field thermal losses.

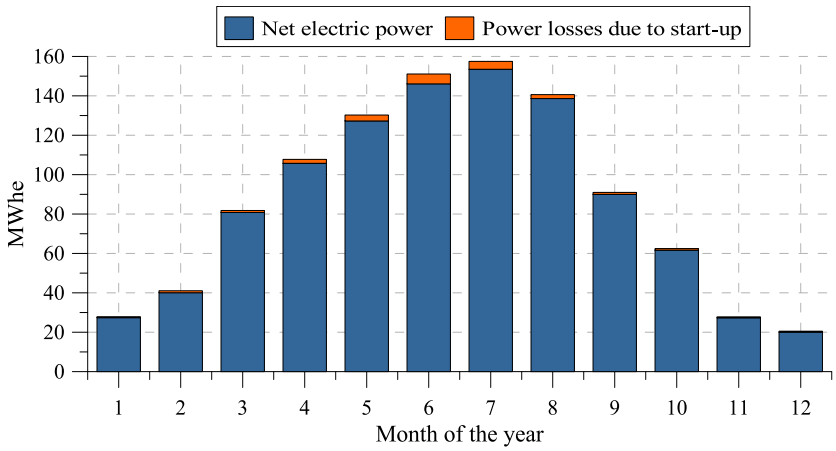

Figure 5.5. Monthly values of start-up power losses.

As also shown by Table 5.1, the electrical consumption of the plant auxiliaries requires about 11.8% of the ORC gross energy production and

Figure 5.6 presents their distribution along the year. The most important electrical consumption is given by the dry cooling section that highly increases during summer, when the ambient temperature is high and the ORC operates with lower efficiencies.

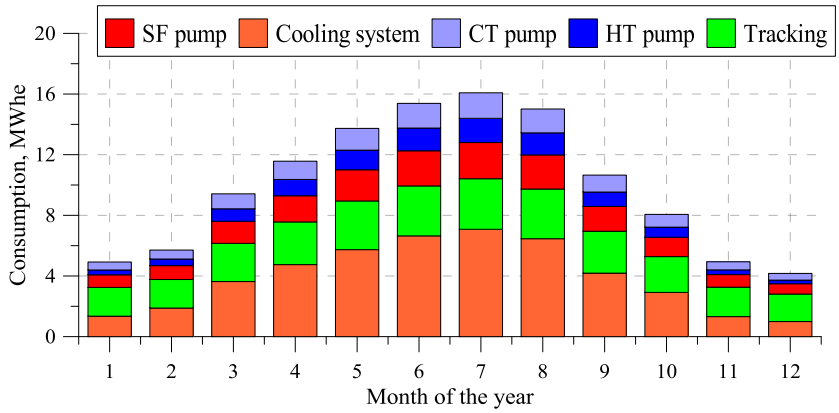

Figure 5.6. Incidence of auxiliaries' consumption.

The specific energy production of the CSP plant, which is herein and generally defined as the electrical energy production per unit area of collecting surface, strongly varies across the year. The distribution of the specific monthly energy production for the real case (with thermal losses inclusion) is reported in Figure 5.7, together with the corresponding values of available solar energy and ORC thermal input. As shown by Figure 5.7, the minimum monthly production is found in January and December, with average values of about 3 kWh/m^2 month. On the contrary, the maximum value is over 16 kWh/m^2 month and is reached in July.

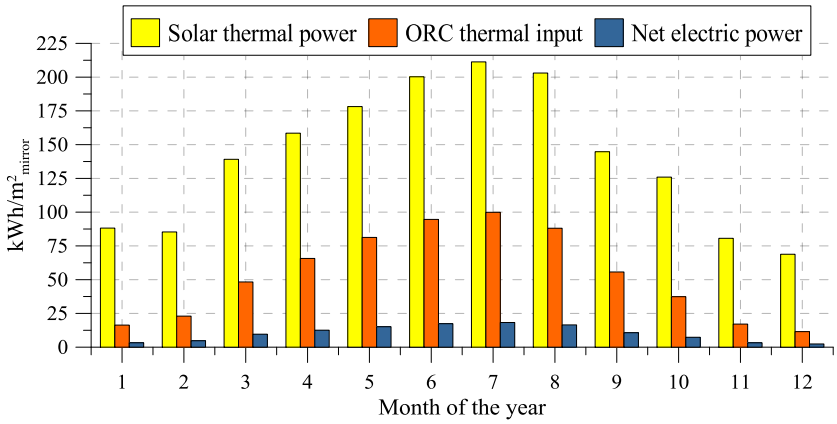

Figure 5.7. Monthly values of the CSP specific production per mirror area.

In order to provide a general outline of a possible daily operation of the CSP plant, Figure 5.8, Figure 5.9 and Figure 5.10 report the main representative performance parameters with reference of a three day period during summer, autumn and winter, respectively. In particular, each figure shows the thermal power output of the Solar Field, the ORC thermal power input, the CSP net power production, the SOC of the TES section and the oil temperatures inside the hot and cold pipes, as well as the average oil temperature inside the receiver tube of the Solar Field.

During summer (Figure 5.8), the DNI assumes its maximum values and therefore the ORC module can be started every day for several hours. Moreover, the power output of the SF exceeds the nominal thermal power input of the ORC module so that the Hot Tank can be charged with the exceeding thermal power, with the need of defocus some of the mirrors during the second day because the TES was full (SOC 100%). With reference to the temperature diagram, Figure 5.8 shows that the average oil temperature into the receivers slowly deeps to the ambient temperature during the night.

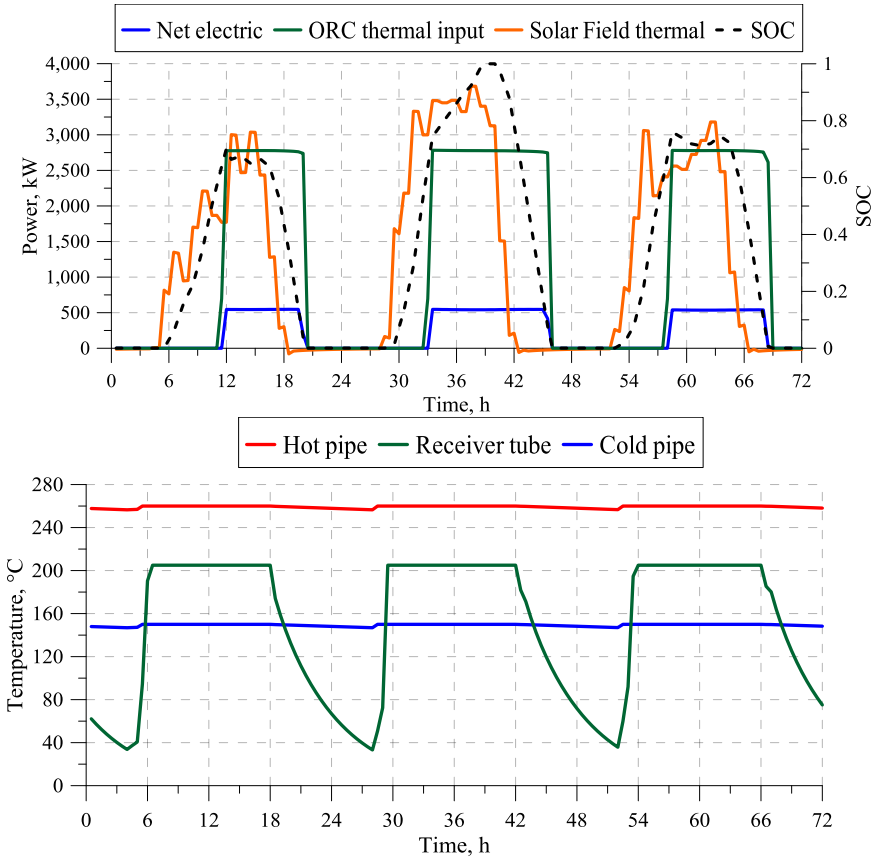

Figure 5.8. Power flows, SOC and Solar Field temperatures throughout three summer days.

During the typical autumnal three-day time period of Figure 5.9, a cloudy day is interposed between two sunny days. For this reason, the ORC is started for some hours only during the first and third days. In fact, at the beginning of the second day the thermal storage is empty and the solar radiation is not enough to warm up the oil up to the nominal temperature. The SF receiver temperature reaches about 80°C during sunlight and then it drops again to the ambient temperature due to the absence of solar radiation.

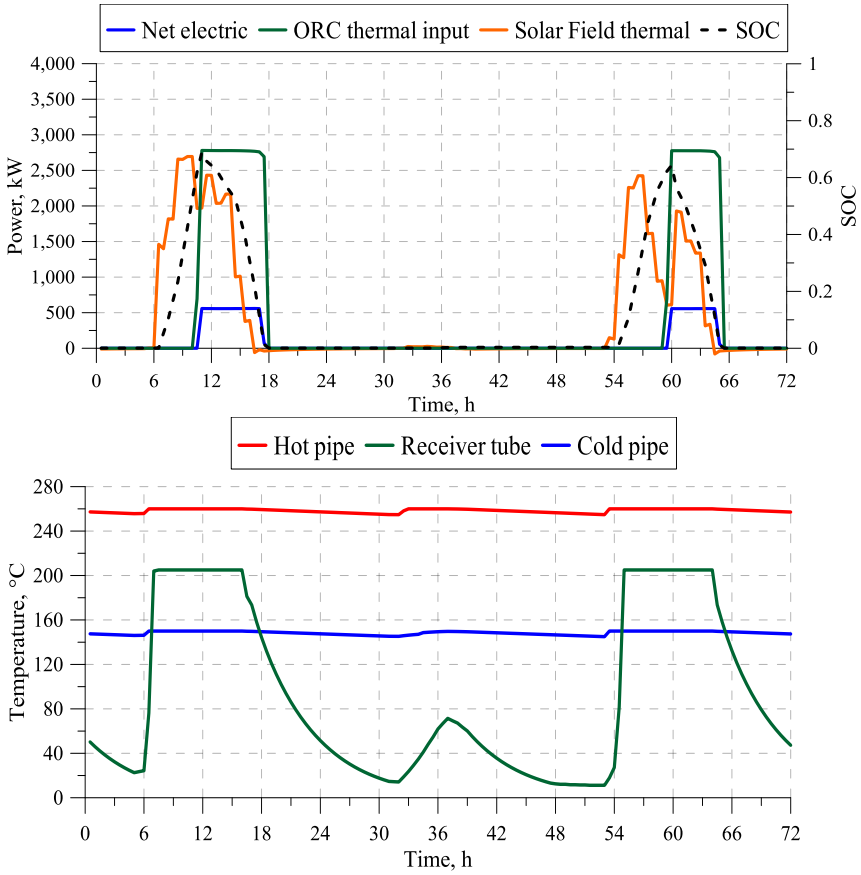

Figure 5.9. Power flows, SOC and Solar Field temperatures throughout three autumnal days.

During the typical winter three-day time period, the thermal power produced by the SF never reaches the summer values. As shown by Figure 5.10, during the first day the Hot Tank is charged but the ORC unit cannot be started yet, because of the limit of three-hours of minimum up-time. The storage charge level is kept almost constant during the night and it raises 70% of its maximum value during the first hours of the second day. During the second day the ORC module can be started, as shown by the corresponding power output. The third day is rainy or cloudy, so the thermal power produced by the SF is negligible, the Hot Tank is empty and the ORC cannot be switched on.

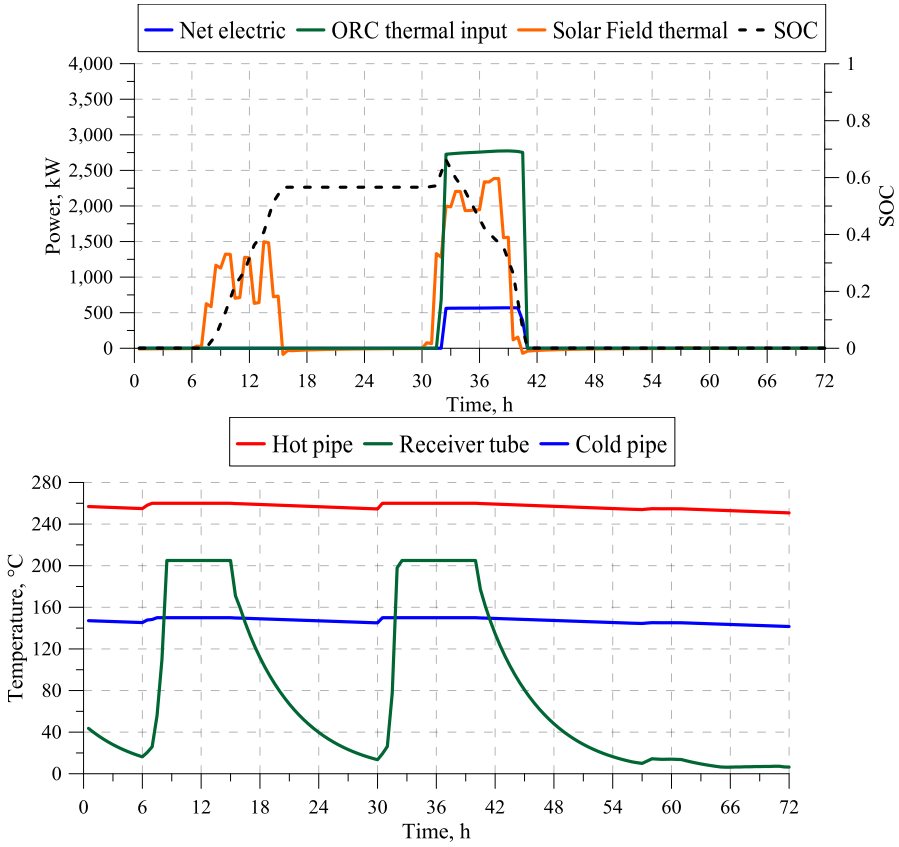

Figure 5.10. Power flows, SOC and Solar Field temperatures throughout three winter days.

Overall, the results of the performance assessment reported in the present paragraph demonstrate that the overall yearly thermal losses of the CSP plant are about 4.4% of the available solar energy or 10.9% of the thermal power concentrated onto the receiver tube. The sum of all these thermal losses determines a corresponding reduction in the net energy production by about 9% on yearly basis. Almost 61% of the thermal losses are located in the Solar Field (receiver tubes and hot and cold oil pipes), 22.3% in the hot and cold oil tanks and the remaining 16.6% is represented by the thermal energy required by the ORC start-up phases.

The most important thermal loss of the Solar Field can be found in the receiver tubes, both during operation and night periods. In particular, the night thermal losses account for about 20.5% of the overall SF thermal

losses. Overall, due to the presence of the thermal losses, the average efficiency of the Solar Field decreases from 40.3% to 37.6% and the thermal energy supplied to the ORC unit decreases by about 11%. On yearly basis, the thermal losses of the TES section are about 2.6% of the thermal energy produced by the SF, with a corresponding TES average efficiency of about 97.4%. About 60% of the TES thermal losses relates to the hot oil tank and the remaining 40% to the Cold Tank. Finally, the hot and cold start-up procedures of the ORC unit account for about 16.6% of the yearly thermal losses. The maximum value of the ORC start-up losses can be found during summer months, when solar radiation is high and the ORC is able to start every day.

5.1.2. Thermal energy losses during night, warm-up and full-operation periods of a LFR solar field

After assessing the yearly thermal losses of the overall small-size CSP plant, the author work was focused on the thermal losses evaluation of a 8,400 m^2 LFR-based Solar Field under different operating conditions and for a time window of a few hours.The considered Solar Field is composed of 6 loops of 220 m each.

The main objectives of the work [55] reported in the present paragraph were to assess both the evolution of the temperature distribution along each loop of the Solar Field and the time durations necessary to reach different temperature conditions of the line.

Basically, three different operating conditions have been herein analyzed: night, warm-up and full-operation. In order to better explain how these conditions have been simulated, the considered layout of the Solar Field is reported Figure 5.11 and the relative component status are listed in Table 5.2.

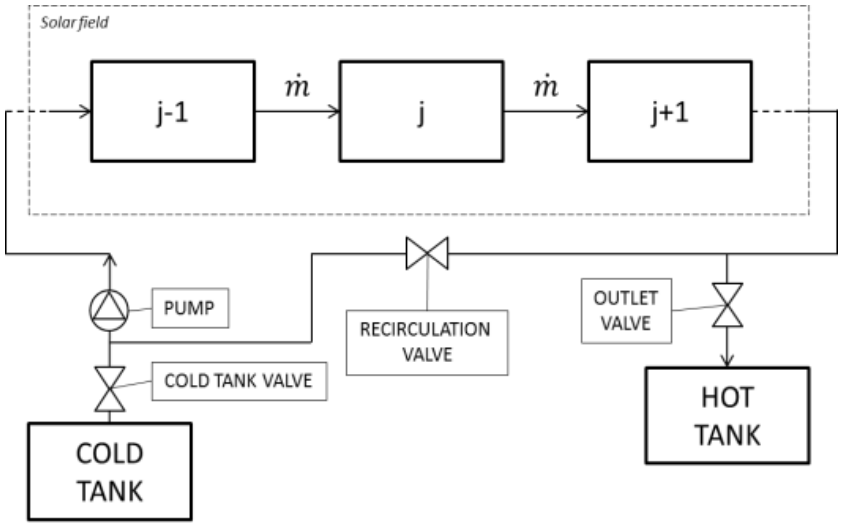

Figure 5.11. Solar Field layout.

Table 5.2. Table of components' status during night, warm-up and full operation.

Operation mode	Pump	Cold Tank valve	Recirculation valve	Outlet valve
Night	OFF	closed	closed	closed
Warm-up	ON	closed	open	closed
Full operation	ON	open	closed	open

The mode defined as *night* becomes operative when the solar radiation is missing and the oil contained in the receiver tubes and in the piping is still at high temperature (this happens at the end of a good-weather day).

The initial temperature profile of the Solar Field loop during night, equal to the last temperature profile achieved during operating hours, gradually cools down to the environment temperature due to radiative losses. The oil temperature of the SF is influenced also by convective and conductive thermal exchanges within the oil.

When simulating the night mode, the pump represented in Figure 5.11 is switched off and all the valves are closed in order to avoid useless energy consumptions and to avoid forced convection inside the Solar Field. Considering as initial condition the last temperature profile reached in nominal conditions, for an ambient temperature of 20 °C the entire cooling process to reach the environment temperature lasts less than 4 hours.

Figure 5.12 shows the average heat loss of the receiver and of the piping across time. The total energy loss due to night cooling is 505.6 MJ related to receiver plus 13.1 MJ related to piping.

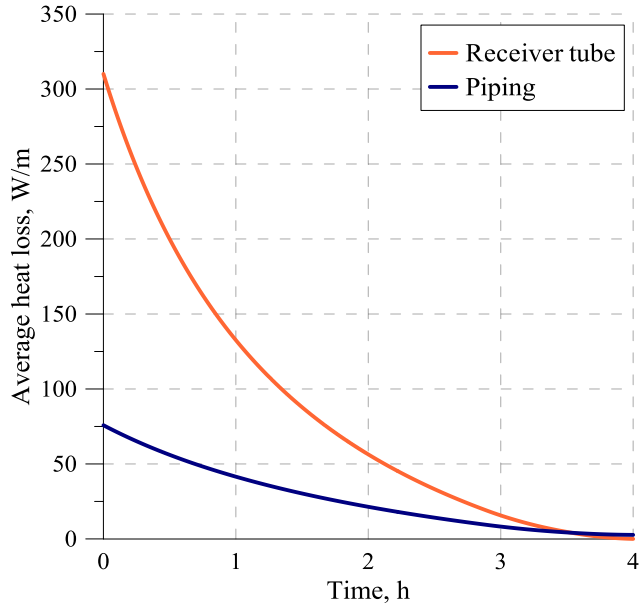

Figure 5.12. Average heat loss during cooling (night mode).

The temperature distribution along the Solar Field loop during the cooling process is shown in Figure 5.13. The initial condition (t=0) is the last temperature profile reached at nominal conditions, and then the temperature gradually drops along the loop.

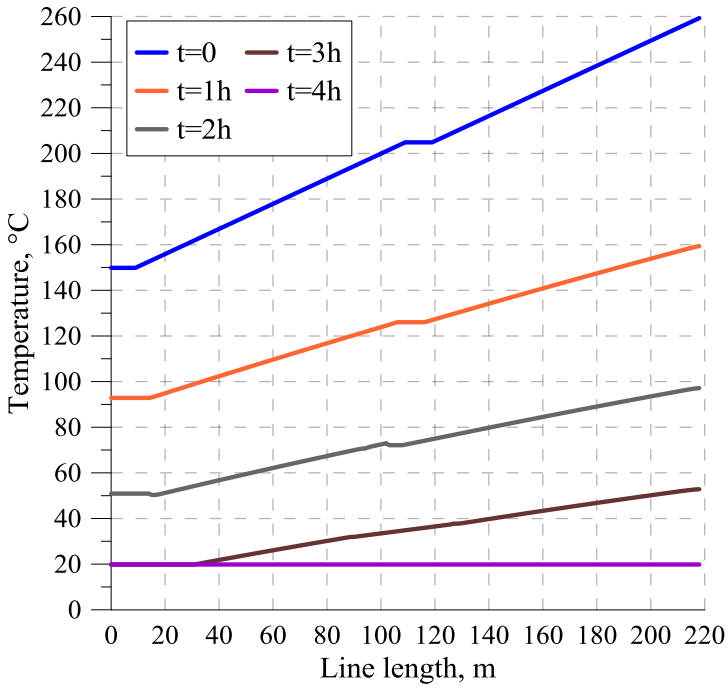

Figure 5.13. Temperature distribution along the SF line during cooling (warm up mode).

The mode defined as *warm-up* is used when the Solar Field has to be warmed up to the nominal conditions of temperature. This mode not only includes the sunrise warm-up, but also the warm-ups that occur during-the-day, which are needed after clouds of long duration. In this operation mode, the main pump is turned on and the HTF mass flow recirculates through the SF loops until it reaches the nominal/desired temperature (Cold Tank valve and outlet valve are closed). Once this condition is fulfilled, the Cold Tank valve and the outlet valve can be opened. Once the SF design temperature is reached, the full operation mode can be started. The thermal oil is extracted from the Cold Tank, it passes through the SF and then it is sent to the Hot Tank.

Figure 5.14 shows the time necessary to reach the Solar Field inlet design temperature of 150 °C starting from an oil temperature equal to an average ambient temperature of 20 °C for two different days of the year (representative of a spring and a winter day) characterized by the different

DNI curves displayed in Figure 5.15 and a recirculation mass flow assumed to be the 70% of the nominal mass flow.

During a typical spring day a value of DNI of 700 W/m^2 is reached after 2 hours from sunrise, and after only one hour the DNI value is already above 400 W/m^2. In this case, the outlet temperature rapidly rises and after approximately 45 minutes it reaches the nominal temperature.

During the typical winter day analysed, even after 2 hours the DNI value is under 200 W/m^2 and therefore the outlet design temperature is reached after about 2 hours and a half. Once the design temperature is reached, the recirculating pumps are turned off and the full operation mode can begin.

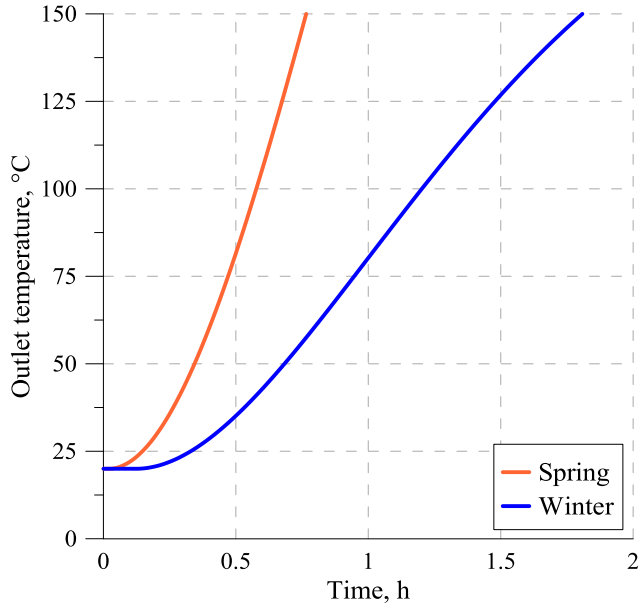

Figure 5.14. Time necessary to reach the nominal temperature (warm up mode).

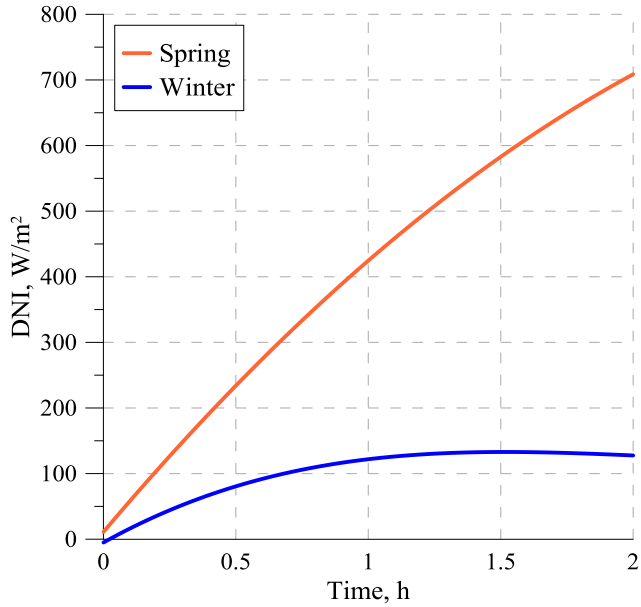

Figure 5.15. DNI curves during spring and summer.

In the *full operation* mode, the control system purpose is to achieve always the nominal output temperature. In order to do so, the SF inlet valve regulates the HTF mass flow that enters and circulates through the lines depending on the output temperature and the available DNI, assuming and inlet temperature constantly equal to the design temperature of 150 °C.

In Figure 5.16 is shown the output temperature behaviours depending on the mass flow for different values of DNI and a constant inlet temperature of 150 °C. The output temperature displayed is the one reached after the travel time related to the mass flow considered. For the lower values of DNI, the curves' slope is flat. This means that when the solar radiation is below 150-200 W/m^2, the SF outlet temperature dependence on the mass flow rate is almost negligible. For example, considering a DNI of 100 W/m^2, the SF outlet temperature is little above 170 °C for a mass flow of 0.5 kg/s and still above 160 °C for a mass flow of 2 kg/s. On the contrary, for the higher values of solar radiation, the mass flow strongly influences the SF outlet temperature. For instance, considering a DNI of 800 W/m^2, the SF outlet temperature is above 320 °C for a mass flow of 0.75 kg/s and 230 °C for a mass flow of 2 kg/s. Still

referring to this graph, the operating field to prevent thermal oil to deteriorate can be seen: in fact, commercial thermal oils have a temperature upper limit in the range of 260-390°C.

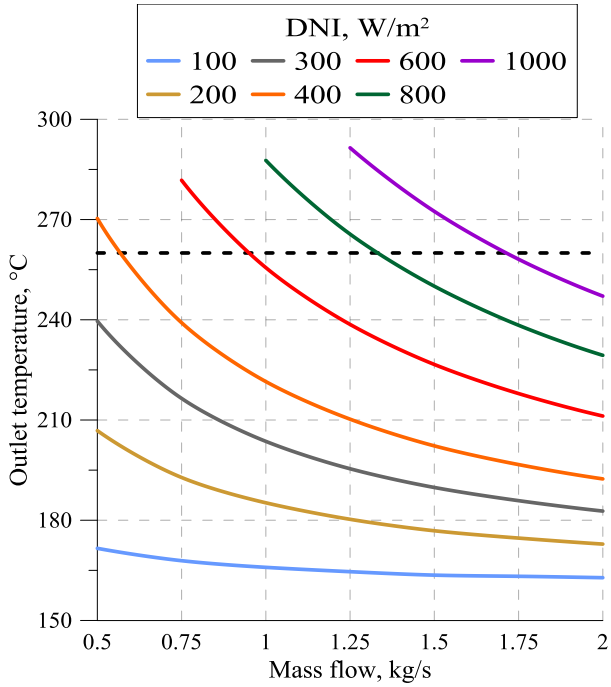

Figure 5.16. Outlet temperature depending on the mass flow and DNI (full operation mode)

Considering that the design outlet temperature of the SF, when coupled with medium-size ORC system is in the range of 260-280 °C, Figure 5.16 allows to obtain the required mass flow as a function of the available solar radiation and the design outlet temperature.

Since Solar Thermal Power Plants' source of energy is the sun, and the Direct Normal Irradiance strongly varies depending on clouds, it is very important to analyze what happens to the SF temperature during cloud transients.

Figure 5.17 shows the Solar Field outlet temperature depending on cloud duration for different values of mass flow (during the cloud duration

the incoming DNI is assumed null). It is interesting to notice that higher mass flow rates cause lower outlet temperatures. The temperature trend can be considered as linear and so it can be defined a rate of temperature decrease in function of cloud duration (time) and mass flow. For a mass flow of 2.0 kg/s, the temperature decreases by about 60 °C during a three-minute-long cloud duration so the temperature decrease rate is about 20 °C/min. For a slower mass flow of 0.5 kg/s, even the temperature decrease rate is slower, and it is about 7 °C/min. Responses to different type of clouds are examined in depth in paragraph 5.1.3.

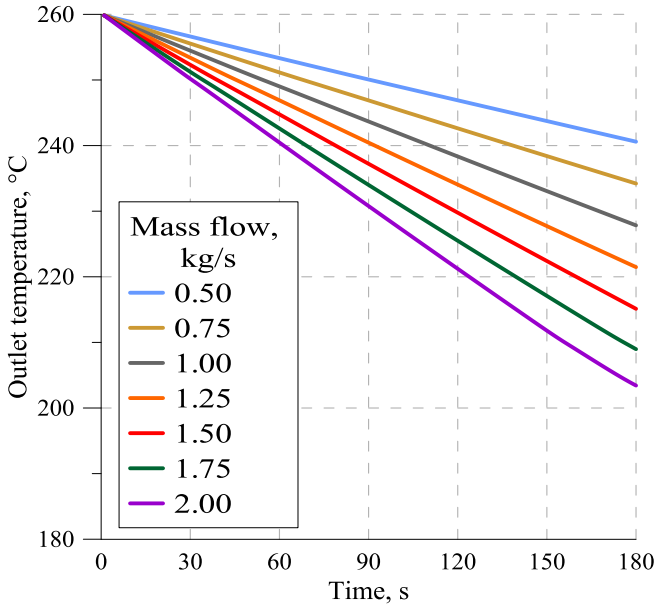

Figure 5.17. Solar Field outlet temperature depending on cloud duration.

The results obtained demonstrate that thermal energy losses during an average night are in the range of 140 kWht, 97.5% of which are due to receivers and 2.5% are due to piping. After 3 hours the maximum oil temperature is below 50 °C and after 4 hours its temperature is uniform and equal to the ambient temperature. The warm up phase of the Solar Field can last from 45 minutes up to 2 hours, depending on DNI. During

full operation, the cloud influence on the oil temperature drop is strongly determined by its mass flow, and usual values range from 7 to 20 °C/min.

5.1.3. Thermo-fluid dynamic analysis of a LFR Solar Field during transient operation

After the assessment of the main thermal energy losses of both the entire CSP Plant and the Solar Field, obtained through the simplified 1D numerical model discussed in the previous paragraphs, the author's research has progressed by improving the 1D model complexity, reducing the simulation time step, and by simultaneously developing an axisymmetric unsteady 2D numerical model under Comsol® environment. The research work that is reported in the present paragraph, which also includes a comparison between the two developed model results, can be found in its original published version in [59].

The comparison between the two developed models has been carried out with reference to three different operating conditions of the Solar Field, described in the following and displayed in Figure 5.18:

- the warm-up phase, obtained simplifying the increasing power coming from the sun after sunshine with ramps of different duration;
- the full operation transients, applying different steps and pulses of the sun power;
- the shut-down phase, modeled through a ramp with a negative slope.

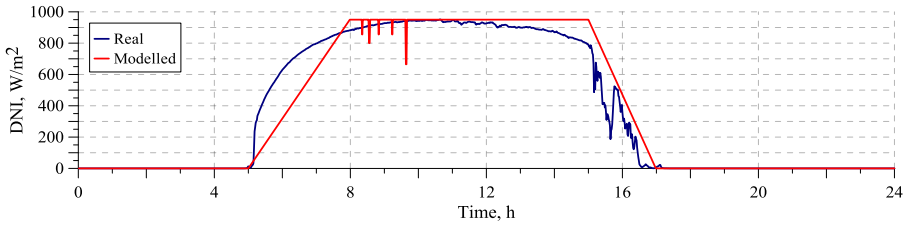

Figure 5.18. Real and modelled trend of DNI.

The results are displayed with reference to a single loop of the Solar Field. Temperature evolution is shown with reference to the final section of the line, at the outlet of the loop, and with reference to the entire length of the line.

Warm-up phase

This is the phase that occurs immediately after sunshine, and it has been modeled through different ramps of power coming from the sun (Q_{sun}). Two, three and four-hour long Q_{sun} ramps have been considered, starting from zero and up to the design power ($Q_{sun,\ design} \approx 720$ kW), obtained with a DNI value of 900 W/m^2, an air temperature of 17 °C, an elevation of 73° and an azimuth of 0° for each of the six loops composing the Solar Field.

The HTF flows from the Cold Tank (T=150°C), with a constant mass flow of 0.5 kg/s (about 17% of the nominal mass flow value) and no recirculation through the SF, has been considered. The HTF, piping and receiver tubes temperatures were initially set equal to the environment temperature (17°C).

Figure 5.19 shows the fluid temperature at the SF outlet over the time, for the three cases of 2, 3 and 4-hour-long ramps of Q_{sun}. For each case, the evolution of the temperature at the outlet of the SF over the time can be virtually subdivided in three parts. The first part (with the lowest slope rate) shows the little increase of the temperature at the outlet of the SF mainly caused by the temperature difference between fluid and receiver tube, which is heated by the available sun radiation. In fact, during the first 10-15 minutes, the contribution of the mass transport term of the energy balance equation significantly affects only the sections immediately downstream of the duct inlet, due to the great distance between the inlet and outlet sections of the receiver tube. During the second very sloped part of each curve, the influence of the mass transport term at the outlet section of the SF is stronger. Finally, during the third and last part of the warm-up curve, the temperature trend slope is again reduced, for the smaller temperature gradient between adjacent sections. Different durations are required for the entire warm-up process up to 260°C, in accordance with the DNI ramps: with a ramp of two hours, the

outlet design temperature is reached approximately after 40 minutes, with a three-hour long ramp more than 50 minutes are required and with a four-hour long ramp the warm-up process takes more than one hour.

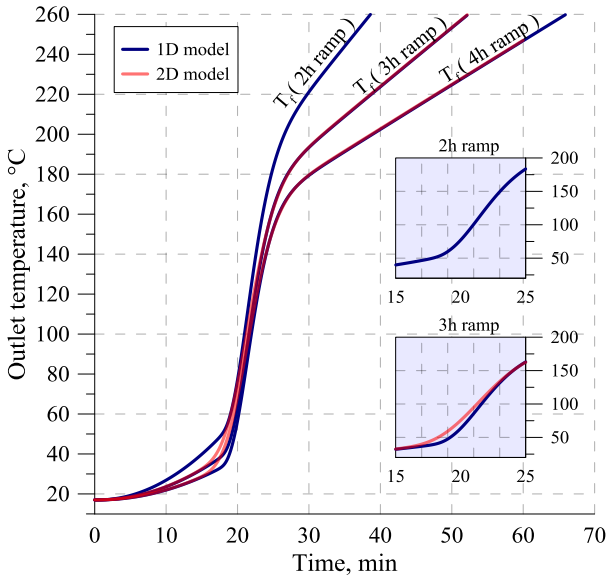

Figure 5.19. Outlet temperature of the SF for the case of 2-hour long ramp.

Figure 5.20 shows the progressive evolution of the temperature distribution along the SF line, for the case of the 2-hour long ramp. Comparison of the right sections of the 5 minutes and 10 minutes curves highlights the negligible contribution of the mass transport term of the energy balance equation at the farthest segments of the duct. It is interesting to notice that, even after the second inflection point of Figure 5.19, the temperature distribution shown in Figure 5.20 is not linear during transients, but it becomes linear only at equilibrium.

The comparison between the results of the two simulation models gives very close curves, with little differences only around the first inflection point of Figure 5.19 (as highlighted in the sub-graphs) and around the second inflection point of Figure 5.20

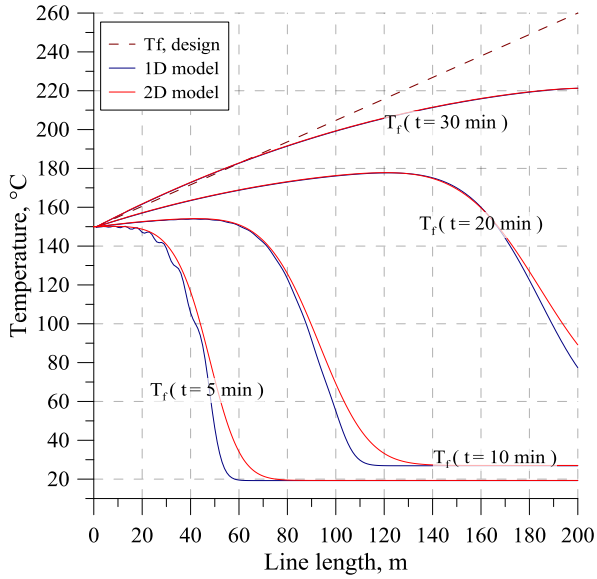

Figure 5.20. Temperature distribution along the SF line for the case of 2-hour long ramp.

Full-operation transients

As previously stated, since Concentrating Solar Technologies use only the direct component of the global irradiance (DNI), during the Solar Field operating phase the clouds' passage over the mirrors causes frequent variations of the receiver tube available power. These variations can be sudden or gradual and brief or long-lasting: in fact the DNI can widely vary its value even down to zero in few seconds. For this reason, the two models' responses to Q_{sun} steps and rectangular pulses of different amplitude and duration are shown and described in the present paragraph.

Figure 5.21 shows the system responses when a Q_{sun} step occurs: the Q_{sun} amplitude suddenly decreases by 25%, 50%, 75% and 100%, starting

from the nominal conditions. As it can be seen, the two developed models lead to very similar results. Each step in Q_{sun} determines a new equilibrium condition of the system after approximately 6 minutes of the step occurrence, and the final (f) equilibrium temperature depends on the final Q_{sun} amplitude. For a final Q_{sun} amplitude of 25%, the outlet final temperature is about 175°C, while for a final Q_{sun} amplitude of 50% the value is slightly above 200°C and for a final Q_{sun} of 75% the HTF temperature is around 225°C. If the final Q_{sun} is zero, as shown, the HTF thermal exchanges are only represented by heat losses, so the final equilibrium temperature is a little below the inlet temperature of 150°C.

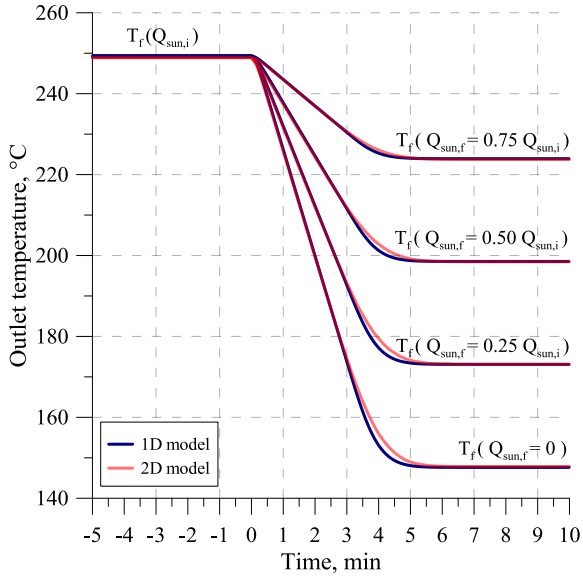

Figure 5.21. Fluid temperature at the outlet of the SF for the case of final DNI=50%.

The temperature distribution along the line and its evolution over time can be seen in Figure 5.22. T_f (t=0) shows the initial equilibrium condition: the temperature distribution along the line can be represented by a straight line. One minute after the step occurrence the slope is reduced and an inflection point occurs. The inflection point moves along

the line until a new equilibrium condition is reached and the temperature distribution returns to be linear.

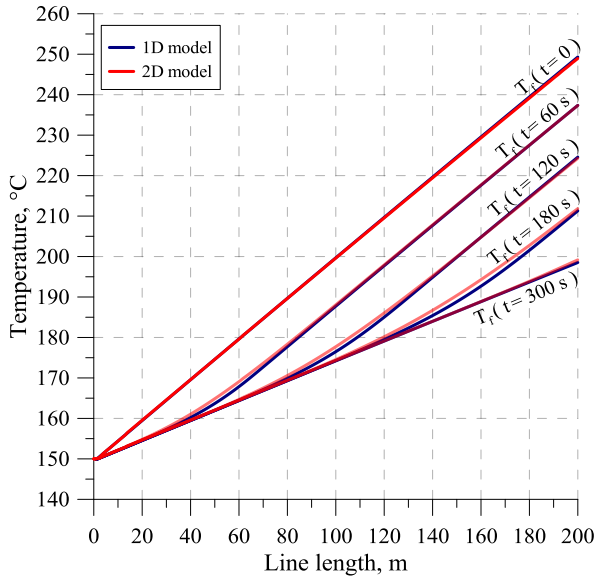

Figure 5.22. Temperature distribution along the SF line for the case of final DNI=50%.

During real operating conditions of a Solar Field, Q_{sun} variations in the range of 10-30% are very frequent and they have been modeled through rectangular pulses. Figure 5.23(a-f) show the system responses to Q_{sun} pulses of different amplitude and durations, with reference to the nominal mass flow rate. This operating condition has been considered in order to determine a threshold level for the regulation action of the circulating pumps: in fact, if the Q_{sun} variation causes negligible variations of the outlet temperature, the oil mass flow can (ideally) be maintained almost constant. The subscript (i) defines the initial condition, and (f) the final.

Figure 5.23 (a), (b), (c) show system responses to pulses starting at t=0 and having the same duration (t=60s) but different amplitudes ($Q_{sun,f} = 0.9\ Q_{sun,i}$, $Q_{sun,f} = 0.8\ Q_{sun,i}$, $Q_{sun,f} = 0.7\ Q_{sun,i}$).

Figure 5.23 (d), (e), (f) show responses to pulses starting at t=0 and having a longer duration (t=90s) and amplitudes of $Q_{sun,f} = 0.9\ Q_{sun,i}$, $Q_{sun,f} = 0.8\ Q_{sun,i}$, $Q_{sun,f} = 0.7\ Q_{sun,i}$, correspondingly.

Results of Figure 5.23 demonstrate that the temperature drop increases with the increase of both amplitude and duration of the pulse. A 10% decrease of the solar power input lasting up to 90s (Figure 5.23 (a) and (d)), causes temperature drops in the range of 5°C. In the case of a deeper Q_{sun} decrease (20%), Figure 5.23 (b) and (e) show that the temperature fall can be almost doubled (10°C), in the case of 90s pulse, with respect to the aforementioned cases.

The case of a 30% Q_{sun} reduction is reported in Figure 5.23 (b) and (e) and gives a maximum temperature drop of about 15°C. Figure 5.23 also demonstrates that the results obtained through the 1D and 2D models are very close and similar, especially during the temperature decreasing phase.

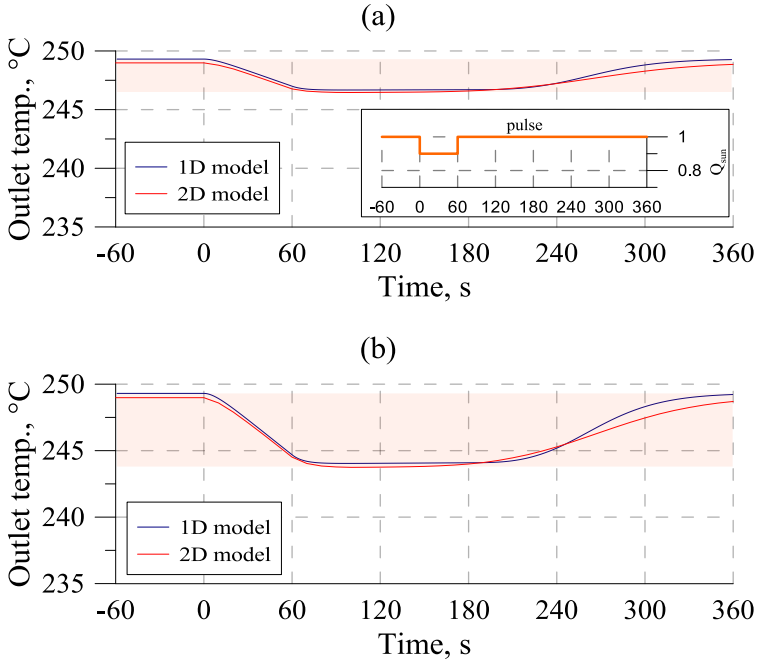

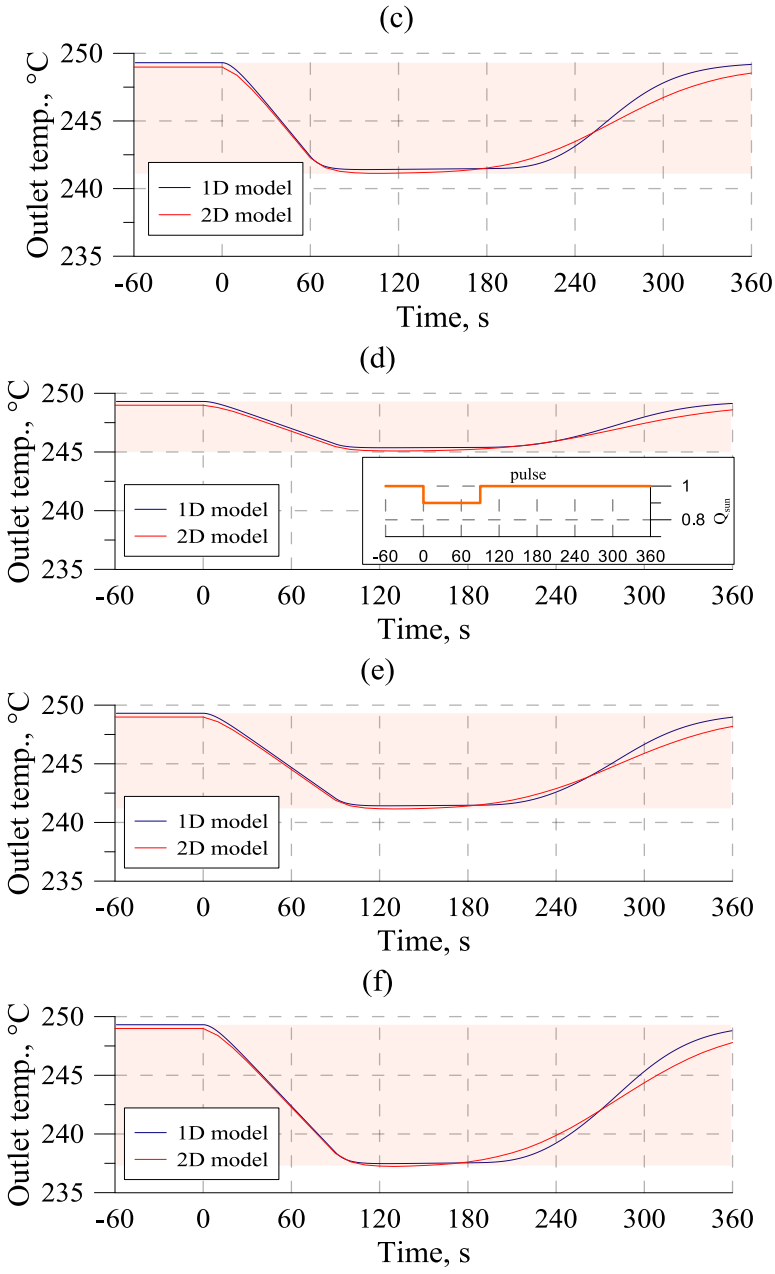

Figure 5.23. Outlet temperature of the SF: system responses to pulses. (a) $Q_{sun,f}$ = 0.9 $Q_{sun,i}$, t=60s; (b) $Q_{sun,f}$ = 0.8 $Q_{sun,i}$, t=60s; (c) $Q_{sun,f}$ = 0.7 $Q_{sun,i}$, t=60s; (d) $Q_{sun,f}$ = 0.9 $Q_{sun,i}$, t=90s; (e) $Q_{sun,f}$ = 0.8 $Q_{sun,i}$, t=90s; (f) $Q_{sun,f}$ = 0.7 $Q_{sun,i}$, t=90s.

Shut-down phase

The shut-down phase is the operating condition of the Solar Field during the final daily time, which occurs before sunset and has been modeled trough a Q_{sun} negative ramp, which starts from $Q_{sun,\ design}$ down to zero in 2 hours, at the nominal mass flow rate. Figure 5.24 shows the Solar Field outlet temperature over time. The outlet temperature linearly decreases and with the considered input power Q_{sun}, the minimal temperature of 150°C is reached after two hours.

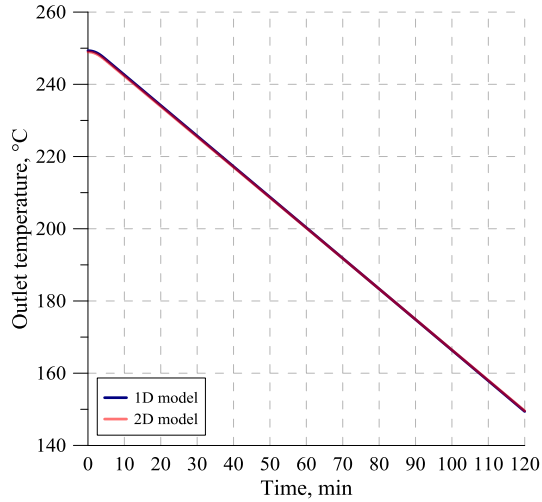

Figure 5.24. Outlet temperature of the SF for the shut-down phase

The temperature along the Solar Field line for the shut-down phase, shown in Figure 5.25, linearly decreases and the temperature distribution reduces its slope down to the ambient temperature. Nevertheless, during a real operation of the shut-down phase, the line mass flow is reduced in order to keep the Solar Field outlet temperature as high as possible when the DNI values decrease.

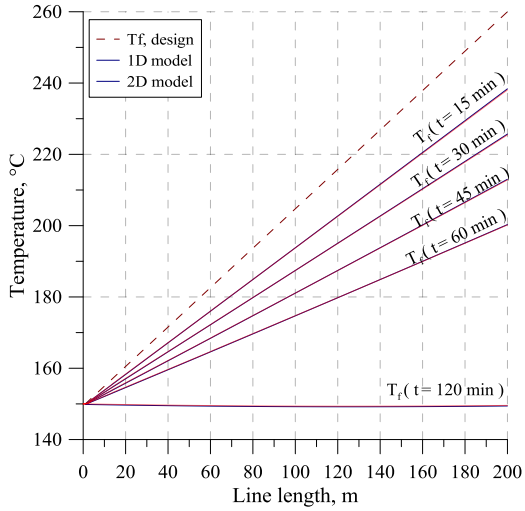

Figure 5.25. Temperature distribution along the SF line for the shut-down phase.

The research results reported in the present paragraph investigated the dynamic responses of a Solar Field line of a medium-size CSP Plant. Furthermore, a comparison between a non-stationary one-dimensional model and a non-stationary two dimensional model has been carried out. Three operating phases of the Solar Field line have been studied: warm-up, full operation transients and shut-down phases. Depending on the time evolution of the solar power, the warm-up process up to nominal conditions can last up to more than 1 hour, and the temperature distribution along the line evolves with some inflection points that gradually disappear. The full operation transients have been modeled through steps and pulses of different amplitude and duration. The most important conclusion of this phase analysis is that a time period of about 5-6 minutes after the step/pulse occurrence is necessary to restore new equilibrium conditions. The shut-down phase analysis allows knowing the system response to a decreasing ramp of incoming solar power. The two models lead to very similar dynamic responses for all three operating phases. For this reason, the simplified one-dimensional model can be confidently used for control and management purposes.

Since the effectiveness of the simplified one-dimensional model has been assessed by the present study, this simulation model can be reliably used to evaluate and compare different energy management strategies of the CSP system.

5.1.4. Recirculation strategies of a line-focus Solar Field

The present paragraph represents the results of a study on a line-focus Solar Field based on Linear Fresnel Reflectors, carried out with the purpose to evaluate the recirculation influence on the performance of a small-size CSP system.

The analysis is based on the different recirculation strategies (B, C, D) proposed and described in Paragraph 4.1.1.5 and herein compared with the case of absence of recirculation (A), during the various operating phases of a CSP that occur throughout a day.

Results are shown with reference to a data set of three typical days (good, variable and bad-weather day) shown in Figure 5.26. DNI evolution, solar elevation, azimuth, air temperature and wind speed of the site of Ottana are used as input data with a resolution of one minute. As shown in Figure 5.26, the DNI for the good day does not present strong variations, while the trends reported for the variable-weather and especially for the bad-weather day are representative of typical cloudy days, with high and sudden variations.

The technical data and parameters of the Ottana CSP system have been assumed for the simulation, together with the following assumptions. A minimum SF mass flow rate of 3.0 kg/s (equally subdivided among the 6 lines) has been determined by the operating range of the pumps, while no mass flow rate is allowed for solar elevation values lower than 10°. In addition, a minimum up time for the Power Block has been set equal to 3 hours, corresponding to a SOC level of 60%. The stored energy is preferably used to produce electricity during evenings or nights, when other solar technologies without storage are in stand-by, and therefore the SOC values at sunrise are generally low: for this reason an initial SOC of 10% is assumed for every simulation.

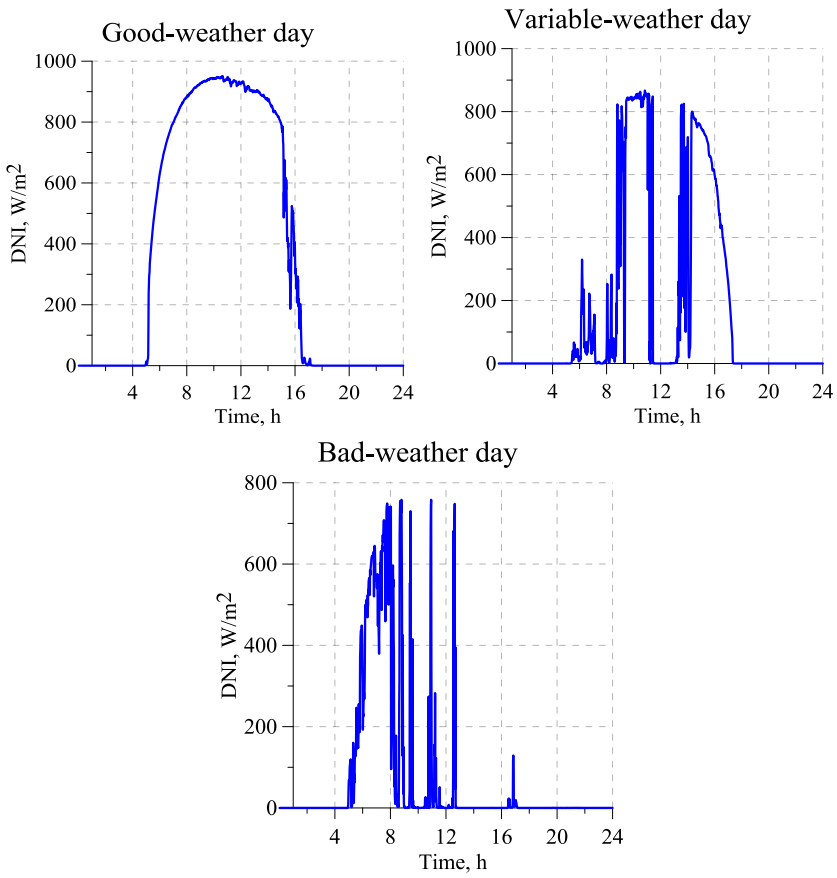

Figure 5.26. DNI evolution during the days analysed (recirculation strategies).

Good-weather day

In Figure 5.27 are displayed the mass flows in the recirculation line and toward the Hot Tank, during the good-weather day and for the different recirculation strategies introduced. As it can be seen, differences among the mass flows for the different recirculation strategies are very little, and localized around the sunrise warm-up and the shut-down phases. During warm-up, a total recirculation occurs in all the cases, except the reference case A. During the central hours of the day, the good weather allows the system to totally deliver the mass flow to the Hot Tank during the full operation, independently of the adopted recirculation strategy. During shut-down phase, in the A and C cases the whole mass

flow is delivered to the Hot Tank, while in the other cases a recirculation occurs.

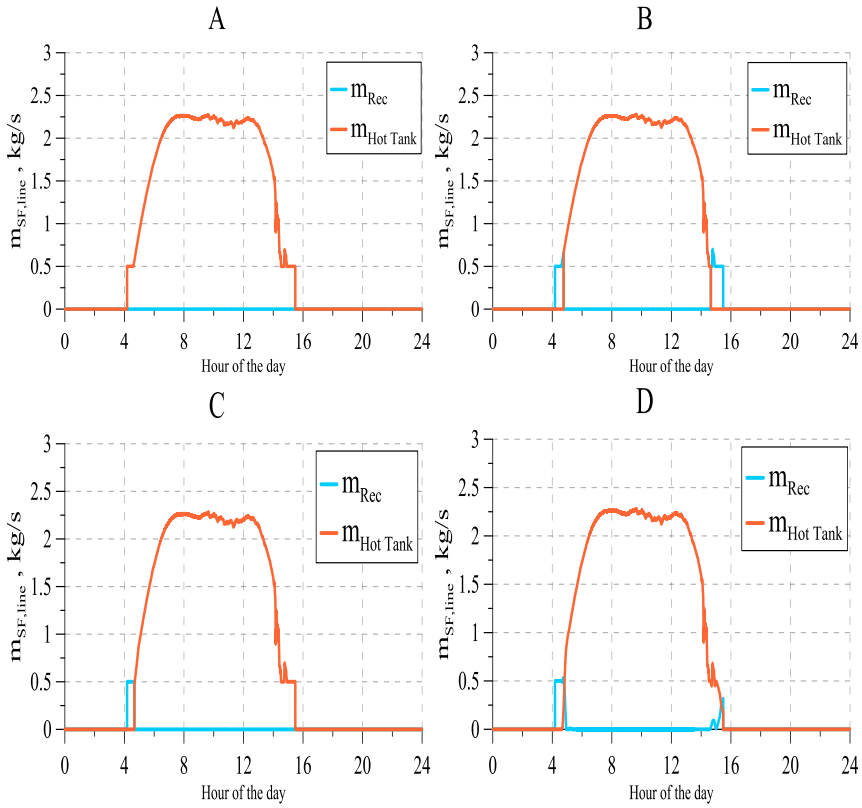

Figure 5.27. Recirculated and Hot Tank mass flows for the reference case (A) and the three recirculation strategies (B, C, D) of the good-weather day.

The comparison among Hot Tank and Cold Tank temperature evolutions for the different strategies can be seen in Figure 5.28. Hot Tank temperature distributions show no substantial differences among B, C and D cases, and a remarkable difference with respect to the A case. This happens because in the A case the HTF is delivered to the Hot Tank at the temperature of the initial pump start, without any pre-heating. Furthermore, the Hot Tank is almost empty at the beginning of the day, and therefore its thermal capacity is more influenced by a minimum mass of cold oil with respect of other times of the day. Cold Tank temperature distributions show the same trend until approximately 3 p.m. At that time,

the Cold Tank temperature of the B case rises of 2-3 °C because the system management started the SF recirculation passing the Cold Tank again: in fact, the SF outlet temperature is not high enough to be sent to the Hot Tank but it is higher than the Cold Tank temperature, causing an increase of the latter.

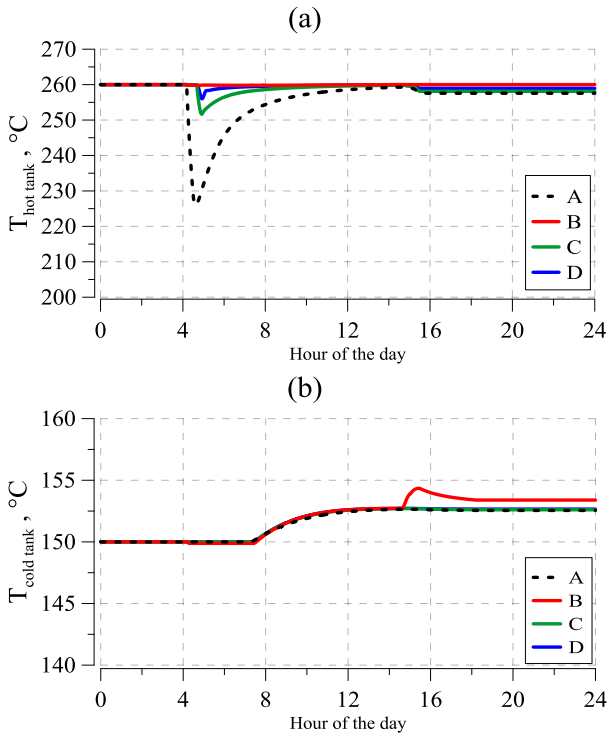

Figure 5.28. Hot and Cold Tank temperatures for the reference case (A) and the three recirculation strategies (B, C, D) of the good-weather day.

SOC and net power output for the different recirculation strategies are displayed in Figure 5.29: as it can be seen both SOC and net power output are negligibly influenced by the recirculation strategy adopted.

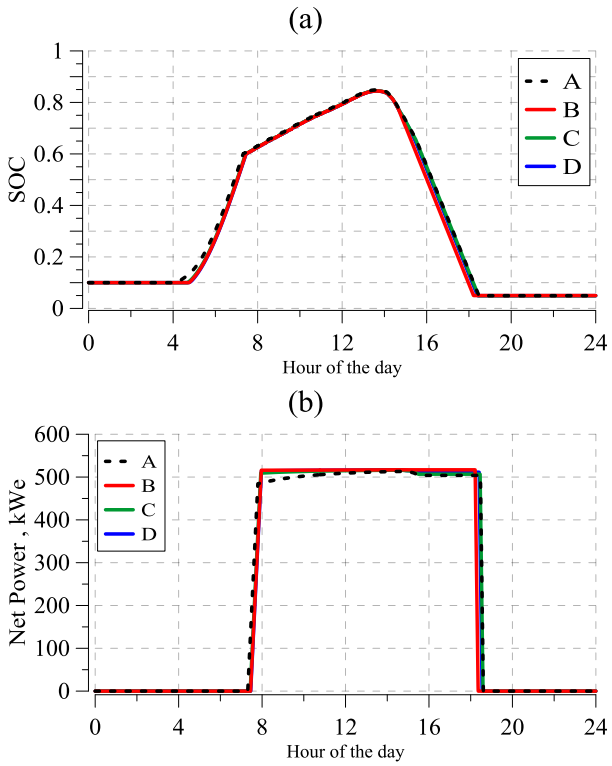

Figure 5.29. SOC and Net Power output for the reference case (A) and the three recirculation strategies (B, C, D) of the good-weather day.

Variable-weather day

Herein are reported the results for the variable-weather day, characterized by a partially-cloudy sky. In Figure 5.40, the mass flows in the recirculation line and in the Hot Tank line are displayed. As it can be seen, the differences among the mass flows for the different recirculation strategies are considerable throughout the entire day. In the reference case A no recirculation occurs and therefore the entire mass flow is always delivered to the Hot Tank. In the B, C and D strategies the recirculation occurs accordingly to the abovementioned assumptions.

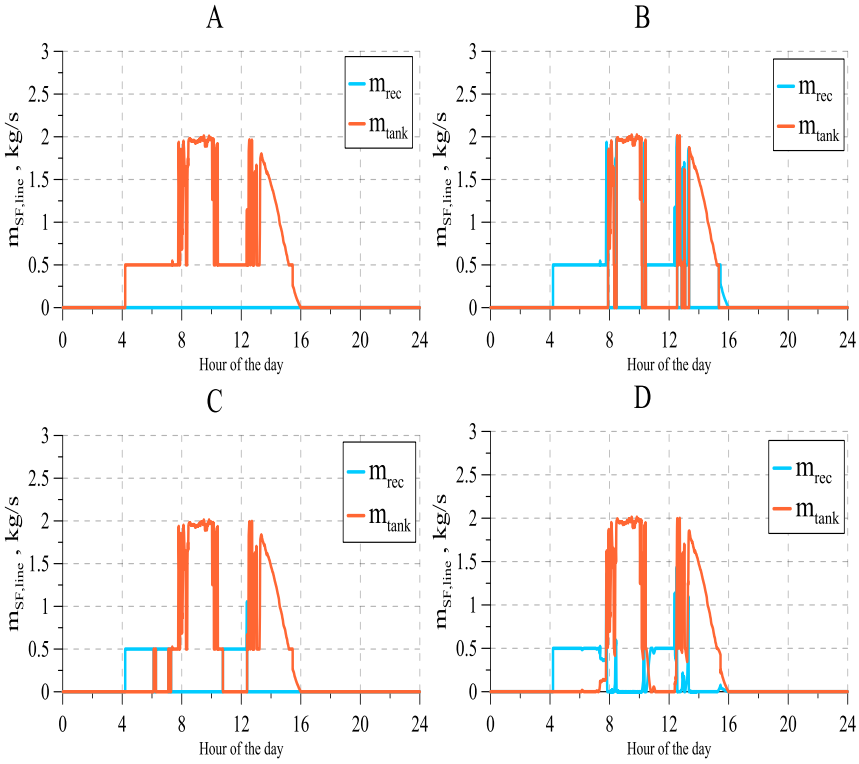

Figure 5.30. Recirculated and Hot Tank mass flows for the reference case (A) and the three recirculation strategies (B, C, D) of the variable-weather day .

For the variable-weather day, substantial differences exist also in the Hot and Cold Tank temperature trends. As displayed in Figure 5.31(a), the reference case A is characterized by a deep reduction of the Hot Tank temperature, whose minimum value is 70 °C lower than the design temperature of 260 °C. Strategies C and D allow to contain the temperature drop within 30 °C and 10 °C, respectively. The best solution in terms of temperature drop reduction is the B case, which on the other hand is characterized by the slower and longer SOC increase (Figure 5.32(a)). The production of the A case is the less powerful: in fact, the lower the temperature, the lower the efficiency of the Power Block (Figure 5.32 (b)). C and D cases are distinguished by mutually similar power production curves, while B case has the higher power production,

but started some hours later with respect to the others. This is due to the postponed realization of the minimum SOC condition of 60% of the B case. Still looking at power production, but focusing on the shape of the curves of the different cases, the reference case A is characterized by a variable power curve, while other cases present more constant power curves. With the abovementioned general purpose to include CSP plants among dispatchable power plants, constant power profiles are surely solutions to be preferred. Since in the B case the Hot Tank is fed only at the design SF outlet temperature, also the Power Block is fed always at the design temperature. For this reason, the Power Block outlet temperatures of the B case are the highest. These temperatures influence the Cold Tank temperature (Figure 5.31 (b)) together with the SF recirculation temperature (in the B case); and this explains why the Cold Tank temperature of the B case is always the highest.

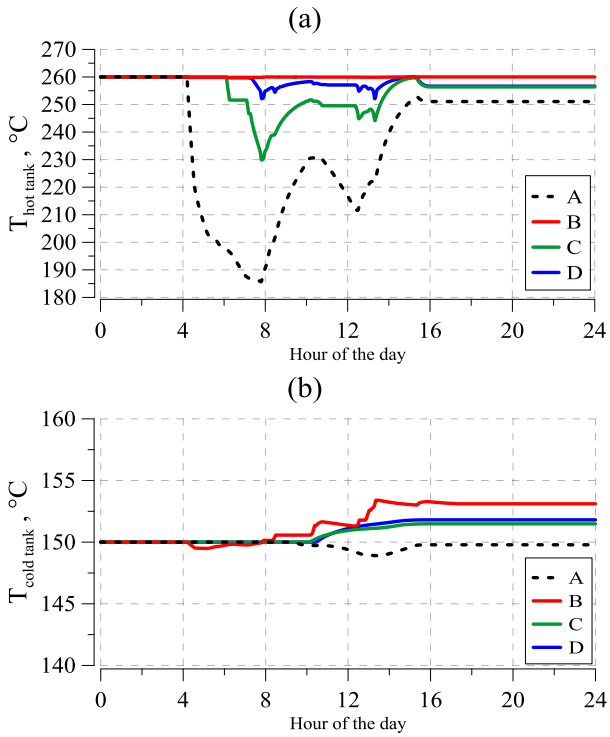

Figure 5.31. Hot and Cold Tank temperatures for the reference case (A) and the three recirculation strategies (B, C, D) of the variable-weather day.

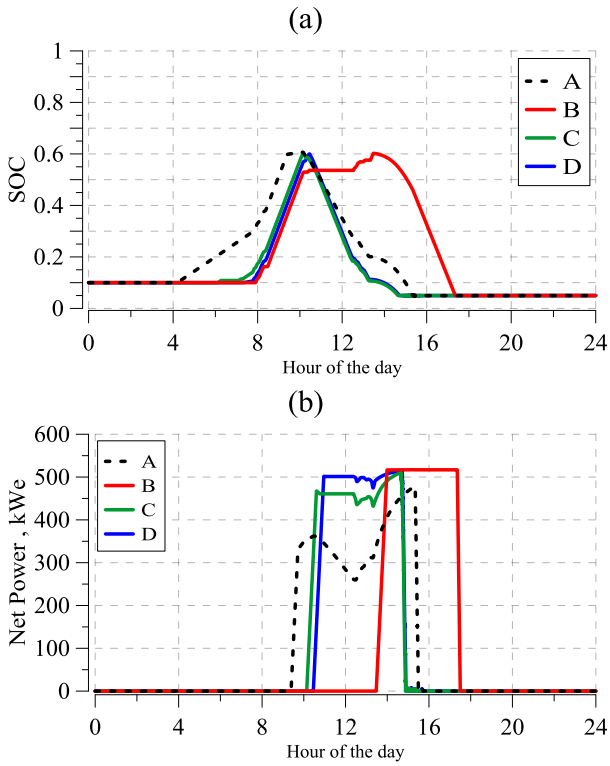

Figure 5.32. SOC and Net Power output for the reference case (A) and the three recirculation strategies (B, C, D) of the variable-weather day.

Bad-weather day

The different mass flow subdivision between Recirculation and Hot Tank for the bad-weather day is reported in Figure 5.33. It is worth noticing that in the B recirculation strategy the HTF ends to be delivered to the Hot Tank much earlier than in the others.

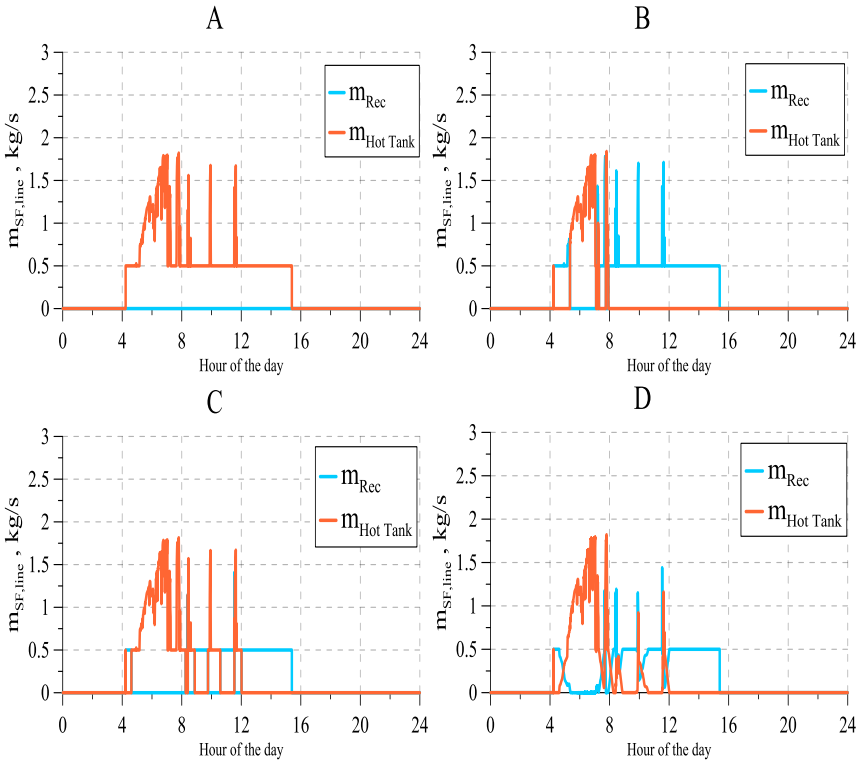

Figure 5.33. Recirculated and Hot Tank mass flows for the reference case (A) and the three recirculation strategies (B, C, D) of the bad-weather day.

With reference to the Hot and Cold Tank temperatures, the A strategy is characterized by very low temperatures of both the Hot and Cold Tanks. The Hot Tank temperature (Figure 5.34(a)) is low because the HTF is delivered here independently of its temperature, while the Cold Tank temperature (Figure 5.34(b)) is low because it is feed by the HTF coming

from the ORC, which works in a condition of strong partial load. The tank temperatures of the other cases present variations in the range of 20°C.

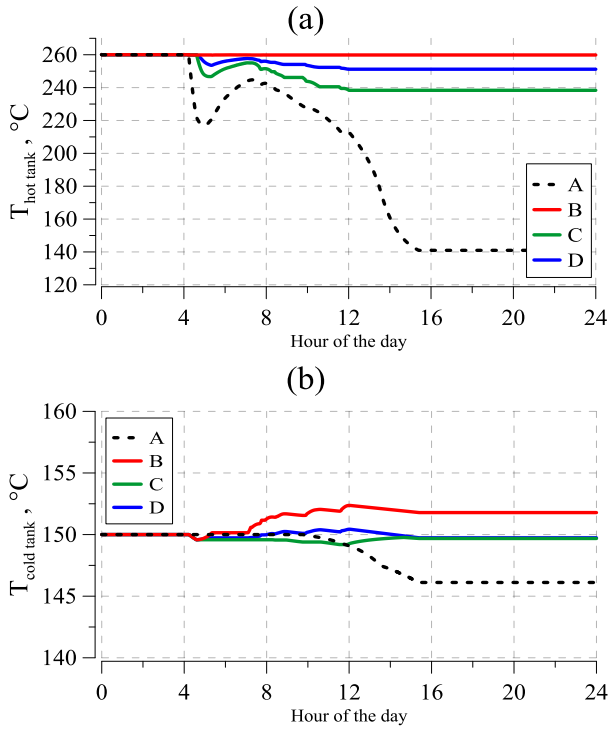

Figure 5.34. Hot and Cold Tank temperatures for the reference case (A) and the three recirculation strategies (B, C, D) of the bad-weather day.

A very important difference among the four strategies can be observed by Figure 5.35(a) and (b): in B and D cases the minimum level of SOC to start the ORC is not reached across the entire day, and for this reason the B and D cases present a null power production. A and C cases, on the other hand, allow to reach the minimum value of SOC and therefore in this cases can be achieved a power production.

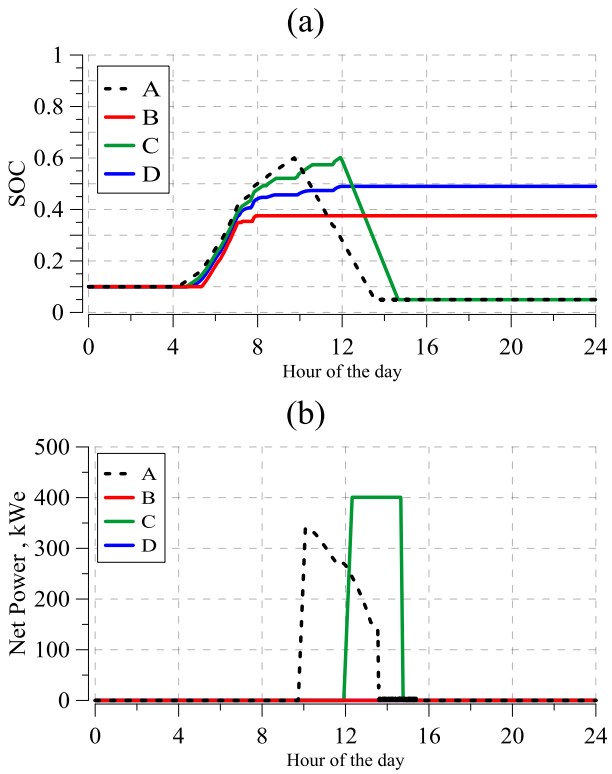

Figure 5.35. SOC and Net Power output for the reference case (A) and the three recirculation strategies (B, C, D) of the bad-weather day.

Table 5.3 shows the electric energy produced for the different recirculation strategies during the good, variable and bad-weather days and the variation of each case with respect to the reference case A.

The good-weather day is characterized by no substantial differences among the power productions of the different cases.

Negligible differences (within 1.5%,) can be noted also for the variable-weather day among A, C and D strategies, but a strong energy production loss (-8% with respect to the reference case A) is observed for the B recirculation strategy.

For the bad-weather day, the C strategy allows to reach the best performance in terms of electric energy production (+7% with respect to the A case).

Table 5.3. Electric energy (kWh/day) produced for the different recirculation strategies during the different days

	Recirculation strategy			
Day	**A**	**B**	**C**	**D**
Good-weather	5,563	5,468 (-1.7%)	5,564 (0%)	5,526 (-0.7%)
Variable-weather	2,085	1,917 (-8%)	2,065 (-1%)	2,056 (-1.4%)
Bad-weather	959	0 (-100%)	1,030 (+7%)	0 (-100%)

Results demonstrate that, independently of the weather, a partial recirculation of the SF, with respect to a not-partial recirculation, does not allow to achieve better results in terms of the overall system performance. In addition, by-passing the Cold Tank (A, C, D) in the recirculation process avoids a strong performance worsening with respect to passing it (case B).

For bad-weather days, differences among achievable performance are more evident: depending on the adopted recirculation strategy, a power production can be achieved or not during the day. It is worth noticing that the recirculation strategy C allows a substantial performance improvement for bad-weather days.

5.1.6. Dispatchability of a small-size CSP system

Hybrid plants are generally built to enhance the performance of single solutions. Before the assessment of the dispatch capability of the entire hybrid CSP-CPV plant, the results reported in the following pages represent a preliminary evaluation of the dispatch capability of the only CSP section of a generic small-size CSP-CPV plant.

The present study [73] has been performed by assuming a reference daily power output curve, which is characterized by a constant power output, a starting time and a duration period. The power ratio (π) is defined as the ratio between the requested power output and the reference CSP power output.

$$\pi = \frac{P_{REQ}\,(kW_{el})}{P_{REF}\,(kW_{el})} \tag{46}$$

As better explained by Figure 5.36, the performance parameter used in the present paragraph is the dispatch capability (δ), here defined as the ratio between the daily electrical energy effectively delivered by the system and the daily scheduled energy.

$$\delta = \left.\frac{E_{el,DEL}(kWh_{el})}{E_{el,SCH}\,(kWh_{el})}\right|_{day} \tag{47}$$

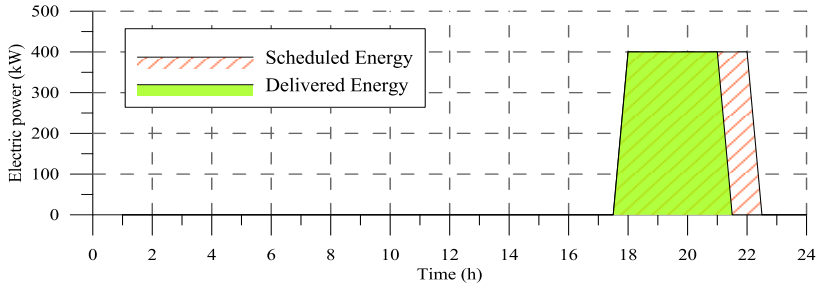

Figure 5.36. Scheduled and delivered energy

Every daily power output curve considered in the present study has a starting time placed after sunset, before sunrise or roughly around it. The analysis compares the dispatch capabilities of the CSP plant with the aim to evaluate the influence of:

- **Season**: the CSP plant is requested to provide the same daily power output curves for the four different seasons.
- **Starting time:** the CSP plant is requested to provide the same daily power output curves starting at different times, and seasonal results are shown.
- **Duration:** the CSP plant is requested to provide the same power ratio but with different time durations, for each season.

In order to evaluate the TES exploitation for each case examined, the final State of Charge (SOC_f) was also analysed. The latter is defined as the SOC of the Hot Tank immediately after the end of the daily power production period. The simulation has been carried out across an entire year and the initial SOC is assumed to be $SOC=SOC_{min}$.

The results are displayed for each season (Winter, Spring, Summer and Autumn) with reference to mean values. Each simulation was repeated with reference to different daily power output curves, characterized by π ranging from 0.30 up to 0.90, different starting times and time durations.

Season influence.

Figure 5.37 shows the mean seasonal δ of the CSP plant to provide a power output for 5 hours at different levels of π, ranging from 0.30 up to 0.90, starting at 6 p.m. As it can be seen, during spring and summer, δ is almost always above 0.9, and it slightly decreases as the parameter π increases. On the contrary, during both winter and autumn, the parameter δ is strongly influenced by the power output ratio π.

In Figure 5.38 the standard deviations of δ are displayed. Considering the reference year evaluated, while clear sky conditions often occurs during summer and spring, during winter and autumn the days are more often cloudy, causing higher standard deviations of δ. Furthermore, during spring and summer, the results for π=0.30 and π=0.45 are very similar: δ values are high and standard deviations are very low.

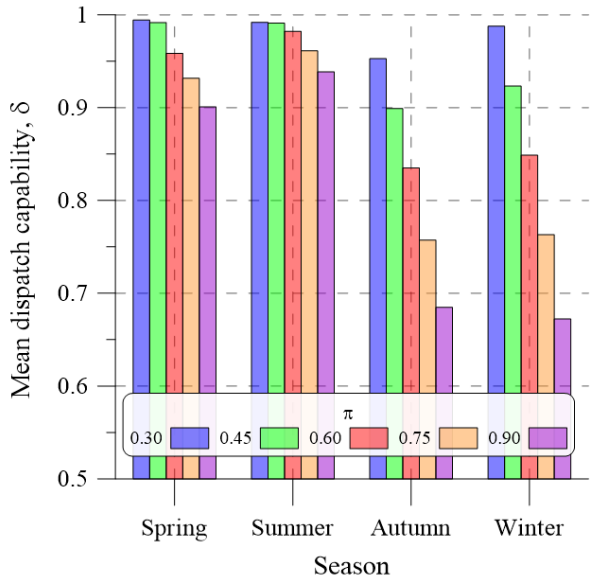

Figure 5.37. Mean δ related to the CSP plant (Electricity production from 6 p.m.to 11 p.m.)

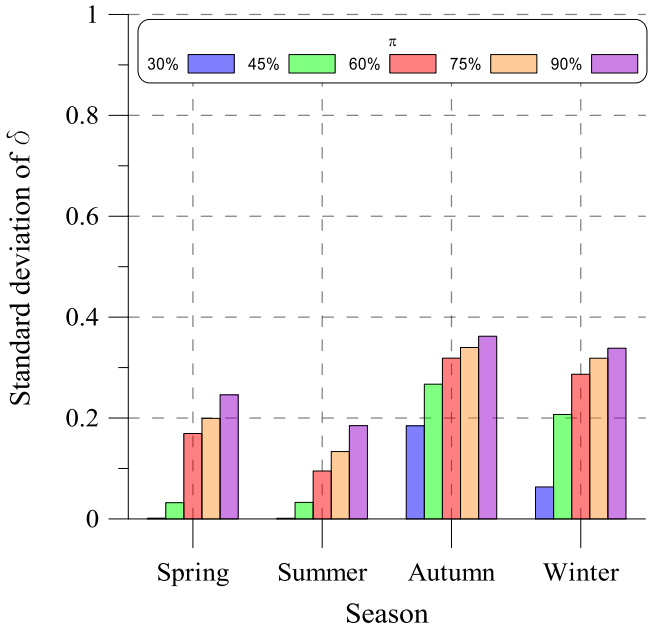

Figure 5.38. Standard deviation of δ related to the CSP plant (Electricity production from 6 p.m.to 11 p.m.)

Figure 5.39 illustrates the mean seasonal SOC_f of the CSP plant in the case of 5 hours of production, starting at 6 p.m., and different levels of power output. The seasonal mean value of the SOC_f can be considered as an index of the TES exploitation: in fact, high final values of the SOC_f mean that a large amount of energy is averagely stored in the TES, rather than be directly transferred to the Power Block and then converted to electricity. This is a useful information about the opportunity to increase the production hours, rather than a disadvantage for the power plant.

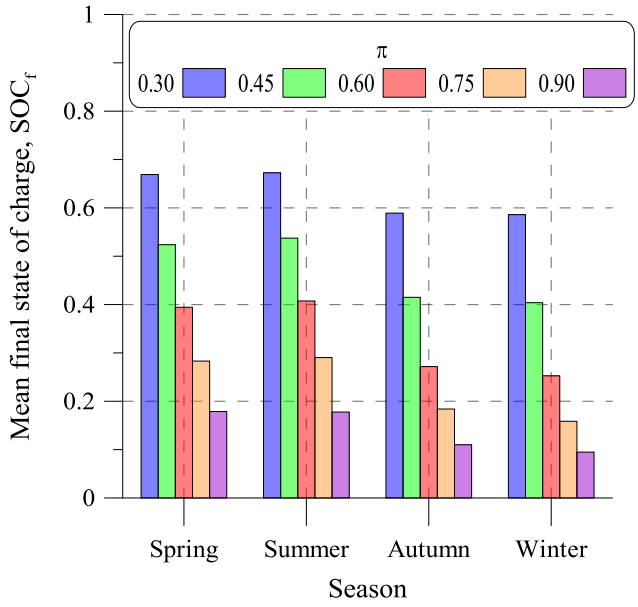

Figure 5.39. Mean seasonal SOC_f related to the CSP plant (electricity production from 6 p.m.to 11 p.m.)

Considering both Figure 5.39 and Figure 5.37, it is interesting to notice that high δ values match to high SOC_f values. In fact, considering that the energy management strategy does not use any weather forecast, high dispatch capabilities can be achieved only accepting low π values and therefore high SOC_f values.

Figure 5.40 shows the daily SOC trend during the first week of the year (from the 1st to the 7th of January), for an electricity production from 6 p.m.to 11 p.m. obtained with the available DNI shown in Figure 5.41.

Three power ratios π are displayed (0.30, 0.60 and 0.90). This figure clarifies the concept discussed above: as it can be seen, the daily SOC extensions of the lower power ratio cases are placed in the upper part of the graph. The maximum SOC level is often reached and therefore the thermal energy deliverable from the SF cannot be stored and defocusing of the SF is necessary. In particular, this happens often during the last four days of the week, with reference to the π=0.30 case.

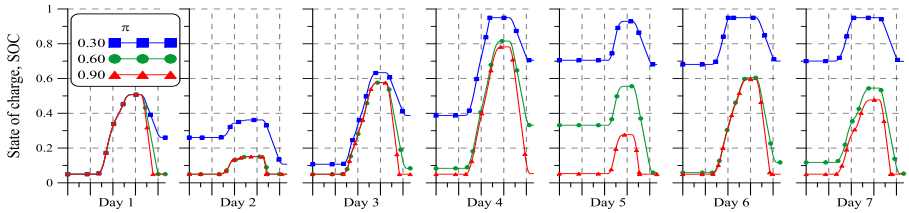

Figure 5.40. SOC of the week related to the CSP plant (Electricity production from 6 p.m.to 11 p.m.).

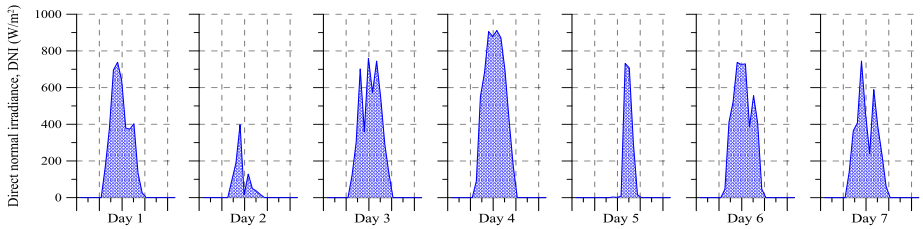

Figure 5.41. Direct Normal Irradiance from the 1st to the 7th of January of the reference year.

Starting time influence.

Figure 5.42(a-c), show the mean values of δ when producing the same daily power output curves starting at different times (6 p.m.to 11 p.m. and 12 a.m. to 5 a.m.), for each season. The figures show the cases π=0.30, π=0.60 and π=0.90. For each combination of season and π, the mean seasonal values of δ for the two different starting times are substantially the same and therefore it can be stated that their values are independent from the starting time. This is probably the greatest advantage of a CSP plant provided with a TES section: if the tanks are well insulated, their

thermal losses do not influence the power generation with a time shift of few hours.

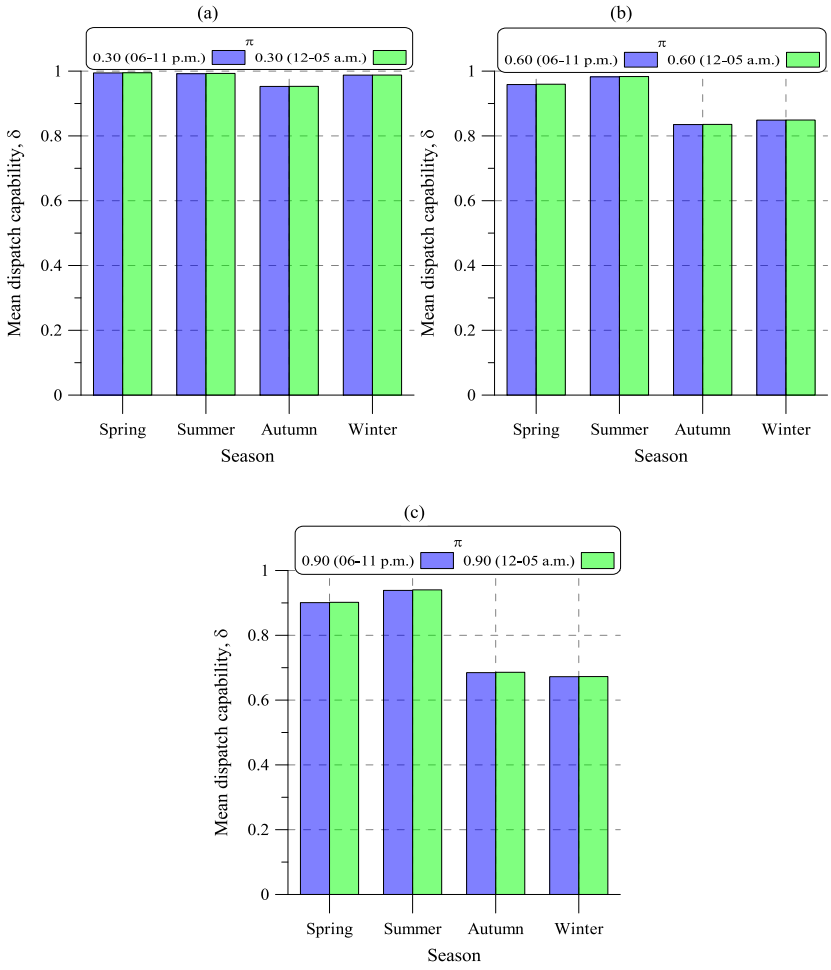

Figure 5.42. Mean δ related to the CSP plant for π =0.30 (a), π =0.60 (b) and π =0.90 (c) (Electricity production from 6 p.m.to 11 p.m. and from 12 a.m. to 5 a.m.).

Figure 5.43 and Figure 5.44 show the TES seasonal heat losses for the two cases (from 6 p.m.to 11 p.m. (a) and from 12 a.m. to 5 a.m. (b)). In the late-evening-case, the TES thermal losses are on average lower than in the early-morning-case one, because in this last case the HTF contained in the two tanks is stored for a longer time before being used. As it can be

seen, lower power ratios are closely related to higher TES losses, and this is due to a higher average SOC.

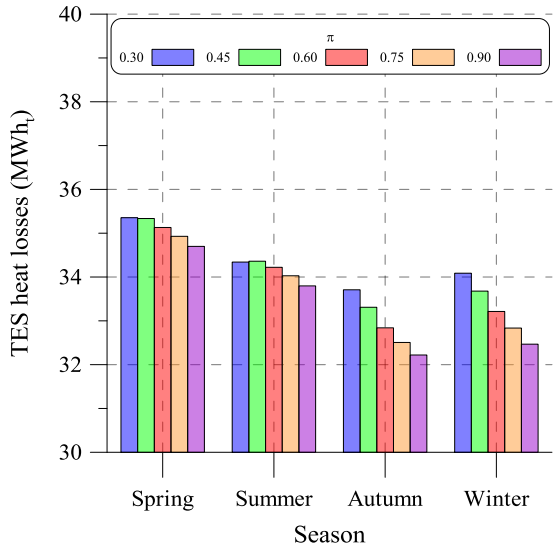

Figure 5.43. TES thermal energy losses from 6 p.m.to 11 p.m.

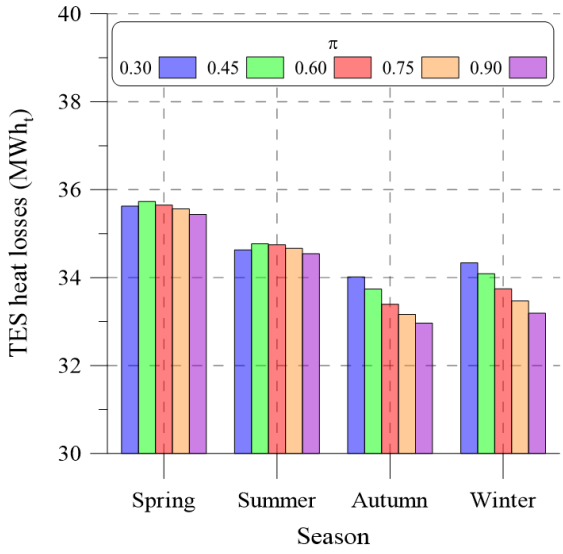

Figure 5.44. TES thermal energy losses from 12 a.m. to 5 a.m. .

Duration period influence.

Figure 5.45 highlights the variations of δ and Figure 5.46 the variations of SOC_f when the CSP system is asked to provide the same power output but with different time durations (6 and 7 hours), for a power ratio of 0.30, 0.45 and 0.60. Greater power ratios are not considered in this comparison because the storage capability does not allow a power ratio higher than 0.60 for more than 7 hours. Switch-off time is fixed for all the cases at 5 a.m. and start-up times are 10 p.m. and 11 p.m., respectively.

As it can be seen in Figure 5.45 the gap between the mean dispatch capabilities δ of the two time durations becomes wider for high power ratios, especially during autumn and winter. During winter and autumn, the values of δ of the longer-lasting case are significantly lower, while during summer and spring they are comparable and always above 0.9, even if the power production starts one hour in advance. In fact, during spring and summer the collected solar energy is enough to guarantee high levels of δ even for longer-lasting cases, while this does not happen in the winter and autumn cases. Figure 5.46 shows the mean SOC_f connected to the values of δ shown on the left. It is remarkable that during spring and summer δ is considerably high even for π=0.60, due to a better exploitation of the TES capacity (as demonstrated by the lower SOC_f values). Therefore, during summer and spring, time durations can be extended without a significant decrease of the dispatch capability.

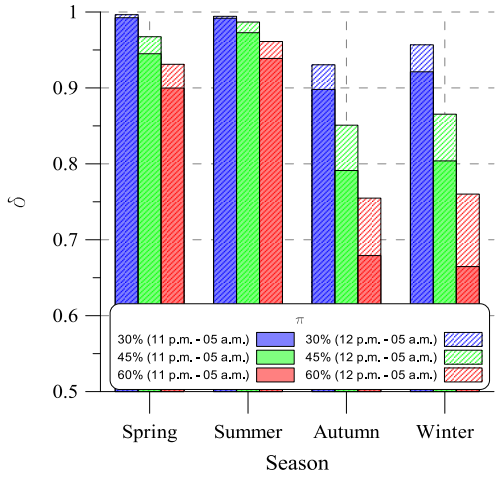

Figure 5.45. Mean seasonal δ for different durations.

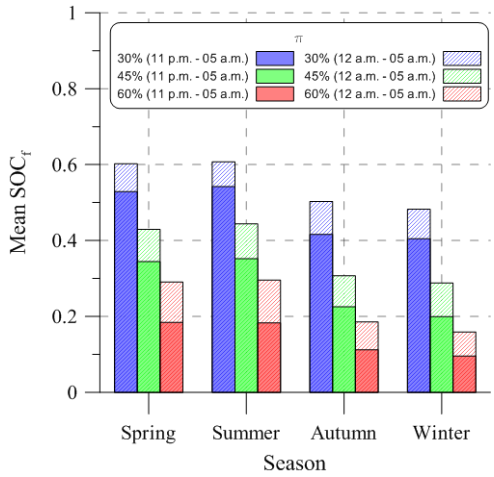

Figure 5.46. Mean SOC_f for different durations.

Yearly results.

Figure 5.47 shows the mean dispatch capability in function of the yearly energy production for different values of the power ratio. Figure 5.47 demonstrates that the highest mean yearly capabilities are obtained for the lowest yearly energy productions. A yearly average value of δ around 0.8 allows to almost triple the energy production with respect to the 0.30 case.

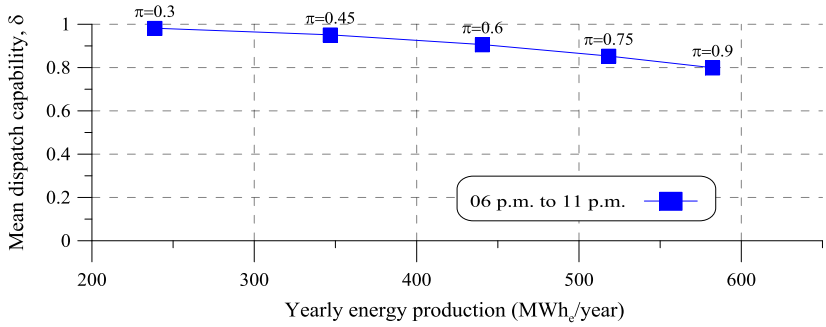

Figure 5.47. Yearly energy production and mean dispatch capability δ.

Table 5.4 reports the seasonal and yearly energy production for π from 0.30 to 0.90 of the late evening case (6 p.m.to 11 p.m.).

Table 5.4. Seasonal energy production of the CSP plant (Dispatchability of a small-size CSP system).

	Power ratio π	**6 p.m.to 11 p.m. (Late evening case) (MWhel)**
Spring energy production	0.30	60.73
	0.45	90.88
	0.60	117.27
	0.75	142.48
	0.90	165.25
Summer energy production	0.30	60.56
	0.45	90.79
	0.60	120.11
	0.75	146.71
	0.90	172.15
Autumn energy production	0.30	58.02
	0.45	82.08
	0.60	101.21
	0.75	114.88
	0.90	124.42
Winter energy production	0.30	59.45
	0.45	83.08
	0.60	101.93
	0.75	114.22
	0.90	120.46
Yearly energy production	0.30	238.76
	0.45	346.83
	0.60	440.52
	0.75	518.29
	0.90	582.27

The results of the performance assessment reported above demonstrate that the dispatch capabilities of the analysed CSP plant are of great interest, especially during summer and spring. In particular, the study shows that the CSP plant is able to effectively delivery over 90% of the daily scheduled energy during spring and summer for any power ratio from 0.30 to 0.90. On the contrary, during the other seasons the power output has to be reduced to 30-45% of the nominal value in order to achieve acceptable dispatch capabilities. The lowest standard deviations of dispatch capability are obtained during spring and summer for power ratios of 0.30 and 0.45, while the influence of the daily weather on the dispatch capability is stronger for higher power ratios.

A very positive result is that the storage thermal losses do not significantly reduce the dispatch capabilities of the CSP plant and that the power generation phase can be achieved with almost no differences between late evening or early morning.

However, these results suggest that the adoption of an optimal management strategy using weather forecast to define the power generation curve could significantly enhance the capabilities of CSP plants to provide *dispatchable* power.

5.2. Dispatchability of a medium-size hybrid CSP-CPV system

The results of the optimization of the energy fluxes coming from the different sections of the hybrid CSP-CPV system, under the two integration strategies P-INT and F-INT[2] previously described, are reported in the following, with reference to the technical data and assumptions of the Ottana Solar Facility.

The evaluation of the system performance was carried out comparing the two proposed control strategies F-INT and P-INT, for daily power output curves characterized by power outputs ranging from 200 kW to 1 MW and optimized potential time durations. To compare the two control strategies, the performance assessment is firstly presented on a daily basis, with reference of two typical days, one during summer and the other during winter, and subsequently extended to a yearly basis analysis.

Daily analysis

The daily analysis was performed considering a time horizon of 24 hours in the definition of the optimal power plant management, with an imposed power output and a given initial SOC of the two storage systems. It's important to highlight that the final SOC is not fixed, and therefore it can be different for the two strategies.

[2] *In the Full Integration (F-INT) strategy the two CSP and CPV systems operated in a synergetic way to supply the required and fixed power output* P_{OUT} *(*$P_{OUT}(t \in \tau) = const.$*). The control system optimizes the share of CSP and CPV power production by maximizing the corresponding potential time duration* τ*.*

In the Partial Integration (P-INT) strategy the two CSP and CPV systems operated independently but always with reference to a single power delivery point. In this case, the control system maximizes the corresponding potential time duration τ *for a fixed share of CSP and CPV power productions (*$P_{CSP}(t \in \tau) = const.$; $P_{CPV}(t \in \tau) = const.$*).*

The two different power output curves related to a typical summer day with a fixed power output (P_{OUT} =500 kW) and an initial SOC_{TES} of 50% are shown in Figure 5.48. Thanks to the optimization of the CSP and CPV power share, a constant power curve can be achieved in the F-INT case for 19 hours. During the first and last hours of the day, the high storage capacity of the TES was used to feed the ORC and to produce the desired power output while the contribution of the CPV was negligible. Thus, the CPV was mainly used during the middle of the day, while the energy produced by the SF was partially stored in the TES system. A portion of the stored thermal energy was then used in the evening. At the end of the day, the energy produced by the CSP was 4.7 MWh with an average ORC efficiency of 17.7%, while the CPV section contributed with 4.8 MWh. Instead, in the P-INT case the potential output curve duration was strongly constrained by the shorter time duration of the CPV unit, which was able to deliver the desired power output only for 13 hours. In this case, the energy production of the CSP and CPV sections were 3.9 MWh and 2.9 MWh respectively with an average ORC efficiency of 18.2%. This highlights the main drawback of using the P-INT strategy with respect to F-INT, since the system was unable to fully exploit the dispatchability potential of the CSP plant and the high conversion efficiency of the CPV section.

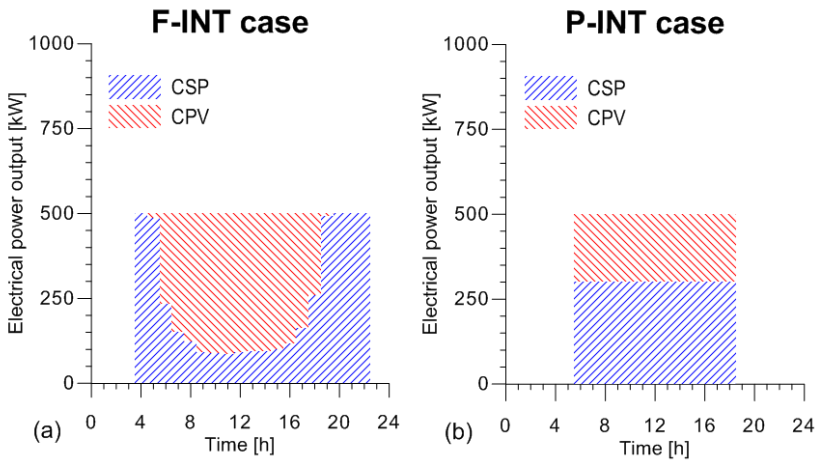

Figure 5.48. Power output curves during a summer day (P_{OUT} =500 kW) for (a) F-INT and (b) P-INT systems.

The two storage systems have a central role with reference to the system's ability to provide dispatch power with a fixed power curve. Both the TES and batteries have the important task of smoothing power production fluctuations mainly connected to the DNI variation. Moreover, the TES system enables achievement of an important time-shifting of the energy produced by the SF, thus favouring CSP power production during the hours of low solar radiation. An example of the main F-INT energy flows and the SOC of the two storage systems during a summer day is given in Figure 5.49. In particular, Figure 5.49 (a) highlights the early morning and late evening use of stored energy to feed the ORC unit and to provide the desired power curve even though solar radiation is still low, with a consequent SOC_{TES} decrease. On the contrary, a surplus of energy production from the SF occurs in the central hours of the day. Only a constant share of this energy is used by the ORC and the surplus is stored until the TES is fully charged. After this moment, the surplus of energy can no longer be stored and a partial defocusing of the mirrors is required to satisfy the energy balance of the CSP plant and avoid high and dangerous oil temperatures (at the end of the day the overall energy losses for defocusing are 25.7 MWh_{th}). Figure 5.49 (b) shows CPV power during the day and also indicates how the batteries are used to keep the power output of the hybrid plant constant. However, the batteries are used only during hours of solar energy availability and cannot be used in other periods because of their low storage capacity.

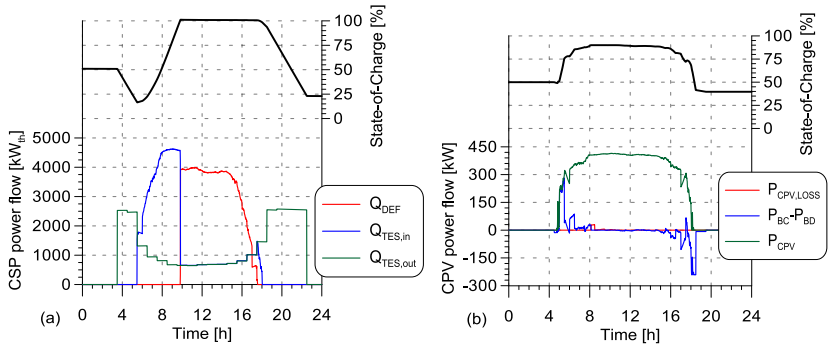

Figure 5.49. Main energy flows of the CSP(a)-CPV(b) plant during a summer day for the F-INT case.

Figure 5.50 shows the main energy flows related to the P-INT case and demonstrates the differences between the two management strategies applied to the storage systems. In particular, a less deep discharge of the TES system occurs throughout the day for the P-INT case while the energy produced by the SF and directly used by the ORC increases. In this way, the defocusing energy losses are reduced to 20.45 MWh_{th}. Moreover, in the P-INT case, the constraint of a constant delivered power of the CPV together with the low storage capacity of the battery bank causes the reduction of the CPV power production. This fact represents the main energy losses of the CPV section, which account for 44% of its daily energy production. With the adoption of the F-INT strategy these energy losses are avoided and the CPV energy production is completely exploited.

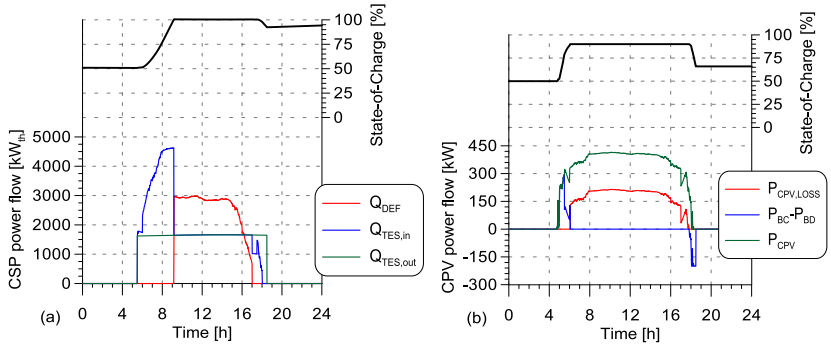

Figure 5.50. Main energy flows of the CSP(a)-CPV(b) plant during a summer day for the P-INT case.

Figure 5.51(a) shows the possible combinations of different values for P_{OUT} and the corresponding maximum potential duration τ for the F-INT and P-INT control strategies. The coloured areas of the figure represent and highlight the large number of choices that can be made with an integrated strategy. In fact, the maximum τ curves represent the upper limits of each strategy but obviously any briefer τ can be chosen for a certain P_{TOT}. Curves in Figure 5.51 (a) are plotted with reference to an initial SOC_{TES} condition equal to $SOC_{TES,MIN}$ and Figure 5.51 (b) illustrates the range of maximum potential durations τ with reference to different

initial SOC_{TES} conditions between $SOC_{TES,MIN}$ and $SOC_{TES,MAX}$. Figure 5.51 (b) reveals another very important advantage of using a F-INT strategy, since its benefits are independent of the initial SOC_{TES}. In fact, the P-INT curve is always below the F-INT curve, and the gap is wider for the lowest values of $P_{OUT.}$

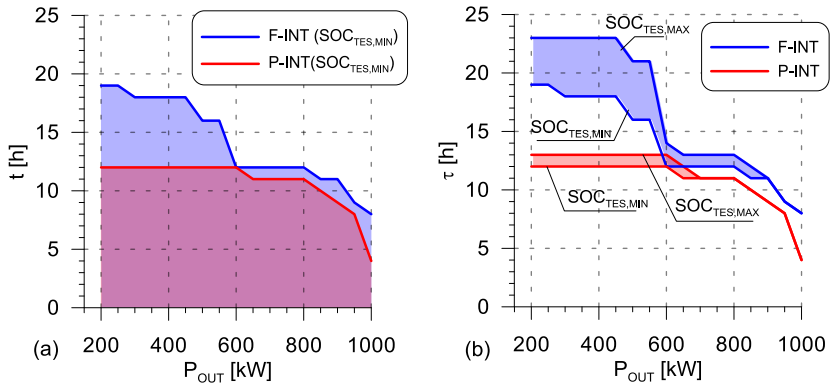

Figure 5.51. Maximum potential time duration for a summer day as a function of power output for an initial SOC_{TES} equal to (a) $SOC_{TES,MIN}$ and (b)its range.

Considering that both DNI and daylight are lower during winter, the average duration times are also consequently lower with respect to the summer case. Figure 5.52 shows the achievable output power curves during a typical winter day, when the F-INT strategy can guarantee a duration time of 9 hours, while with the P-INT only 6 hours are obtained. The higher duration time is mainly achieved thanks to the higher exploitation of the energy produced by the CPV section (2.3 MWh for F-INT and 1.4 MWh for P-INT) while the energy production of the CSP section is almost the same for the two strategies (2.2 MWh for F-INT and 2.1 MWh for P-INT).

Figure 5.53 shows the main energy flows of the hybrid CSP-CPV system for the winter case and demonstrates that the thermal storage is used to guarantee the constant power output and the SOC_{TES} is reduced across the day. The batteries are charged during the middle of the day and the stored energy is then used in the early afternoon. Compared to the

summer case, due to the more frequent occurrence of P_{CPV} fluctuations, the role of batteries becomes fundamental in reaching the desired power output. Finally, the state of charge of the batteries always remains within the range imposed, by avoiding the energy losses due to a full charge of the batteries ($P_{CPV,LOSS}$=0 for F-INT case). This is a relevant difference with the P-INT case (Figure 5.54), which leads to $P_{CPV,LOSS}$ of about 0.75 MWh. Unlike the summer case, no relevant differences are observed in the main energy flows involving the CSP section between the F-INT and P-INT cases.

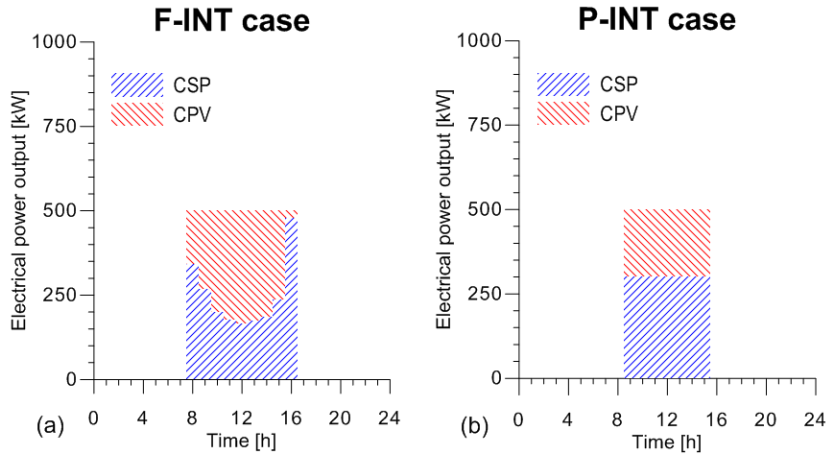

Figure 5.52. Power output curves during a winter day (P_{OUT} =500 kW) for (a) F-INT and (b) P-INT systems.

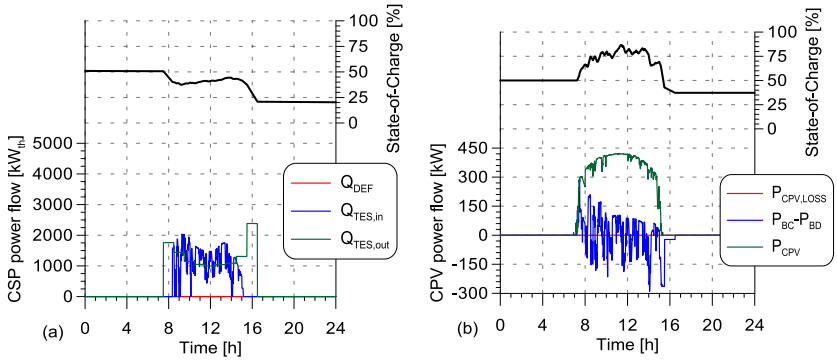

Figure 5.53. Main energy flows of the CSP(a)-CPV(b) plant for a winter day for the F-INT case.

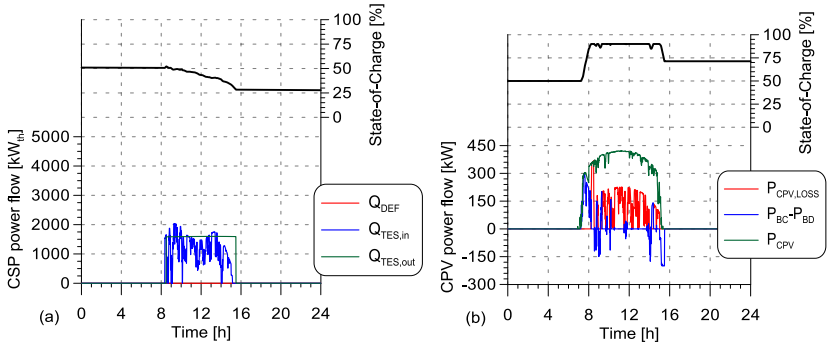

Figure 5.54. Main energy flows of the CSP(a)-CPV(b) plant for a winter day for the P-INT case.

The maximum potential time duration is shown in Figure 5.55(a) and (b) and even in the winter case the F-INT strategy allows reaching higher τ values. In any case, the P-INT strategy is severely limited by the CPV section, especially for lower power outputs, when the maximum potential time duration is strongly constrained by the low storage capacity of the CPV section. Comparison of the maximum potential time duration curves for the summer (Figure 5.51(b)) and winter (Figure 5.55 (b)) cases highlights the different effect of the initial SOC_{TES} on the τ value. In fact, while during summer days the difference between $\tau_{SOC=MIN}$ and $\tau_{SOC=MAX}$ is in the range of few hours, during the winter days this difference strongly increases to an average value of 10 hours.

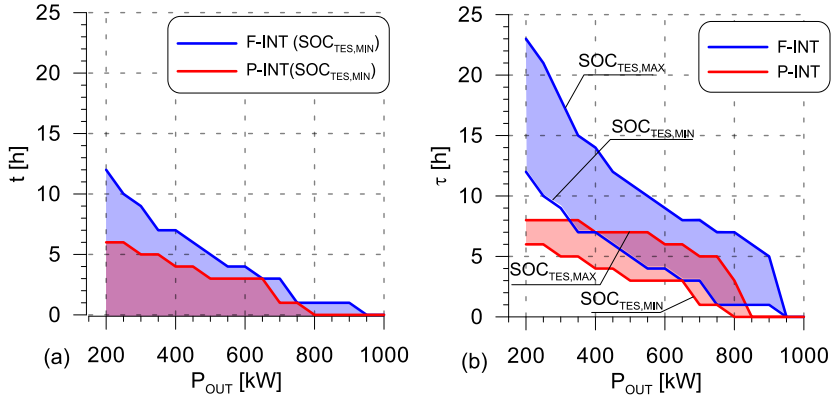

Figure 5.55. Maximum potential time duration for a winter day as a function of power output for an initial SOC_{TES} equal to (a) $SOC_{TES,MIN}$ and (b)its range.

Yearly analysis

As already mentioned, it is difficult to know the power curves that will be required during the actual operating phases of the hybrid CSP-CPV plant. However, the results of a first assessment of the annual performance achieved with the assignment of planned output curves are discussed in the following.

Owing to the absence of any other optimization target, the energy management strategy was set to maximize the energy production by keeping a constant power output POUT for a certain duration τ during the day. In particular, for each day of the year, the control system arranges the energy flows to find the values of POUT and τ that maximize the energy production for the following 72 hours. Therefore, for each day the initial state-of-charge of the two storage systems was not imposed but depends on past operating conditions of the hybrid plant. Table 5.5 summarizes the results of the annual simulation of the two main sections of the hybrid plant.

The comparison of the results achieved with the two control strategies proves better performance of the F-INT strategy in terms of annual energy production and hours of potential time duration. This result is mainly achieved by a better exploitation of the CPV potential, as demonstrated by its higher energy production and average efficiency. Because of the battery bank is designed for the short-term energy storage and therefore it is unable to achieve a time-shifting of the CPV energy production, the exploitation of the current CPV power becomes fundamental to avoid the fully charge of batteries and the consequent energy losses. It is worth noting that for the P-INT case the energy losses due to the impossibility of storing the CPV excess power are more than double compared to those of the F-INT approach. On the contrary, the adoption of the F-INT control strategy worsens the CSP performance. In particular, owing to the priority given to the direct use of the CPV power, the ORC often works at partial load during the daily hours with a consequent decrease of its efficiency. Instead, with the P-INT strategy the power output curve is often covered by the sole contribution of the CSP section and therefore the ORC unit operates at higher load and with greater efficiency. Nevertheless, a lower number of start-ups of the ORC unit with the F-INT solution is observed,

with a consequent decrease in ORC start-up losses and a prospective longer lifetime of this unit.

Table 5.5. Annual performance of the hybrid CSP-CPV system for different control strategies (Dispatchability of the hybrid system).

	F-INT	**P-INT**
CPV section		
CPV energy production (MWh/year)	650	473
CPV losses (MWh/year)	153	335
Battery losses (MWh/year)	14	7.3
CPV average efficiency	19.9%	13.7%
CPV running time (h)	3,111	2,455
CSP section		
CSP energy production (MWh/year)	980	1,100
SF energy production (MWh/year)	5,496	5,496
TES energy losses (MWh/year)	169	169
Defocusing energy losses (MWh/year)	777	257
ORC average efficiency	18.5%	19.1%
ORC running time (h)	2,703	2,455
ORC start-up	250	305
hybrid CSP-CPV system		
CSP-CPV energy production (MWh/year)	1,630	1,573
CSP-CPV potential time duration (h)	3,561	2,938

Moreover, the defocusing energy losses are very high for the F-INT case, because of the use of the CPV during the middle of the day, which penalizes the CSP energy production. Therefore, the F-INT strategy would take the best advantages in terms of energy production from an

increase in TES storage capacity. This also means that the TES storage capacity must be chosen in accordance with the plant operation strategy.

As stated previously, the hybrid CSP-CPV solution is proposed to improve the dispatchability of Solar Power Plants rather than to increase their energy production. The definition of a fixed power curve results in a decrease in energy production for both the CSP and CPV plants, since without this constraint the annual energy production would be about 800 MWh for the CPV plant and 1,150 MWh for the CSP plant. Therefore, the introduction of the power curve constraint causes only a marginal penalization of annual energy production of the CSP section, especially with the P-INT strategy, thus confirming the good capacity of the CSP to follow desired output curves. On the contrary, due to the inability of CPV to carry out dispatch tasks a reduction of 20% and 40% in the CPV energy production is observed in the F-INT and P-INT strategies respectively. Therefore, the greater involvement of the CPV plant is another important result of the F-INT case strategy.

As mentioned, Table 5.5 refers to different power output curves throughout the year, obtained by maximizing the energy production. On the contrary, Figure 5.56 (a) shows the yearly energy production of the two different integration strategies of the CSP-CPV plant if a constant power output is imposed throughout the year. For both F-INT and P-INT strategies, a large reduction in annual energy production occurs with respect to the previous case shown in Table 5.5. The maximum yearly energy production is reached for a P_{OUT} in the range of 500-700 kW, which allows the achievement of the best balance between energy production and storage capacity. Production curves with lower power outputs lead to correspondingly high potential duration times and an intense use of the two energy storage systems. The latter occurs both during daylight hours, when the large energy production from the SF has to be stored because of low ORC thermal demand, and during the night hours, when energy production only depends on the energy stored. Vice versa, the fulfilment of power output curves close to the nominal value is achieved only for few hours during the day, exclusively during daylight hours.

Figure 5.56 (b) shows the annual average value of time duration τ as a function of P_{OUT}. In the F-INT case, although the duration time of the CSP

and CPV plants is forced to be the same, the share of the CSP and CPV contribution is optimized by the control system to obtain the desired power output by maximizing τ. In the case of P-INT, both the CSP and CPV plants have to provide by themselves a given share of the power output without any cooperation between the two storage systems. Therefore, the two plants are very often forced to operate at partial load conditions throughout the year and with significant constraints in the management of the two storage systems. Comparison of the P-INT and F-INT cases for the hybrid CSP-CPV system in Figure 5.56 (a) demonstrates that the F-INT case allows the highest energy production and corresponding highest potential duration for any power output. The dotted lines represent the share of the CPV section on total energy production with reference to the P-INT and F-INT cases. Although the CPV share is low, even this section benefits from the F-INT strategy, which leads to the increase of the CPV annual energy production for any power output.

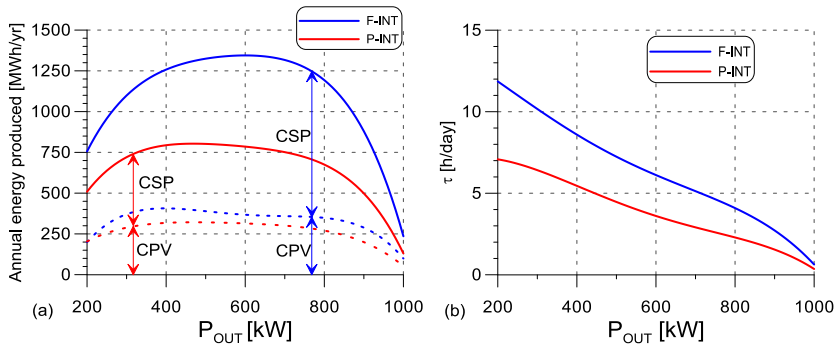

Figure 5.56. Annual energy production and potential time duration for fixed power outputs.

In conclusion, the integration of different solar power plants and energy storage systems may be an interesting option to mitigate the effects of the variability and intermittency of solar energy and to provide ancillary services to the energy distribution network.

The results of this study show the advantages of using an integrated management strategy to satisfy a constant power output curve.

Optimization of the CSP and CPV power share leads to an effective use of the dispatch capabilities of the CSP plant owing to the presence of the TES section, while the CPV plant is fully exploited, especially during the hours of high solar radiation. Comparison of the results achieved with the F-INT and P-INT control strategies demonstrate that the F-INT solution leads to better performance in terms of annual energy production and hours of potential time duration with fixed power outputs.

The advantages of integrated management of the CSP and CPV plants are obviously closely related to the required service of the plant and therefore to the required power output curves. On the other hand, the latter depend on many external factors, which are beyond the scope of this thesis. In particular, it appears likely that the power output curves of these power plants will be defined in accordance with the economic value of such service on the market.

Moreover, the study also shows that the dispatchability features of these hybrid plants strongly depend on the capacity of the two energy storage systems, and especially on the TES section. For this reason, the storage capacity of the hybrid plant should be carefully optimized to fit the desired power output curves.

5.2.2. Influence of the design criteria on the dispatch capability of a hybrid CSP-CPV system

The design choices of the components of a hybrid CSP-CPV system can be very numerous and their combination almost countless. Once fixed the design power capacity and selected the technology, for example, different power shares between the two major sections (CSP and CPV) can be chosen. Moreover, the TES capacity as well as the Solar Multiple are other CSP design criteria that are usually selected following, as expected, techno-economical, safety, land requirement, legislative limits and so on.

With the double intention to study the influence of some design criteria on the dispatch capability of the hybrid system and to justify the Ottana Solar Facility design choices, the present paragraph reports an analysis on the dispatch capability of various hybrid-CSP-CPV component combinations, all characterized by an overall system power capacity of 1 MW.

The fixed overall power capacity of 1 MW can be obtained with different power shares between the two CSP and CPV sections (the theoretical limits are 1 MW of CSP and 0 MW of CPV and 0 MW of CSP and 1 MW of CPV). For this reason, a proper design factor has been here introduced. The power ratio (γ) is the ratio between the CSP nominal power and the CSP+CPV nominal power (keeping a constant value of 1 MW). Therefore, γ =1 identifies the case of only CSP while γ =0 only CPV. The Solar Multiple is also considered as a design factor, and it is defined as the ratio between the thermal power produced by the SF at the design point and the thermal power required by the PB at nominal conditions. The third important design factor considered in the present study is the TES capacity (h_{TES}), which is the capacity of the CSP storage section in terms of operating hours of the power block at nominal conditions. The CPV storage is represented by electric batteries with a capacity of 1 hour, in any case.

The impact of the three aforementioned design factors in the system performance is analyzed. The main output parameters are examined varying simultaneously the three design factors, because the

interdependence between these parameters cannot be neglected and the analysis on a single parameter (keeping the other factors constants) could be not thorough.

Since the availability of large land areas could be an important constraint somewhere, the results are shown with reference to the specific energy production of the hybrid system, defined as the ratio between the annual energy production and the land area occupied by the Solar Field.

Figure 5.57 shows the specific energy production that can be achieved, in function of the solar multiple (SM), the TES capacity (h_{TES}) and the power ratio (γ), by adopting the constant power output strategy discussed thoroughly in the previous paragraphs. Moreover, the figure shows the dispatch losses, defined as the reduction in annual energy production with respect to the energy produced and directly delivered to the grid without using any dispatch strategy. Values of the specific energy production and dispatch losses for the theoretical limit of $\gamma=0$ (the entire system is represented by CPV), which are obviously independent from the solar multiple and TES capacity, are reported as dashed lines in Figure 5.57.

Since the CSP-CPV power output strongly depends on the direct component of the sun radiation, the adopted constant power output strategy has to find the best compromise between nominal power output and time duration of the energy delivery. Therefore, a constant power production often involves a time-shifting of the energy production, and the hybrid plant greatly benefits from high values of the TES storage capacity and of the power ratio. In particular, the benefits coming from the increase of the TES capacity become relevant with the increase of the solar multiple and the consequent increase of excess thermal energy that can be stored. The maximum energy production per land area is found for a TES capacity of 12.5 h, while the optimal solar multiple increases with the power ratio.

Even if the CPV plants usually present higher conversion efficiencies in comparison with CSP, their energy production is not firm and easily storable as that of the CSP plant, as also demonstrated by the lower graphs of Figure 5.57. The very high dispatch losses (30%) estimated for the $\gamma=0$ case highlight the inability of the CPV to provide constant power curves. A linear rise of the dispatch losses with the solar multiple is observed for $\gamma=0.2$, while the TES capacity influence is essentially irrelevant. With the

weight increase of the CSP on the overall energy production, the TES capacity impact on the dispatch loss acquires an increasing importance and the latter is minimized for a Solar Multiple of about 1.5-2. As it can be seen, the higher the CSP share, the smaller the dispatch loss.

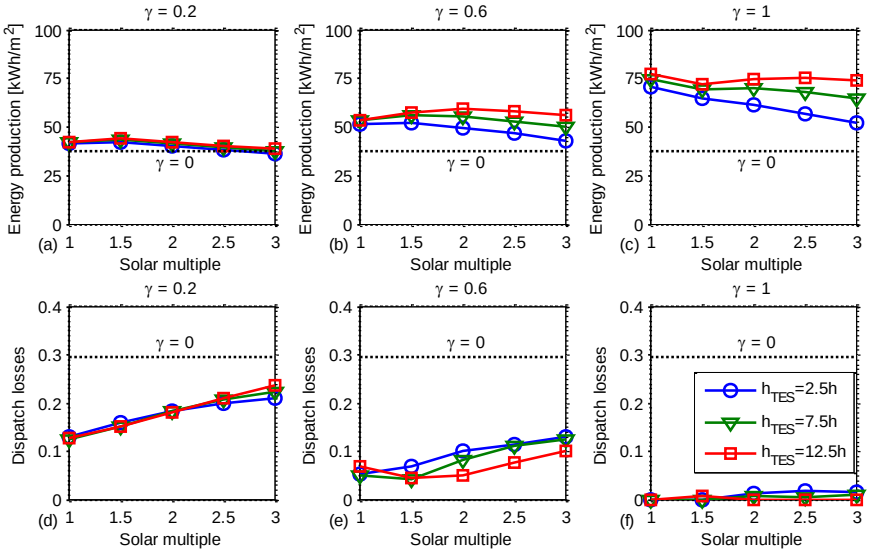

Figure 5.57. Effect of the three design factor on the specific energy production and dispatch losses.

In particular, it is worth noticing that higher power ratios allow both better dispatchability performance and energy productions and bigger thermal energy storages allow higher energy productions but no relevant variations in the dispatch capability.

For the specific case of the Ottana Solar Facility, which is characterized by a configuration, according to the present paragraph, identified as γ=0.6, SM=1.56 and hTES=5, it can be concluded that the adopted design criteria maximize the specific energy production and minimize the dispatch losses.

Chapter 6

Conclusions and future research

The research of the present Ph.D. has been carried out in order to study the performance of medium-size hybrid CSP-CPV systems designed for improving the dispatchability of Solar Power Plants and to develop novel management strategies for this kind of plants.

The different studies have been performed considering the Ottana Solar Facility, whose technical data were known by the author and where the experimental tests and model validation are going to be carried out.

Novel simulation models have been developed, aimed to better study the behaviour of medium-size hybrid CSP-CPV systems, at different levels of complexity and including different management strategies.

The results obtained by making use of a non-stationary one-dimensional model and a non-stationary two dimensional model for the Solar Field dynamic behaviour modeling, allowed to conclude that the simplified one-dimensional model is confidently usable for control and management purposes.

The analysis of the effects produced by the adoption of a recirculation strategy in a line-focus Solar Field demonstrate that, independently of the weather, a partial recirculation of the Solar Field, with respect to a full recirculation, does not allow to achieve better results in terms of the overall system performance.

The results of the performance assessment of the overall CSP section demonstrate that the dispatch capabilities of this technology are of great interest, especially during summer and spring.

When considering the overall hybrid CSP-CPV system, the conclusion of the research shows the advantages of using an integrated management strategy to satisfy a constant power output curve. Optimization of the CSP and CPV power share leads to an effective use of the dispatch capabilities of the CSP plant owing to the presence of the TES section, while the CPV plant is fully exploited, especially during the hours of high solar radiation. Comparison of the results achieved with the two proposed control (full and partial) strategies demonstrate that the full integrated solution leads to better performance in terms of annual energy production and hours of potential time duration with fixed power outputs. The advantages of an integrated management of the CSP and CPV plants are obviously closely related to the required service of the plant and therefore to the required power output curves.

This Ph.D. research is part of the growth of the knowledge on hybrid CSP-CPV systems designed for improving the dispatchability of Solar Power Plants and demonstrates the improvement of the power dispatchability that can be achieved with a suitable integration of Concentrating Solar Technologies, helping to move this green technology a bit closer to the word *dispatchability*.

6.1. Future research

Because of the delay in the construction, the test phase of the developed simulation models and the experimental validation of the results in the Ottana Solar Facility are the principal challenging objectives for the author near future work.

In addition, since appears likely that the power output curves of these hybrid solar facilities will be defined in accordance with the economic value of such service on the market, those aspects will be deeply investigated in a future work: a feed-in tariff for the remuneration of the dispatchability and the possibility to provide ancillary services from a Renewable Energy Source power plant will be proposed.

Another research idea for the future, conceived while studying the recirculation strategies of the Solar Field, is to study the influences that the inclusion of the Hot Tank in the recirculation can have on the plant warm-up.

Moreover, a study on the influence of the stratification inside the storage tanks on the tanks' thermal losses will be carried out.

Author's note

As it often happens while studying something you really love, lots of (probably the best) ideas come to your mind along the way, unexpectedly and magically; after all

If we knew what it was we were doing, it would not be called research, would it?

Albert Einstein

Nomenclature

Symbols

c_p	Specific heat capacity at constant pressure (J/kg·°K)
E , e	Energy, generic (J, kWh)
F	Shape factor
g	Gravitational acceleration (m/s^2)
h	Convective heat transfer coefficient ($W/(m^2 \cdot K)$
k	Kinetic energy (J)
l	Length (m)
$\dot{m}$	Mass flow (Kg/s)
Nu	Nusselt number
P	Electric power (W)
P	Pressure (Pa)
Pr	Prandtl Number
$\dot{Q}$, $\dot{q}$	Thermal power (W)
Q	Thermal energy (J)
R	Equivalent thermal conductance (W/°K)
Re	Reynolds Number
S	Surface (m^2)
T	Temperature (°C)
t	Time (s)
u	Speed (m/s)

U	Heat transfer coefficient ($W/m^2 \cdot °K$)
v	Wind speed (m/s)
$\dot{w}$	Work (W)
x	Longitudinal displacement (m)
z	height (m)
α	Absorptance of the surface
β	Thermal expansion coefficient ($°K^{-1}$)
χ	Correction coefficient for CPV power evaluation ($°K^{-1}$)
γ	Recirculation factor
δ	Dispatch capability (kWh_{el}/ kWh_{el})
ε	Emissivity
η	Efficiency
μ	Dynamic viscosity (Pa·s)
ν	Kinematic viscosity (m^2/s)
π	Power ratio (kW/kW)
ρ	Volumetric mass density (kg/m^3)
σ	Stefan–Boltzmann constant ($W/(m^2 \cdot °K^4)$
τ	Time duration (h)
ζ	Zenith angle (°)
ι	Radiative heat transfer coefficient ($W/m^2 \cdot °K$)
κ	Thermal conductivity (W/(m·K))
ξ	Azimuth angle (°)
φ	Solar elevation (°)
θ	Incidence angle (°)
ω	Generic coefficient

Subscripts

B	Battery
BC	Battery during charge phase
BD	Battery during discharge phase
c	Cell
C	Capacity
CLN	Cleanliness factor
DEL	Delivered
EL	Electric
END	End loss
EXT	External
IN	Inlet
INT	Internal
L	Losses
MAX	Maximum
MIN	Minimum
Opt	Optical
OUT	Output
Pipe	Piping
R	Roof
RCV	Receiver
REC	Recirculation
REF	Reference
REQ	Requested
SCH	Scheduled
TRACK	Tracking system

w	Wall

Acronyms

AM	Air Mass
CPV	Concentration Photo Voltaic
CSP	Concentrating Solar Power
DNI	Direct Normal Irradiance (W/m2)
ENV	Environment
F-INT	Full Integration Strategy
HCPV	High Concentration Photo Voltaic
HRES	Hybrid Renewable Energy Sources
HTF	Heat Transfer Fluid
IAM	Incidence Angle Modifier
MPPT	Maximum Power Point Tracking
ORC	Organic Rankine Cycle
P-INT	Partial Integration Strategy
PCM	Phase Change Material
PV	Photo Voltaic
RES	Renewable Energy Sources
SF	Solar Field
SOC	State Of Charge
TES	Thermal Energy Storage

Bibliography

[1] WEO. World Energy Outlook. Int Energy Agency 2014:690 pp. doi:10.1787/20725302.

[2] GSE - Gestore dei Servizi Energetici. Energia da fonti rinnovabili in Italia - Dati preliminari 2015. 2016.

[3] Ibrahim H, Ilinca a., Perron J. Energy storage systems-Characteristics and comparisons. Renew Sustain Energy Rev 2008;12:1221–50. doi:10.1016/j.rser.2007.01.023.

[4] Huber M, Dimkova D, Hamacher T. Integration of wind and solar power in Europe: Assessment of flexibility requirements. Energy 2014;69:236–46. doi:10.1016/j.energy.2014.02.109.

[5] Nehrir MH, Wang C, Strunz K, Aki H, Ramakumar R, Bing J, et al. A review of hybrid renewable/alternative energy systems for electric power generation: Configurations, control, and applications. IEEE Trans Sustain Energy 2011;2:392–403. doi:10.1109/TSTE.2011.2157540.

[6] Lopes J a P, Hatziargyriou N, Mutale J, Djapic P, Jenkins N. Integrating distributed generation into electric power systems: A review of drivers, challenges and opportunities. Electr Power Syst Res 2007;77:1189–203. doi:10.1016/j.epsr.2006.08.016.

[7] Pepermans G, Driesen J, Haeseldonckx D, Belmans R, D'haeseleer W. Distributed generation: Definition, benefits and issues. Energy Policy 2005;33:787–98. doi:10.1016/j.enpol.2003.10.004.

[8] Celik a N. Optimisation and techno-economic analysis of autonomous photovoltaic-wind hybrid energy systems in comparison to single photovoltaic and wind systems. Energy Convers Manag 2002;43:2453–68. doi:10.1016/S0196-8904(01)00198-4.

[9] Bajpai P, Dash V. Hybrid renewable energy systems for power generation in stand-alone applications: A review. Renew Sustain Energy Rev 2012;16:2926–39. doi:10.1016/j.rser.2012.02.009.

[10] Diaf and OBFBKMS, Baghdadi F, Mohammedi K, Diaf S, Behar

O. Feasibility study and energy conversion analysis of stand-alone hybrid renewable energy system. Energy Convers Manag 2015;105:471–9. doi:10.1016/j.enconman.2015.07.051.

[11] Sinha S, Chandel SS. Review of recent trends in optimization techniques for solar photovoltaic–wind based hybrid energy systems. Renew Sustain Energy Rev 2015;50:755–69. doi:10.1016/j.rser.2015.05.040.

[12] Mahesh A, Sandhu KS. Hybrid wind/photovoltaic energy system developments: Critical review and findings. Renew Sustain Energy Rev 2015;52:1135–47. doi:10.1016/j.rser.2015.08.008.

[13] Green A, Diep C, Dunn R, Dent J. High Capacity Factor CSP-PV Hybrid Systems. Energy Procedia 2015;69:2049–59. doi:10.1016/j.egypro.2015.03.218.

[14] Slavin A. CSP-PV Hybrid to Deliver 90% of Mine's Energy Needs. Energy and Mines 2014:1–6.

[15] Parrado C, Girard A, Simon F, Fuentealba E. 2050 LCOE (Levelized Cost of Energy) projection for a hybrid PV (photovoltaic)-CSP (concentrated solar power) plant in the Atacama Desert, Chile. Energy 2016;94:422–30. doi:10.1016/j.energy.2015.11.015.

[16] Green MA, Emery K, Hishikawa Y, Warta W, Dunlop ED. Solar cell efficiency tables (Version 45). Prog Photovoltaics Res Appl 2015;20:6–11. doi:10.1002/pip.

[17] Trujillo Serrano PJ, Alamillo Davila C, Martínez Montes M, De La Rubia O, Rubio F, Masa-Bote D, et al. Instituto de Sistemas Fotovoltaicos de Concentraciòn concentration photovoltaics hybrid system first year of operation and improvements. Prog Photovoltaics Res Appl 2013;21:1260–75. doi:10.1002/pip.2366.

[18] M. Vetter, A. Schies, J. Wachtel, B.P. Koirala, I. Heile, A. Gombert FA. the World'S First Cpv Stand-Alone System – Water Supply in Remote Areas of Egypt. 25th Eur Photovolt Sol Energy Conf Exhib / 5th World Conf Photovolt Energy Convers - Val 2010:6–10.

[19] Cabeza LF, Galindo E, Prieto C, Barreneche C, Inés Fernández A. Key performance indicators in thermal energy storage: Survey and assessment. Renew Energy 2015;83:820–7. doi:10.1016/j.renene.2015.05.019.

[20] Plan I, Team S. SET-Plan - SOLAR THERMAL ELECTRICITY

EUROPEAN INDUSTRIAL INITIATIVE (STE-EII) IMPLEMENTATION PLAN 2013-2015 Approved by the SEII Team 2015.

[21] Strategic Energy Technologies Information System (SETIS). Concentrated solar power 2014.

[22] Vasallo MJ, Bravo JM. A MPC approach for optimal generation scheduling in CSP plants 2016;165:357–70. doi:10.1016/j.apenergy.2015.12.092.

[23] Dinter F, Gonzalez DM. Operability, reliability and economic benefits of CSP with thermal energy storage: First year of operation of ANDASOL 3. Energy Procedia 2013;49:2472–81. doi:10.1016/j.egypro.2014.03.262.

[24] Usaola J. Participation of CSP plants in the reserve markets: A new challenge for regulators. Energy Policy 2012;49:562–71. doi:10.1016/j.enpol.2012.06.060.

[25] SolarPACES, Greenpeace, Estela. Solar Thermal Electricity Global Outlook 2016. 2016.

[26] SolarPACES. CSP projects around the world n.d. http://www.solarpaces.org/csp-technology/csp-projects-around-the-world (accessed July 1, 2016).

[27] Rahimi E, Rabiee A, Aghaei J, Muttaqi KM, Esmaeel Nezhad A. On the management of wind power intermittency. Renew Sustain Energy Rev 2013;28:643–53. doi:10.1016/j.rser.2013.08.034.

[28] Law EW, Prasad AA, Kay M, Taylor RA. Direct normal irradiance forecasting and its application to concentrated solar thermal output forecasting – A review. Sol Energy 2014;108:287–307. doi:10.1016/j.solener.2014.07.008.

[29] IEA. Snapshot of Global PV Markets 2014 2015:1–16.

[30] Forrester J. The Value of CSP with Thermal Energy Storage in Providing Grid Stability. Energy Procedia 2014;49:1632–41. doi:10.1016/j.egypro.2014.03.172.

[31] Fernandez-Garcia A, Zarza E, Valenzuela L, Perez M. Parabolic-trough solar collectors and their applications. Renew Sustain Energy Rev 2010;14:1695–721. doi:10.1016/j.rser.2010.03.012.

[32] Mossaz S, Gruss JA, Ferrouillat S, Skrzypski J, Getto D, Poncelet O, et al. Experimental study on the influence of nanoparticle PCM slurry for high temperature on convective heat transfer and

energetic performance in a circular tube under imposed heat flux. Appl Therm Eng 2015;81:388–98. doi:10.1016/j.applthermaleng.2015.01.028.

[33] Zarza E, Valenzuela L, León J, Weyers H-D, Eickhoff M, Eck M, et al. The DISS Project: Direct Steam Generation in Parabolic Trough Systems. Operation and Maintenance Experience and Update on Project Status. J Sol Energy Eng 2002;124:126. doi:10.1115/1.1467645.

[34] AREVA. Asia's largest Concentrated Solar Power (CSP) project : 2 x 125 MW in Rajasthan , India 2013:0–1.

[35] NREL. Concentrating Solar Power Projects with Operational Plants n.d. http://www.nrel.gov/csp/solarpaces/projects_by_status.cfm?status=Operational (accessed October 17, 2016).

[36] Kalaiselvam S, Parameshwaran R. Thermal Energy Storage Technologies for Sustainability. Elsevier; 2014. doi:10.1016/B978-0-12-417291-3.00001-3.

[37] Cabeza LF, de Gracia A. Advances in Thermal Energy Storage Systems. Elsevier; 2015. doi:10.1533/9781782420965.4.549.

[38] Navarro ME, Martínez M, Gil A, Fernández AI, Cabeza LF, Olives R, et al. Selection and characterization of recycled materials for sensible thermal energy storage. Sol Energy Mater Sol Cells 2012;107:131–5.

[39] Lovegrove K, Stein W, (Ed.). Concentrating Solar Power Technology: Principles, Developments and Applications. 2012.

[40] Arena S. Modelling , design and analysis of innovative thermal energy storage systems using PCM for industrial processes , heat and power. University of Cagliari, 2015.

[41] Abedin A, Rosen M. A Critical Review of Thermochemical Energy Storage Systems. Open Renew Energy J 2011;4:42–6. doi:10.2174/1876387101004010042.

[42] Quoilin S, Lemort V. Technological and Economical Survey of Organic Rankine Cycle Systems. 5th Eur Conf Econ Manag Energy Ind 2009;278:12. doi:hdl.handle.net/2268/14609.

[43] ORC world map n.d. http://orc-world-map.org/analysis.html.

[44] Manente G, Rech S, Lazzaretto A. Optimum choice and placement of concentrating solar power technologies in integrated solar

combined cycle systems. Renew Energy 2016;96:172–89. doi:10.1016/j.renene.2016.04.066.

[45] Irena. Renewable Power Generation Costs in 2014 : An Overview 2015:92.

[46] VGB PowerTech Publishing -. Levelised Cost of Electricity 2015 2015.

[47] GSE - Gestore dei Servizi Energetici. Solar thermodynamic Feed-in tariff n.d. http://www.gse.it/en/feedintariff/Thermodynamic solar/Pages/default.aspx (accessed October 21, 2016).

[48] International Energy Agency. Technology Roadmap Solar Thermal Electricity 2014:52. doi:10.1007/SpringerReference_7300.

[49] Lauterbach C. Solar heat for industrial processes – Technology and potential n.d.:1–23.

[50] European Commission. Hydrogen Energy and Fuel Cells. 2003.

[51] Philipps SP, Bett AW, Horowitz K, Kurtz S. Current Status of Concentrator Photovoltaic (CPV) Technology. Natl Renew Energy Lab 2015:1–25. doi:http://www.ise.fraunhofer.de/en/publications/veroeffentlichungen-pdf-dateien-en/studien-und-konzeptpapiere/current-status-of-concentrator-photovoltaic-cpv-technology.pdf.

[52] Archimede Solar Energy - HCEOI12 n.d. http://www.archimedesolarenergy.it/en_hceoi-12-olio.htm (accessed March 23, 2016).

[53] Stuetzle T. Automatic Control of the 30 MWe SEGS IV Parabolic Trough Plant 2002.

[54] Luo N, Yu G, Hou HJ, Yang YP. Dynamic Modeling and Simulation of Parabolic Trough Solar System. Energy Procedia 2015;69:1344–8. doi:10.1016/j.egypro.2015.03.137.

[55] Migliari L, Arena S. Thermal Energy Losses During Night, Warm-up and Full-Operation Periods of a CSP Solar Field Using Thermal Oil. Energy Procedia 2015;82:1002–8. doi:10.1016/j.egypro.2015.11.858.

[56] Cau G, Cocco D. Comparison of medium-size concentrating solar power plants based on parabolic trough and linear Fresnel collectors. Energy Procedia 2014;45:101–10. doi:10.1016/j.egypro.2014.01.012.

[57] Cocco D, Serra F. Performance comparison of two-tank direct and thermocline thermal energy storage systems for 1MWe class concentrating solar power plants. Energy 2015;81:526–36. doi:10.1016/j.energy.2014.12.067.

[58] Giostri A, Binotti M, Silva P, Macchi E, Manzolini G. Comparison of two linear collectors in solar thermal plants: Parabolic trough vs Fresnel 2011:10. doi:10.1115/ES2011-54312.

[59] Migliari L, Arena S, Puddu P, Cocco D. Thermo-fluid dynamic analysis of a CSP solar field line during transient operation. Energy Procedia 2016;101:1167–74. doi: 10.1016/j.egypro.2016.11.158

[60] Comsol. The Heat Transfer Module User's Guide. n.d.

[61] Rolander N, Rambo J, Joshi Y, Allen JK, Mistree F. An Approach to Robust Design of Turbulent Convective Systems. J Mech Des 2006;128:844–55.

[62] Sa M, Zaversky F, Garcı J, García-Barberena J, Sánchez M, Astrain D. Transient molten salt two-tank thermal storage modeling for CSP performance simulations. Sol Energy 2013;93:294–311. doi:10.1016/j.solener.2013.02.034.

[63] Duffie JA, Beckman WA. Solar Engineering of Thermal Processes: Fourth Edition. John Wiley and Sons; 2013.

[64] Rodrigo P, Fernández EF, Almonacid F, Pérez-Higueras PJ. Models for the electrical characterization of high concentration photovoltaic cells and modules: A review. Renew Sustain Energy Rev 2013;26:752–60. doi:10.1016/j.rser.2013.06.019.

[65] Helmers H, Schachtner M, Bett AW. Influence of temperature and irradiance on triple-junction solar subcells. Sol Energy Mater Sol Cells 2013;116:144–52. doi:10.1016/j.solmat.2013.03.039.

[66] Fernández EF, Almonacid F, Rodrigo P, Pérez-Higueras P. Model for the prediction of the maximum power of a high concentrator photovoltaic module. Sol Energy 2013;97:12–8. doi:10.1016/j.solener.2013.07.034.

[67] Cocco D, Puddu P, Palomba C. Tecnologie delle energie rinnovabili. 2010.

[68] Soitec Solar GmbH. Technical Data Sheet - Soitec CX-S530-II CPV System 2014. http://soitec.com/pdf/CX-S530-II_30.6kWp_Technical_Data_Sheet_v12_EN_2014-07-15.pdf.

[69] Renzi M, Egidi L, Comodi G. Performance analysis of two 3.5kWp CPV systems under real operating conditions. Appl Energy 2015;160:687–96. doi:10.1016/j.apenergy.2015.08.096.

[70] Vivar M, Herrero R, Anton I, Martinez-Moreno F, Moreton R, Sala G, et al. Effect of soiling in CPV systems. Sol Energy 2010;84:1327–35. doi:10.1016/j.solener.2010.03.031.

[71] Cocco D, Migliari L, Petrollese M. A hybrid CSP–CPV system for improving the dispatchability of solar power plants. Energy Convers Manag 2016;114:312–23. doi:10.1016/j.enconman.2016.02.015.

[72] Cocco D, Migliari L, Serra F. Influence of thermal energy losses on the yearly performance of medium size CSP plants. Proc. ECOS 2015 - 28TH Int. Conf. Effic. COST, Optim. Simul. Environ. IMPACT ENERGY Syst., PAU, FRANCE: 2015.

[73] Migliari L, Cocco D, Petrollese M, Cau G. Capability of a small size CSP plant to provide dispatch power. Proc. ECOS 2016 - 29TH Int. Conf. Effic. COST, Optim. Simul. Environ. IMPACT ENERGY Syst., 2016.